

博士論文

Development of X-ray imaging system using silicon strip detector

(シリコンストリップ検出器を用いたX線撮像システムの開発)

巖小松 (Yan Xiaosong)

Doctor of Philosophy

in

Department of Nuclear Engineering and Management

Graduate School of Engineering

The University of Tokyo

Advisor:

Prof. Hiroyuki Takahashi

2015

Abstract

We are developing a photon-counting X-ray imaging system consisting of stacked edge-on silicon strip detectors for nondestructive testing of steel components in nuclear facilities and concrete infrastructures.

Strip detectors with 50 channels and 1 mm pitch were fabricated with the a-Si/c-Si heterojunction technique. The leakage current density of the detector was measured to be 0.06 nA/mm² at 120 V bias. The fabricated detector had energy resolutions of 2.8 keV FWHM at 59.5 keV and 2.9 keV FWHM at 122 keV. The spatial resolution of the 1-mm-pitch strip detector was measured to be lower than 2 mm (FWHM).

We coupled the strip detectors with ASICs based on Time-over-Threshold (ToT) method, and we build an X-ray imaging module consisting of 6 stacked silicon strip detectors. The module was evaluated with a ¹³⁷Cs gamma-ray source. It had efficiency of about 20% for the 662 keV photons and the spatial resolution of the module was measured to be about 1 mm (rms). One-scan and six-scan images of a 2-cm-thick tungsten sample and an 1-cm-thick iron sample were obtained. The module was also evaluated with the 0.95 MeV LINAC X-ray source. Spatial resolution of the module was measured to be about 1 mm (rms). Six-scan images of the same tungsten sample and the iron sample were obtained. Each scan lasted for 180 s for accumulating sufficient statistics. The images measured with the LINAC X-ray source reproduced the samples without distortion and amplification. The six-layer module was also used to image a 20-cm-thick concrete with the 0.95 MeV LINAC X-ray source. Reinforcing bars inside the concrete were observed.

We are planning to construct 4 (2×2) modules which will have a field of view as large as 10 cm×10 cm. In addition, tungsten collimator module will be applied to suppress scattering and on-site NDT experiments will be proceeded.

Keywords: *silicon strip detector, X-ray imaging, ToT ASIC, nondestructive testing, a-Si/c-Si heterojunction detector, photon-counting*

Acknowledgements

This research can never be proceeded without the support and contribution of many people and organizations. I would like to express my deepest appreciation to all the people who have helped me and organizations that have supported me.

First of all, I owe my deepest gratitude to my advisor, Professor Hiroyuki Takahashi for his continuous guidance and support in the past three years. He was always eager for sharing his knowledge and experience and also giving precious advices. Particularly I was always greatly affected and touched by his intense enthusiasm for scientific research. He has always been working up to deep night and sometimes he replied to my email in the early morning. He has the best insight into a research problem, the current status of research and the hotspots and new trend of the whole research field. Above all, he has always taught me that a novel, original and creative idea is beyond restrictions owing to the current conditions and a modern researcher should always persist in overcoming difficulties until the final success.

I would like to express my gratitude to Doctor Yang Tian, as a senior and good friend, who was always willing to help me and give me his best suggestions. He helped me a lot when I was studying fundamentals, proceeding numerical simulations and performing experiments. My research progress would have been greatly postponed without his help. He also showed me how a young researcher with great potential improves himself during doing research.

I express sincere appreciation to Doctor Kenji Shimazoe and Doctor Takeshi Fujiwara for their great support in doing experiments, constructing the imaging system and also communicating with other Japanese engineers.

I would like to thank Doctor Masashi Ohno and Doctor Yoneichi Hosono for their support during experiments and lab meetings.

I would like to thank all the other members of Takahashi Laboratory, who make me feel like home in Japan. The past three years when we studied in the same room will always be happy and precious memory for me.

I am grateful to Ms. Ayako Watanabe in Takahashi Laboratory, Ms. Mari Morishita, Ms. Nabeshima and all other administrative staffs in the department of Nuclear Engineering and Management for their help even before my enrollment. They helped me have an easier life in Japan.

I also acknowledge the financial support from Ministry of Education, Culture, Sports, Science and Technology, Government of Japan.

It was my great honor to have the chance to study in the University of Tokyo, one of the best universities all over the world. My research and life during the last three years in Japan will be forever remembered.

Finally, I would like to thank my parents. They were always supporting me with their best wishes. I would like to thank my wife. She was always there cheering me up when I achieved progress and comforting and encouraging me when I met with problems. Whenever and wherever, I can feel their deepest love and strongest support.

Contents

Abstract	i
Acknowledgements	i
Contents	ii
List of Figures	vii
List of Tables	xi
Abbreviations	xiii
1 Introduction	1
1.1 Importance and demand for nondestructive testing	1
1.2 NDT techniques	2
1.2.1 Sonic/ultrasonic methods	2
1.2.2 Electromagnetic methods	2
1.2.3 Electrical methods	3
1.2.4 Infrared thermography	3
1.2.5 Radiography	3
1.3 X-ray imaging system	5
1.3.1 X-ray generator	6
1.3.2 Radiography detectors	8
1.3.2.1 Scintillators	9
1.3.2.2 Semiconductor detectors	10
1.3.2.3 Detection efficiency of traditional imaging detectors . . .	12
1.4 Energy-integrating and photon-counting techniques	12
1.4.1 Energy-integrating technique	12
1.4.2 Photon-counting technique	13
1.5 Objectives	15
1.6 X-ray imaging system design	15
1.6.1 Detector module	16
1.6.2 Collimator module	16

2	System design based on Monte Carlo simulation	19
2.1	Widely used Monte Carlo codes	19
2.1.1	MCNP	20
2.1.2	EGS	20
2.1.3	FLUKA	21
2.1.4	GEANT4	21
2.1.5	Other codes	21
2.2	Energy spectrum of the X-ray source	22
2.3	X-ray attenuation and scattering in concrete	24
2.4	Scattering decrease with object-to-detector distance	27
2.5	Detector module response	31
2.6	Evaluation of PCB, tungsten shielding and tungsten collimator	34
2.6.1	Influence of PCBs	35
2.6.2	Tungsten shielding inside the detector stack	35
2.6.3	Tungsten collimator in front of the detector stack	38
2.7	Summary	43
3	a-Si/c-Si heterojunction strip detector	45
3.1	Interaction of photons	45
3.1.1	Photoelectric effect	45
3.1.2	Compton scattering	46
3.1.3	Pair production	47
3.2	Detector basics	48
3.2.1	Intrinsic properties of silicon	48
3.2.2	Extrinsic properties of silicon	50
3.2.3	p-n junction	52
3.3	Fabrication processes of silicon strip detector	54
3.3.1	General process steps in passivated planar technology	54
3.3.2	a-si/c-si heterojunction process	55
3.4	Operational characteristics	57
3.4.1	Leakage current characteristics	57
3.4.2	Capacitance characteristics	59
3.5	Energy spectrum measurement	59
3.5.1	^{241}Am spectrum and ^{57}Co spectrum	60
3.5.2	^{133}Ba spectrum and ^{137}Cs spectrum	60
3.6	Position sensitivity evaluation	60
3.7	Conclusion	62
4	Time-over-Threshold (ToT) based front-end electronics	65
4.1	Integrated circuit technology	66
4.1.1	A brief history of integrated circuit	66
4.1.2	CMOS technology	67
4.1.3	ASIC	68
4.2	Principle of ToT method	69
4.3	ToT ASIC	70
4.3.1	Charge-sensitive preamplifier	70
4.3.2	Shaping amplifier	72

4.3.3	Comparator	73
4.3.4	DAC	73
4.3.5	Response of ToT to input charge	75
4.4	Evaluation of the ToT ASIC	76
4.4.1	Baseline and noise characteristics	76
4.4.2	ToT spectrum	77
4.5	Dynamic ToT	77
4.5.1	Principle of dynamic ToT	77
4.5.2	Dynamic ToT ASIC	79
5	Development of imaging system	81
5.1	Continuous-mode system	81
5.1.1	One-layer module	83
5.1.1.1	Edge-on efficiency	83
5.1.1.2	Edge-on spatial resolution	84
5.1.1.3	Scan imaging of samples	84
5.1.2	Scan imaging with two-layer module	86
5.2	Pulse-mode system	89
5.2.1	Gamma-ray imaging with the ^{137}Cs source	89
5.2.1.1	Edge-on efficiency	89
5.2.1.2	Edge-on spatial resolution	91
5.2.1.3	Scan imaging of samples	93
5.2.2	X-ray imaging the 0.95 MeV LINAC X-ray generator	94
5.2.2.1	Edge-on spatial resolution	94
5.2.2.2	Scan imaging of samples	95
5.2.2.3	Scan imaging of reinforcing bars inside concrete	95
6	Conlusion and discussion	99
6.1	Conclusion	99
6.2	Discussion	100
6.3	Future works	101
	Bibliography	103

List of Figures

1.1	A gamma-ray radiography system.	4
1.2	Principle of laser-Compton X-ray source.	6
1.3	Comparison of the laser-Compton X-ray spectrum and bremsstrahlung X-ray spectrum	7
1.4	X-band LINAC. (a) 950 keV LINAC. (b) 3.95 MeV LINAC.	8
1.5	Schematic of a flat-panel detector.	10
1.6	Schematic of a flat-panel detector.	10
1.7	Dynamic ranges of scintillator screen and multi-CdTe detector	11
1.8	Detection efficiency of typical detectors for photons	12
1.9	A schematic diagram of the energy-integrating circuit.	13
1.10	Signals of the energy integrating circuit.(a) Current signal. (b) Voltage signal.	13
1.11	A schematic diagram of the photon-counting circuit.	14
1.12	Analog and digital signals. (a) Voltage and threshold signals.(b) Counts of signals higher than threshold.	14
1.13	One detector module that consists of stacked silicon strip detectors and tungsten sheets.	16
1.14	Assembly of detector module and collimator module.	17
2.1	Geometry of the X-ray target	23
2.2	Energy spectrum of the 3.95 MeV X-ray source	23
2.3	Geometry of the X-ray attenuation simulation	24
2.4	Spectrum at 10 cm behind 20-cm-thick concrete	25
2.5	Spectrum at 10 cm behind 40-cm-thick concrete	25
2.6	Spectrum at 10 cm behind 60-cm-thick concrete	26
2.7	Spectrum at 10 cm behind 80-cm-thick concrete	26
2.8	Spectrum at 10 cm behind 100-cm-thick concrete	27
2.9	Spectrum at 10 cm behind 40-cm-thick concrete	28
2.10	Spectrum at 20 cm behind 40-cm-thick concrete	29
2.11	Spectrum at 30 cm behind 40-cm-thick concrete	29
2.12	Spectrum at 40 cm behind 40-cm-thick concrete	30
2.13	Spectrum at 50 cm behind 40 cm concrete	30
2.14	Geometry of concrete and detector module. The detector module is com- posed of 20 stacked 50-channel silicon strip detectors.	31
2.15	Cross section of the detector stack. Each silicon strip detector is divided into 50 individual channels.	32
2.16	Photons incident on a plane in front of the detector module. Primary photons and scattered photons are recorded separately.	32

2.17	Photons incident on the 1000 silicon channels. Primary photons and scattered photons are recorded separately.	33
2.18	Spectrum of deposited energy on 1000 channels.	33
2.19	Event number when one photon is detected.	34
2.20	Concrete and the interior iron bars and the projected view of iron bars on the detector stack	35
2.21	Spectra of photons incident on the 1000 silicon channels. PCBs are placed below each detector.	36
2.22	Spectrum of deposited energy on 1000 channels. PCBs are placed below each detector.	36
2.23	Image of the phantom concrete. PCBs are placed below each detector. . .	37
2.24	Horizontal profiles of the red rectangular area without/with threshold. PCBs are placed below each detector.	37
2.25	Spectra of photons incident on the 1000 silicon channels. Tungsten sheets are placed inside the detector stack.	38
2.26	Spectrum of deposited energy on 1000 channels. Tungsten sheets are placed inside the detector stack.	39
2.27	Image of the phantom concrete. Tungsten sheets are placed inside the detector stack.	39
2.28	Horizontal profiles of the red rectangular area without/with threshold. Tungsten sheets are placed inside the detector stack.	40
2.29	Geometry of concrete, tungsten collimator and the detector stack. . . .	40
2.30	Spectra of photons incident on the 1000 silicon channels. Tungsten collimator is placed in front of the detector stack.	41
2.31	Spectrum of deposited energy on 1000 channels. Tungsten collimator is placed in front of the detector stack.	42
2.32	Image of the phantom concrete. Tungsten collimator is placed in front of the detector stack.	42
2.33	Horizontal profiles of the red rectangular area without/with threshold. Tungsten collimator is placed in front of the detector stack.	43
3.1	Demonstration of the photoelectric effect.	46
3.2	Demonstration of the Compton scattering.	47
3.3	Demonstration of the pair production.	47
3.4	The relative importance of the three major interactions.	48
3.5	Diamond-lattice type structure of silicon.	48
3.6	n-type doping.(a) The crystal lattice of Si doped with As. (b) Band structure of n-type material.	51
3.7	p-type doping.(a) The crystal lattice of Si doped with B. (b) Band structure of p-type material.	52
3.8	A p-n junction in thermal equilibrium (a) with two parts separated (b) with two parts brought together.	53
3.9	Steps of the passivated planar process.	55
3.10	Steps of fabricating a-Si/c-Si heterojunction strip detector.	56
3.11	A fabricated a-Si/c-Si heterojunction strip detector.	57
3.12	Configuration of the leakage current measurement. 3 channels are biased at the same high voltage simultaneously.	58
3.13	Leakage currents of 3 adjacent channels in one measurement.	58

3.14	(a) Bias dependence of the leakage currents of 5 channels (b) Leakage currents of all 50 channels.	59
3.15	(a) Junction capacitances of 5 channels. (b) Depletion depth of 5 channels.	59
3.16	^{241}Am spectrum measured by channel 2. The FWHM of the 59.5 keV photopeak is 2.8 keV.	60
3.17	^{57}Co spectrum measured by channel 2. The FWHM of the 122 keV photopeak is 2.9 keV.	61
3.18	(a) The measured ^{133}Ba spectrum. (b) The measured ^{137}Cs spectrum.	61
3.19	Setup of the position-sensitivity evaluation.	62
3.20	Count distributions of 5 measurements with a collimated ^{90}Sr β source	62
4.1	Dependence of drain current on drain to source voltage.	67
4.2	CMOS technology: n- and p-channel enhancement transistors.	68
4.3	Block diagram and signal flow of ToT method.	70
4.4	Board and die of the 48-channel ToT ASIC.	71
4.5	Simplified diagram of a charge-sensitive preamplifier.	71
4.6	Schematic of the preamplifier implemented in the ASIC.	72
4.7	Schematic of CR-RC pulse shaping.	73
4.8	Schematic of the shaper with PZC circuit.	74
4.9	Schematic of implemented comparator.	74
4.10	Pin configuration of the DAC128S085 12-bit DAC.	75
4.11	ToT responses to the input charge at different threshold levels.	75
4.12	Demonstration of the baseline and noise of the signal output to the comparator in the ASIC.	76
4.13	A scanned baseline and noiserange of one ASIC chip.	76
4.14	The measured ToT spectrum of ^{137}Cs source.	77
4.15	Schematic of the dynamic ToT circuit.	78
4.16	Waveforms of CR-RC signal, dynamic threshold signal and ToT signal of the dynamic ToT circuit.	78
4.17	Schematic of one channel of the 64-channel dynamic ToT ASIC.	79
4.18	Layout of the 64-channel dynamic ToT ASIC.	80
5.1	The continuous-mode system.	82
5.2	Wired-OR multiplex readout.	82
5.3	ToT spectra of 144 channels with irradiation from a ^{137}Cs γ -ray source. Some channels are masked intentionally in the DAQ software.	83
5.4	Count distributions with irradiation from a ^{137}Cs γ source.	84
5.5	Setup of the edge-on spatial resolution evaluation.	85
5.6	Normalized and fitted count distributions of four measurements using flood-field data.	85
5.7	Setup of the scan imaging of an iron object.	86
5.8	Scan image of the iron object.	86
5.9	Scans of an iron object filled with soil. (a) The iron object filled with soil. (b) The scan image of the object.	87
5.10	Setup for the scans of the tungsten object.	87
5.11	Nine-step scan images of the tungsten object using two detectors.	88
5.12	Splice of two scanned images.	88
5.13	The pulse-mode system.	89

5.14	The constructed pulse-mode module with 6 stacked layers.	90
5.15	Flood-field counts with irradiation from a ^{137}Cs γ source.	90
5.16	Setup for the edge-on spatial resolution evaluation of the 6-layer module with the 1 MBq ^{137}Cs source.	91
5.17	Normalized count distributions of 3 measurements.	91
5.18	Normalized and fitted count distributions of 3 measurements of 6 detectors.	92
5.19	One-scan and six-scan images of the tungsten sample.	93
5.20	One-scan and six-scan images of the iron sample filled with soil.	94
5.21	Count distributions when the a part of the detector module was shielded with a 2 mm thick lead. (a) Distributions of six layers (b) Fitting of six distributions.	95
5.22	Six-scan images of the tungsten object and the iron object.(a) Image of the tungsten object.(b) Image of the iron object.	96
5.23	Scan imaging of a 20 cm thick concrete. The darker parts represent the iron reinforcing bars.	96
5.24	Six-scan images of the tungsten object and the iron object.(a) Image of the tungsten object.(b) Image of the iron object.	97
6.1	Imaging system composed of (2×2) modules.	102
6.2	Tungsten collimator modules.	102

List of Tables

1.1	Common isotopes and the corresponding half value layer thickness of materials.	4
1.2	Parameters of 950 keV and 3.95 MeV LINAC.	8
1.3	Scintillators for imaging.	9
2.1	X-ray attenuation and scattering after penetrating concrete of different thicknesses	24
2.2	Scatter-to-primary ratios at different object-to-detector distances	28
3.1	Intrinsic properties of commonly used semiconductors.	49

Abbreviations

NDT	N on- D estructive T esting
EC	E ddy C urrent
GPR	G round P enetrating R adar
MRI	M agnetic R esonance I maging
LINAC	L INear A Ccelerator
CT	C omputed T tomography
PHERMEX	P ulsed H high- E nergy R adiographic M achine E mitting X -rays
LCS	L aser C ompton S cattering
CCD	C harge C oupled D evice
APD	A valanche P hoto D iode
PMT	P hoto M ultiplier T ube
SiPM	S ilicon P hoto M ultiplier
SIT	S ilicon I ntensified T arget
DAC	D igital-to- A nalog C onverter
SNR	S ignal-to- N oise R atio
PCB	P rint C ircuit B oard
ASIC	A pplication S pecific I ntegrated C ircuit
PET	P ositron E mission T omography
SPECT	S ingle P hoton E mission C omputer T omography
DAQ	D ata A c Q uisition
SSD	S ilicon S trip D etector
FWHM	F ull W idth at H alf M aximum
CVD	C hemical V apor D eposition
PECVD	P lasma E nhanced C hemical V apor D eposition
ECR-CVD	E lectron C yclotron R esonance C hemical V apor D eposition

CMS	C ompact M uon S olendoid
ToT	T ime-over- T hreshold
IC	I ntegrated C ircuit
ADC	A nalog-to- D igital C onverter
SSI	S mall S cale I ntegration
MSI	M edium S cale I ntegration
LSI	L arge S cale I ntegration
VLSI	V ery L arge S cale I ntegration
ULSI	U ltra L arge S cale I ntegration
WSI	W afer S cale I ntegration
SoC	S ystem-on-a- C hip
MOS	M etal O xide S emiconductor
FET	F ield E ffect T ransistor
CMOS	C omplementary M etal O xide S emiconductor
NMOS	n-channel M etal O xide S emiconductor
PMOS	p-channel M etal O xide S emiconductor
TTL	T ransistor T ransistor L ogic
CAD	C omputer A ided D esign
VDEC	VLSI D esign and E ducation C enter
TSMC	T aiwan S emiconductor M anufacturing C ompany
PZC	P ole- Z ero C ancellation
FPGA	F ield P rogrammable G ate A rray
CPLD	C omplex P rogrammable L ogic D evice

Chapter 1

Introduction

1.1 Importance and demand for nondestructive testing

More than 50 main reactors have been constructed in Japan and they provided about 30% of the country's electricity. However, these reactors were stopped after the great nuclear accident on 11 March, 2011. Due to an increase of fossil fuel imports, Japan faces further dependency on the Middle-East, a rise in electricity prices, a rapid increase of greenhouse gas emissions, and an outflow of national wealth. Based on the serious energy situation, Japanese government issued the fourth "Strategic Energy Plan" [1] in April, 2014. It mentioned that Nuclear power is an important base-load power source, contributing to stability of energy supply-demand structure, on the major premise of ensuring its safety. Currently 24 of 43 operable reactors are in the process of restart approvals [2]. Special care has to be taken with steel structures in these reactors, such as reactor vessel, pipes, turbine, et al. to satisfy the major premise of ensuring its safety.

Concrete is the most commonly used construction material on earth, from infrastructures such as highways, bridges, tunnels, et al. to nuclear facilities like containments, cooling towers, reactor vessels and other reactor buildings, from industrial factories to agricultural waste containments. A large number of concrete based solids were built in the past 50 years with little consideration of the long term safety aspects. They play a crucial role in economics and public safety, and the public expects reliable and safe concrete structures, especially at locations that suffered from earthquake, tsunami, landslide and other serious accidents. It is impossible and unnecessary to repair or replace all public works, but it is important to reliably assess the health of aging concrete structures and to appropriately allocate resources based on the assessment where they are most needed. Besides, it is often necessary to test new concrete structures to determine whether they satisfy all design criteria after they have been hardened.

Testing of aging structures is usually related to an assessment of structural integrity or adequacy, while the principal concerns about newly constructed structures are quality control and the resolution of doubts about the quality of materials and construction. In either case, if destructive testing alone is used, the cost of testing and the damage to the structures may only permit a relatively small amount of tests to be proceeded which may be misleading. So testing of both the aging and new concrete structures in most cases is required to be processed without damage to the concrete, leading to the development of nondestructive testing (NDT) techniques.

1.2 NDT techniques

There are a lot of NDT techniques, each based on different theoretical principles and produce different sets of information regarding different physical properties of the concrete structures [3, 4].

1.2.1 Sonic/ultrasonic methods

Nondestructive sonic and ultrasonic testing methods are based on the transmission and reflection of mechanical stress waves through a medium at sonic and ultrasonic frequencies. They can be used for detection of fatigue cracks in welds and assessment of stay cable anchorages to locate possible wire breaks. There are several most used methods: Sonic transmission method, sonic/seismic tomography, sonic/seismic reflection method, ultrasonic reflection method and sonic resonance method. Ultrasonic inspection can be performed in cases where the structure is relatively thin. However, it is difficult to obtain unambiguous information due to the grain structure of thick concrete components.

1.2.2 Electromagnetic methods

Electromagnetic testing is the process of inducing electric currents or magnetic fields inside a test object and observing the electromagnetic response. They are used to detect or measure flaws, bond or weld integrity, thickness, electrical conductivity and detect the presence of reinforcing bar or metals. Eddy current (EC), ground penetrating radar (GPR) and magnetic resonance imaging (MRI) are the most widely used electromagnetic nondestructive testing methods.

1.2.3 Electrical methods

There are mainly two measurements for the electrical methods: resistivity measurements and half-cell potential measurements. The electrical resistivity method can be used to assess the likelihood of significant corrosion within a reinforced concrete structure, and the half-cell potential system where the potential of the embedded steel reinforcement rod is measured relative to a reference half-cell placed on the concrete surface can be used for assessing corrosion of the reinforcing rods.

1.2.4 Infrared thermography

Infrared thermography is a process in which heat is converted into a thermal image using specialized scanning cameras. This technique is the most effective for rapid evaluation of large buildings and can be used for delamination in bare and asphalt-covered concrete and characterization of the paving process.

1.2.5 Radiography

Radiography is one of the earliest NDT techniques used to obtain a shadow image of a solid. Gamma rays, X rays, neutrons and cosmic muons are partially absorbed when they are penetrating through components. The amount of absorption is dependent on the thickness, density and material of the component which the radiation passes through, and also the characteristics (e.g. beam type, energy spectrum, incidence geometry) of the radiation. The radiation which passes through the material can be detected and recorded on imaging devices, such as photographic film, flat panel detector, scintillator array coupled with photo sensors, semiconductor detector array, et al. A projection or a series of projections will be formed and image of the test component can be obtained. Radiography is capable of detecting any feature in a component provided that there are sufficient differences in thickness or density within the test sample. Large differences are more readily detected than small differences. Brief introductions about the radiography technologies are below.

A. Gamma-ray radiography

Figure 1.1 shows a gamma-ray radiography system. A gamma-ray radiography system is generally composed of a gamma-ray source and an imager. Gamma-ray photons are generated by disintegration of a radioactive isotope and used for nondestructive testing. Common isotopes used in radiography are ^{60}Co , ^{137}Cs and ^{192}Ir , and their characteristics are shown in Table 1.1[5].

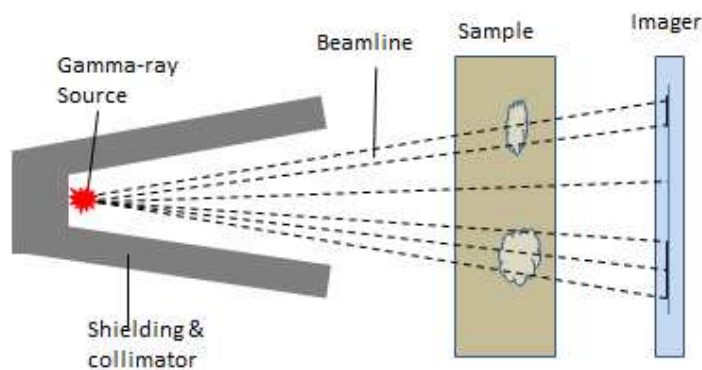


FIGURE 1.1: A gamma-ray radiography system.

TABLE 1.1: Common isotopes and the corresponding half value layer thickness of materials.

Source	Half-life	Energy	Lead	Iron	Concrete
^{60}Co	5.3 years	1.33 MeV, 1.17 MeV	12.5mm	22.1mm	68.6mm
^{137}Cs	30.3 years	0.662 MeV	6.4mm	17.3mm	55.3mm
^{192}Ir	74 days	0.317MeV, 0.468MeV	4.8mm	15.49mm	48.3mm

Isotope gamma sources generate monochromatic radiation, and they are relatively cheap and dimensionally small. The main disadvantage is that isotopes have a limited life and they are generally suitable for testing thin sample objects suffered from low intensity and limited energy. In addition, additional radiation shielding problems are resulted even when not in use because they cannot be turned off.

B. X-ray radiography

There are various types of X-ray generators based on different principles, e.g. laser plasma, synchrotron radiation, electron linear accelerator (LINAC), X-ray tube. A LINAC X-ray source is generally employed to generate X-rays in nondestructive testing of concrete. Compared with gamma-ray radiography, the main advantage of X-ray sources is that they can produce a regulated beam of much higher energy and greater intensity. They can also be switched off if something goes wrong, which represent a significant safety margin. The disadvantages are that they produce polychromatic photons of which most are low-energy photons, and they are expensive and cumbersome to be moved around. If high-intensity X-ray/gamma-ray nondestructive situ testing is to be proceeded, human and cattle have to be cleared in advance.

C. Neutron radiography

Neutron radiography has been used in industrial applications for more than 50 years. Compared with photons, neutrons are more sensitive to the light elements (hydrogen, water, carbon, etc.) in concrete. Chemical containment agents transported by water through cracks can reach and cause damage to steel reinforcing in concrete structures, so it is important to investigate cracks within the concrete and the transport of water through concrete. Neutron radiography has been used to study internal cracking patterns in concrete and quantify of water penetration into concrete through cracks. Neutron radiography has been applied in laboratory testing but cannot be easily used on large scale structures such as bridges.

D. Computed tomography

Computed tomography (CT) is a type of radiography, by turning the object and taking radiographies successively information about the three dimensional inner structure can be obtained. X-ray CT is the most widely used radiography method, and it is capable of producing accurate 2D and 3D cross-sectional images of an object with millimeter or sub-millimeter resolution. Characteristics of an object such as dimensions, shape, internal defects, and density are available from CT images.

E. Muon radiography

Muons have the same electric charge as electrons, but are much more massive ($m_\mu \approx 207m_e$) and have a much higher momentum, conferring them with high penetrating ability. The mean muon energy is 3-4 GeV, which is sufficient to allow them to penetrate several meters of rock before being stopped [6]. Benefitting from their high penetrating capability, muons have been used to image the interiors of structure since 1970 [7]. Mainly based on the Multiple Coulomb Scattering of cosmic ray muons, muon radiography has been proposed as a tool to perform nondestructive testing of very large objects. They are more strongly scattered by high-Z materials, so they are more suitable for probing nuclear materials, such as uranium and plutonium, and shielding materials, such as lead and tungsten. However, natural muons only have a rate of about $10,000 \text{ m}^{-2} \text{ min}^{-1}$ on earth [8], as a result, the process time of muon radiography is much longer than photon radiography techniques.

1.3 X-ray imaging system

An X-ray imaging system for nondestructive testing of concrete mainly consists of 2 components: a LINAC X-ray source for generating X-ray photons and the detector system for recording photons which penetrate concrete components. Systems like CT include a scanner which rotates the sample for a series of projections with X-ray.

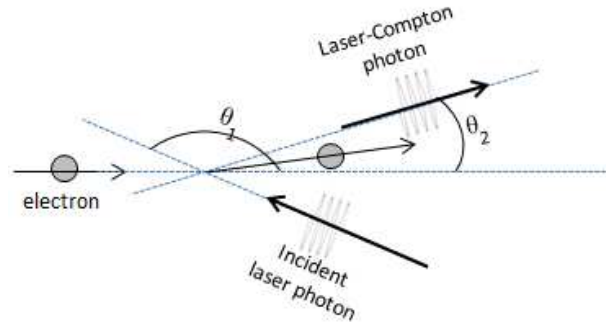


FIGURE 1.2: Principle of laser-Compton X-ray source.

1.3.1 X-ray generator

X-ray generators can be greatly different for laboratory-based nondestructive testing and for on-site nondestructive testing.

A. Electron LINAC X-ray source

Electron LINAC produces high-energy bremsstrahlung X-rays and is the most widely used X-ray source for high-energy imaging. The benchmark for large radiography accelerators is pulsed high-energy radiographic machine emitting X-rays (PHERMEX) [9], and there have been significant advances in electron LINAC designed specifically for radiography over the past dozen years. The accelerator must be capable of producing radiation at a high dose rate, in order to produce sufficient dose for a high-quality image within the short pulse width. For example, an X-ray source has been designed for X-ray radiography based on an S-band 5MeV electron LINAC at Department of Physics, University of Messina [10, 11]. An 1-mm-thick tungsten has been chosen as the electron-gamma converter, coupled with a 9-mm-thick copper layer for filtering the produced X-ray beam both from primary electrons and low energy X-rays. It has been then coupled to a collimation system, providing an X-ray spot of about 16 cm diameters at the sample position, and a beam aperture of about 3.8° .

B. Laser-Compton X-ray source

X-ray sources with a small energy spread are very useful for measuring density profiles because there is almost no cupping artifact on CT images measured with monochromatic X-ray beams [12]. Laser-Compton scattering (LCS) [13] is a technique to generate quasi-monochromatic X rays using laser-electron interaction, and the LCS X-ray source is one of the best choices for nondestructive testing. The kinematics of the LCS X-ray source is shown in Figure 1.2 and the energy of the Compton-scattered photon, E_γ , can be calculated as Formula 1.1:

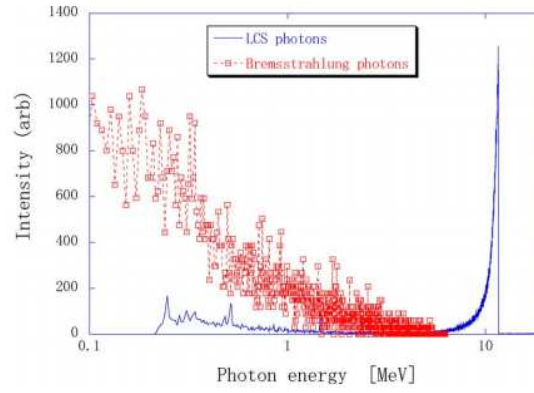


FIGURE 1.3: Comparison of the laser-Compton X-ray spectrum and bremsstrahlung X-ray spectrum

$$E_{\gamma} = \frac{E_L(1 - \beta \cos \theta_1)}{1 - \beta \cos \theta_2 + \frac{E_L(1 - \beta \cos(\theta_2 - \theta_1))}{E_e}}, \text{ where } \beta = \sqrt{1 - \gamma^2}, \gamma = \frac{E_e}{0.511} \quad (1.1)$$

where θ_1 and θ_2 are the angles of the laser photon before and after the Compton scattering with respect to the incident electron.

Figure 1.3 shows the measured Energy spectrum of the LCS X rays, the bremsstrahlung photons produced by 10 MeV electrons bombarding a Cu target is also shown for comparison. The energy spread of the LCS X-rays is 3%, while a continuum is formed in the spectrum of the bremsstrahlung X rays. The laser-Compton X-ray source is a good candidate for laboratory-based test but is not suitable for on-site applications suffered from the huge electron storage ring.

C. Portable X-band LINAC X-ray generator

However, the primary difficulty with use of these devices in on-site nondestructive testing is the weight and size of the X-ray head. For example, nondestructive testing of substructures in a nuclear plant requires the X-ray generator to be moved by hand and can be fitted into very limited space, though a larger space is possible for nondestructive testing of bridges, highways, etc. the LINAC X-ray generator has to be transported by common cargos and it is required to be reasonably small and light. This leads to the development of X-band (8-12 GHz) portable LINAC X-ray generators since late 60s in USA and Russia.

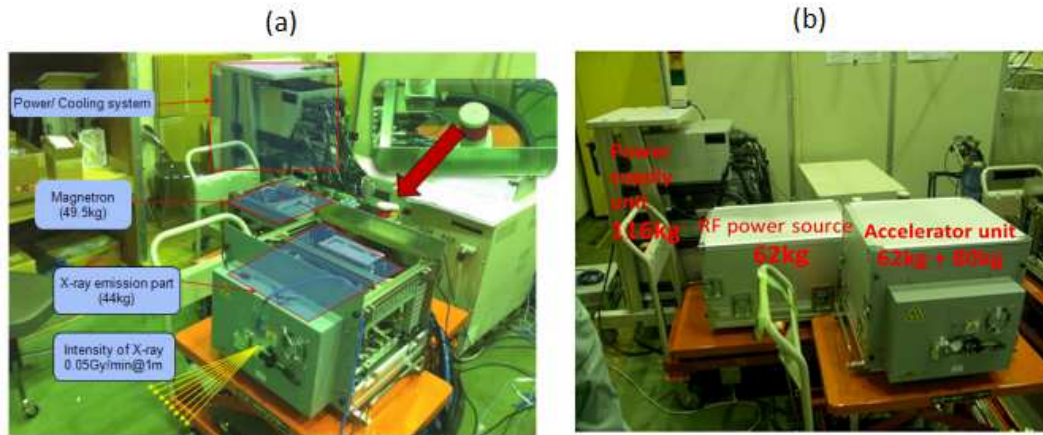


FIGURE 1.4: X-band LINAC. (a) 950 keV LINAC. (b) 3.95 MeV LINAC.

TABLE 1.2: Parameters of 950 keV and 3.95 MeV LINAC.

	950 keV	3.95 MeV
Pulse width	3 μ s	4 μ s
Repetition rate	330 PPS	200 PPS
Length of acceleration tube	25 cm	50 cm
Beam current	>64 mA	>95 mA
Intensity of X ray	50 mGy/min	2 Gy/min
Voltage of electron gun	20 kV	20 kV

Concerning prevention of ionizing radiation hazards due to radioisotopes and others of MEXT (Ministry of Education, Culture, Sports, Science and Technology) in Japan, only electron LINACs with lower than 1MeV can be used outside radiation controlled areas and those with up to 4 MeV are only available for on-site inspection of bridges. Complying with these regulations, Uesaka M developed portable 950 keV/3.95 MeV X-band (9.3 GHz) LINAC X-ray generators for on-site nondestructive inspection [14, 15]. Configurations are shown in Figure 1.4, and parameters are listed in the Table 1.2.

The weight of 950 keV electron LINAC X-ray source part with the local radiation shielding and magnetron are only 44 kg and 49.5 kg, respectively, and the X-ray intensity of this system is 50 mGy/min at 1 m. The 3.95 MeV LINAC consists of 62 kg X-ray head with the target collimator of 80 kg, 62 kg RF power source and other utility box of 116 kg, and the X-ray intensity of this system is 2 Gy/min at 1 m.

1.3.2 Radiography detectors

Scintillators and semiconductor detectors are the most widely used detectors for imaging applications .

TABLE 1.3: Scintillators for imaging.

Scintillator	Density (g cm ⁻³)	ρZ_{eff}^4 (10 ⁶)	Light yield (photons /MeV)	$\Delta E/E$ (FWHM) at 662 keV (%)
CsI:Na	4.51	38	40,000	7.4
CsI:Tl	4.51	38	66,000	6.6
<i>CdWO</i> ₄	7.9	134	20,000	6.8
NaI:Tl	3.67	24.5	41,000	5.6
<i>Bi</i> ₄ <i>Ge</i> ₃ <i>O</i> ₁₂ (BGO)	7.1	227	9,000	9.0
<i>Lu</i> ₂ <i>SiO</i> ₅ (LSO)	7.4	143	26,000	7.9
<i>YAlO</i> ₃ (YAP)	5.5	7	21,000	4.3
<i>Ce</i> : <i>Gd</i> ₃ <i>Al</i> ₂ <i>Ga</i> ₃ <i>O</i> ₁₂ (Ce:GAGG)	6.63	45	57,000	5.2

1.3.2.1 Scintillators

Most of the X-ray imaging systems are based on scintillator, such as flat panel detectors and charge coupled device (CCD) cameras. Table 1.3 shows a variety of widely-used scintillators [16]. Compared with semiconductor detectors (Section 1.3.2.2) especially the silicon detector, many scintillators have higher densities and also higher efficient atomic number (Z_{eff}) and thus they are more efficient for detecting high-energy photons. However, the main disadvantage is worse energy resolution suffered from indirect conversion of photons into scintillation lights before lights are converted into electrical charge signals by photodetectors such photodiode, avalanche photodiode (APD), photomultiplier tube (PMT) and silicon photomultiplier (SiPM).

Flat Panels integrate in the same plate the scintillator and the photodiodes as shown in Figure 1.5. To ensure sub-millimeter spatial resolution at lower energies, flat panel detectors are usually built on thin scintillator screen and thus is inefficient for high-energy photons. The Perkin Elmer XRD0822 flat panel detector [17] has a fluorescent screen that consists of 200- μ m-thick GOS scintillator and a TFT/diode array fabricated on a single substrate amorphous silicon. The detector has a 20.5-cm field of view with a pixel matrix of 1024 \times 1024 at 200 μ m pitch.

A thin scintillator screen can be combined with digital CCD camera for nondestructive testing. Auditore L et al. developed a scintillator screen and CCD camera based X-ray tomography system for industrial applications (Figure 1.6)[18]. The CCD camera has 768 \times 512 pixel resolution with 9 \times 9 square pixels. In order to preserve the CCD camera from radiation damage, it has been set at 90° with respect to the beam direction and 100 cm far from the mirror reflecting the image from the scintillator screen to the camera. CCD camera systems are thought to have high resolution. However, the

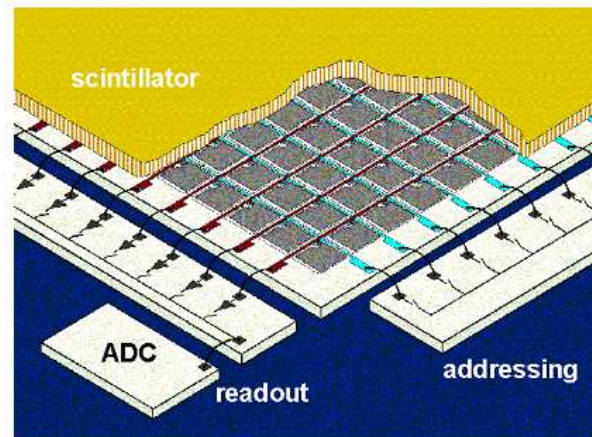


FIGURE 1.5: Schematic of a flat-panel detector.

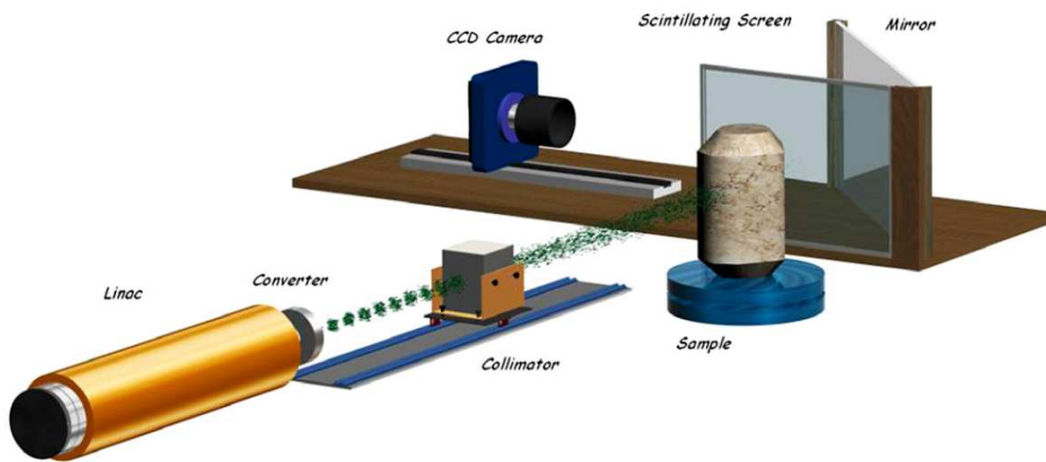


FIGURE 1.6: Schematic of a flat-panel detector.

scintillator screen is required to be optically transparent so that the image of attenuation in the object can be easily transferred to the CCD, as a result, the thickness of the imaging plate is just tens of micrometer which limits detection efficiency for high energy photons.

1.3.2.2 Semiconductor detectors

Recently room temperature semiconductor detectors such as CdTe, CZT and silicon detectors have been more and more applied in medical and industrial radiography. Compared with scintillator-based imaging systems, the main advantage is they directly convert photons into electron-hole pairs which are collected as electrical signals and thus they possess inherently better energy resolution than scintillators. In current-mode

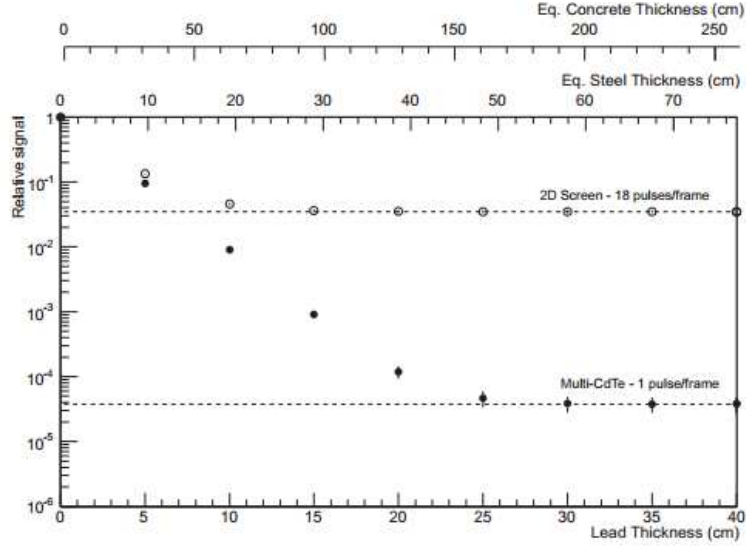


FIGURE 1.7: Dynamic ranges of scintillator screen and multi-CdTe detector

operation, the current generated per unit energy absorbed is higher than that generated in scintillators and leads to a better signal-to-noise ratio and a wider dynamic range.

The improved energy resolution of CdTe and CZT detectors leads to better contrast in energy dispersive imaging systems for relatively low photon energies and at a wide dynamic range of detector exposures, that is, for large variations of object thickness and for transmission or emission photons [19]. Estre N et al. constructed an X-ray imaging system based on CdTe detectors and compared the results of scintillator-based system as shown in Figure 1.7 [20]. The 2D scintillator detector allows to measure up to 10-cm lead that is equivalent to 20-cm steel or 65-cm standard concrete while the multi-CdTe limit is reached for 25-cm lead that is equivalent to 48-cm steel or 160-cm standard concrete. CdTe and CZT detectors have several disadvantages that prevent their wide use in imaging systems: low charge mobility and lifetime, poor hole collection, nonuniformity over large volumes and relatively high fabrication expenses. Besides, typical pixel CdTe detectors have thickness of lower than 2 mm and thus the detection efficiency is limited.

Silicon detectors have advantages of low cost, high mobility and full collection of electron-hole pair. Suffered from low atomic number and low density of silicon, silicon detectors are generally considered to be only efficient in the detection of low energy photons or charged particles. Typical silicon detectors have thickness of less than 0.5 mm. Though silicon detectors are inefficient for detecting high-energy photons suffered from their low density and low atomic number, researchers have been trying to construct high-energy X-ray imaging systems based on silicon detectors [21–24]. Katsuyama et al. [24] developed an X-ray computer tomography (CT) system with a 12 MeV linear

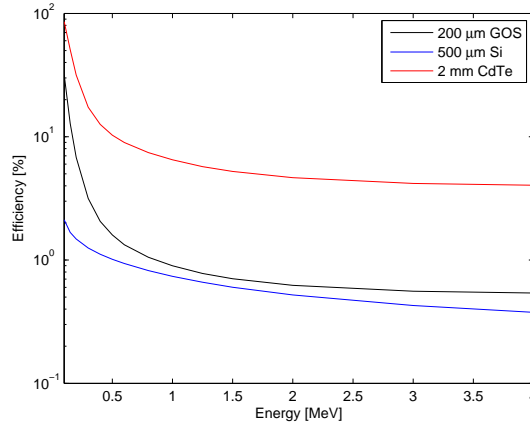


FIGURE 1.8: Detection efficiency of typical detectors for photons

accelerator (LINAC) X-ray source using 100 silicon detectors in a circular arc. They obtained images of irradiated fuel pellets .

1.3.2.3 Detection efficiency of traditional imaging detectors

Referred to NIST X-ray attenuation databases [25], we calculated detection efficiency of typical imaging detectors for photons with different energies as shown in Figure 1.8. For 1 MeV photons, efficiencies of the 200 μm thick GOS scintillator and 500 μm thick silicon detector are lower than 1%, and 2 mm thick CdTe detector has efficiency lower than 7%. Moreover, The detection efficiencies decrease rapidly with the increase of photon energy. Traditional imaging detectors are not suitable for high-energy X-ray applications suffered from their low detection efficiency.

1.4 Energy-integrating and photon-counting techniques

X-ray detectors are mainly working in two modes: energy-integrating mode and photon-counting mode. Detectors working in the energy-integrating mode integrate the total energy deposition of the incident X rays, while the number of discrete events is counted when they are working in photon-counting mode.

1.4.1 Energy-integrating technique

Benefiting from lower requirement about the readout electronics and X-ray intensity, most of the practical radiography systems are working in energy-integrating mode.

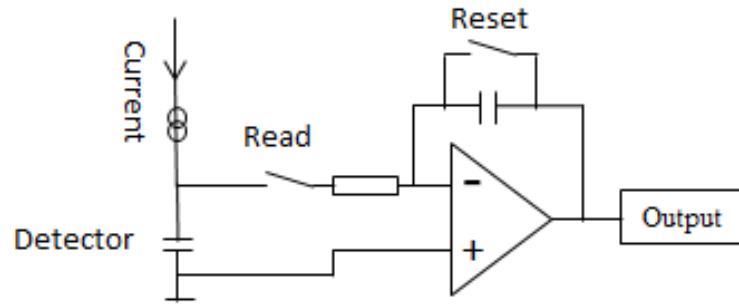


FIGURE 1.9: A schematic diagram of the energy-integrating circuit.

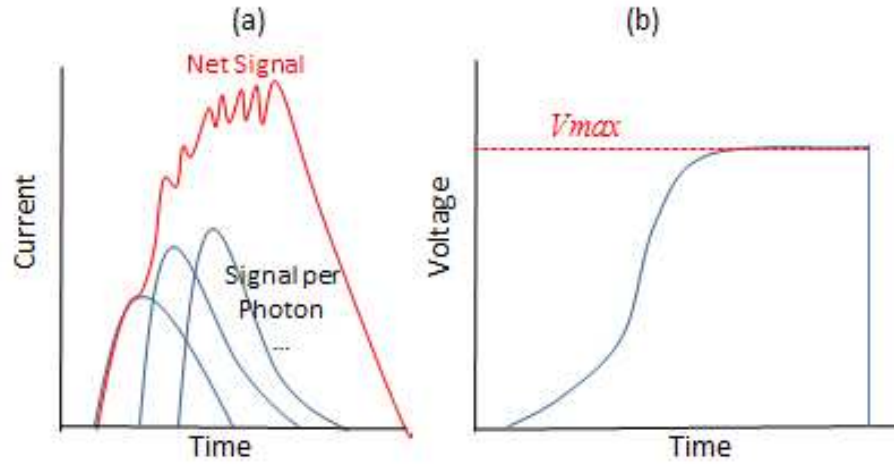


FIGURE 1.10: Signals of the energy integrating circuit. (a) Current signal. (b) Voltage signal.

A typical example of the integrating detector is the amorphous silicon flat panel. A current signal is generated when a photon is detected by the 2D detector, and the established current is then integrated by a circuit such as the one illustrated in Figure 1.9. The charging current and the voltage on the storage capacitor are illustrated in Figure 1.10(a) and Figure 1.10(b). The output signal is determined by the maximum potential on the storage capacitor which is essentially proportional to the integration of the deposited energy of incident photons.

However, detectors working in energy integrating mode suffer from limited dynamic range and sensitivity to dark current and electronic readout noise.

1.4.2 Photon-counting technique

Photon-counting detectors have been proposed to overcome the drawbacks of energy integrating detectors. A simplified block diagram of the photon-counting detector is

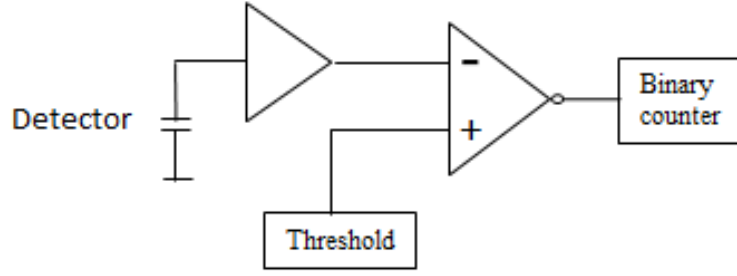


FIGURE 1.11: A schematic diagram of the photon-counting circuit.

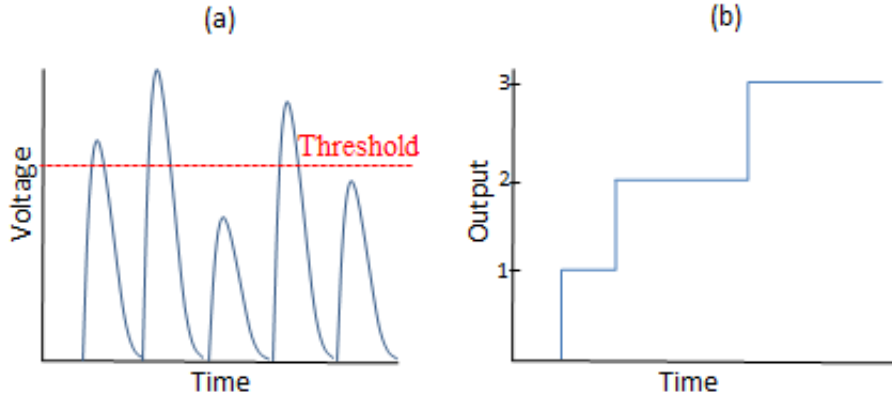


FIGURE 1.12: Analog and digital signals. (a) Voltage and threshold signals.(b) Counts of signals higher than threshold.

shown in Figure 1.11. A current signal is generated when a photon is detected by the detector, and it is then transferred to a preamplifier and a shaper and the voltage gain is compared with a threshold that is established by potentiometer or digital-to-analog converter (DAC). Voltage gains exceeding the threshold are treated as representative of a single photon (Figure 1.12(a)) and the number of events per pixel is counted (Figure 1.12(b)).

A key advantage of photon-counting technique over traditional energy-integrating technique is that the background noise can be effectively suppressed and the signal-to-noise ratio (SNR) of image is improved as a result. The setting of a threshold makes it possible to discriminate not only noise from signal, but also lower from higher energies. Strongly Compton scattered events can therefore be suppressed with mono-energetic sources reducing image blurring [26]. Furthermore, because the height of the voltage gain is proportional to the energy of the incident X-ray, another advantage of photon-counting technique is that thresholds can be adjusted to achieve energy discrimination in a polyenergetic beam. This information can be used to remove anatomical noise, quantify contrast uptake over a set of voxels, or perform material decomposition. In

addition, because pileup is no longer required, low-rate imaging can be performed and dynamic range of the imaging system is expanded.

Although the advantages and potentials of photon-counting systems have been recognized, the application of these systems has been hampered by the requirements of a large number of electronics, where the entire amplification, discrimination and digital logic chain has to be fit into a tiny area and a large amount of data has to be transferred to the computer and stored. Recent development on chip-level application-specific integrated circuit (ASIC) electronics has made it possible to provide fast, multichannel readout electronics for photon-counting X-ray imaging detectors.

1.5 Objectives

We are motivated to develop a new X-ray imaging system for on-site nondestructive testing of steel structures in nuclear power plants and concrete components in infrastructures. The system should satisfy the following requirements:

- A) The system is required to be of high sensitivity for decreasing the dose to environment and shortening imaging process time with low cost.
- B) The system should have a wide dynamic range for imaging thick samples, so the photon-counting technique is to be applied instead of traditional energy-integrating technique.
- C) The system should be capable of identifying 2 mm break of reinforcing bars inside concrete, so the intrinsic spatial resolution is required to be lower than 2 mm.

1.6 X-ray imaging system design

Silicon detectors would be suitable for constructing such an imaging system. They can be fabricated with low cost than compound semiconductors such as CdTe or CZT, and as a semiconductor detector, silicon detector has intrinsic better energy resolution than scintillators and thus is beneficial to realizing a better spatial resolution. The only disadvantage would be its low density and atomic number. However, if silicon strip detectors are used and the strips are oriented parallel to the incident beam (called edge-on), one can benefit by stacking edge-on silicon strip detectors for high-energy X-ray imaging because each strip functions as a pixel of the imaging device and the edge-on setup greatly increase the detection efficiency compared with traditional pixel detectors.

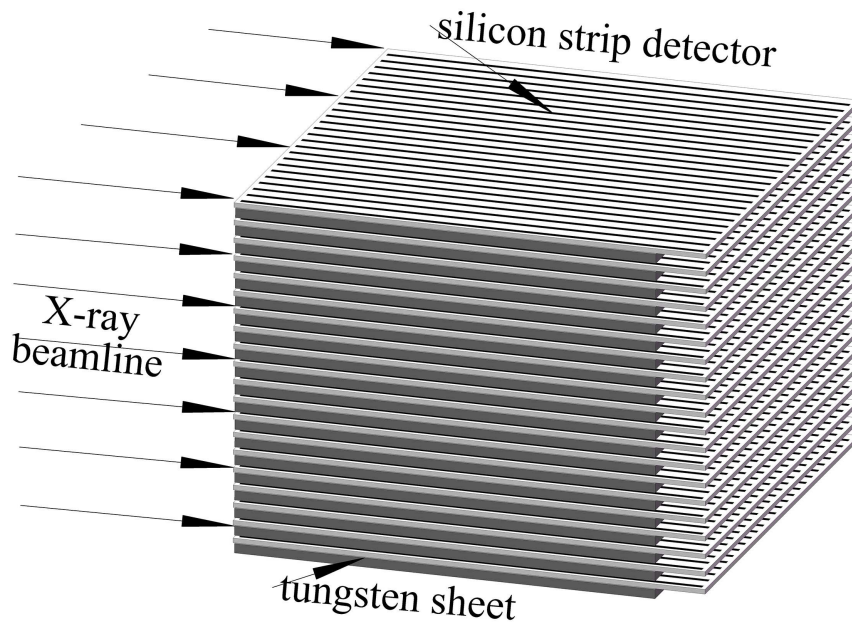


FIGURE 1.13: One detector module that consists of stacked silicon strip detectors and tungsten sheets.

It's calculated that an edge-on silicon detector with a length of 5 cm has an efficiency of over 70% for 1 MeV photons.

The initial design of the X-ray imaging system includes the detector module and the collimator module.

1.6.1 Detector module

The detector module (Figure 1.13) consists of a stack of 20 units. One unit is composed of an edge-on silicon strip detector mounted on one print circuit board (PCB) and a tungsten plate above the silicon detector. The tungsten plates are used to shield scattered photons inside the detector module. One strip detector has 50 channels and the sensitive region of the whole detector is 0.5 mm (thickness) \times 50 mm (width) \times 50 mm (length). One unit has a thickness of 2.5 mm.

1.6.2 Collimator module

A tungsten collimator module is designed to absorb the scattered photons from the thick object. The collimator module is made of 50 tungsten plates. The thickness of each tungsten plate is 0.5 mm and every two tungsten layers are placed 0.5 mm apart. Primary X-ray photons (without interaction with test structure) can be detected by

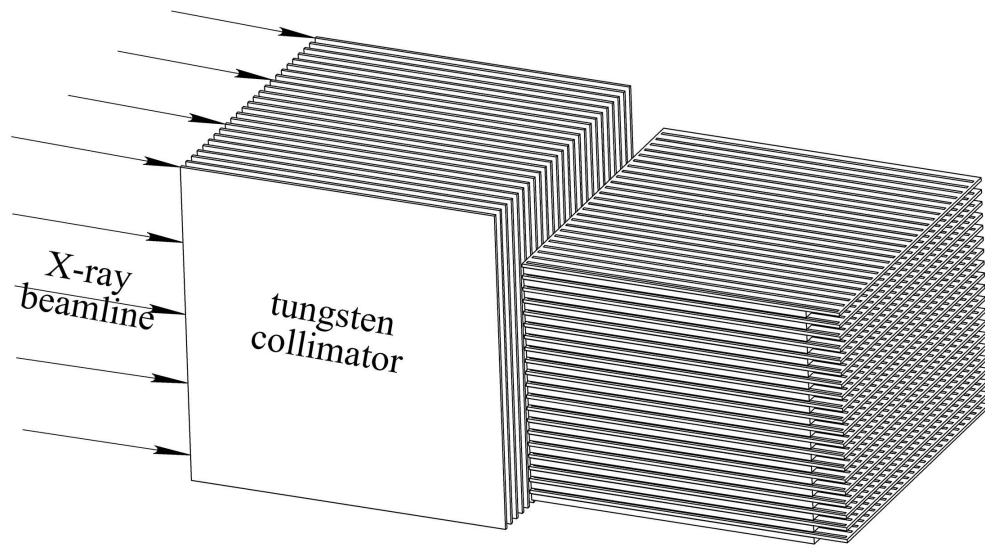


FIGURE 1.14: Assembly of detector module and collimator module.

edge-on detector channels through the slits. The assembly of the collimator module and detector module is shown in Figure 1.14.

Chapter 2

System design based on Monte Carlo simulation

In order to optimize the design of a detector system, experimental collaborations typically spend considerable effort in modeling the detector as complete as possible, and this is especially important for understanding the impact of each part of the system before investing time and money in constructing the apparatus. This is the main advantage of using Monte Carlo Simulation, which makes it easy to optimize the different system parts and parameters with high flexibility.

The Monte Carlo method [27], as an important and powerful numerical technique for calculating probabilities and related quantities by using sequences of random numbers [28], has been widely used in nuclear and particle physics, astrophysics and space science, medical physics, radiation protection, etc.

In detector system simulations, the Monte Carlo method is generally applied in three stages: event generation, particle transport and detector simulation. By sampling events from the corresponding probability distributions, complex physical processes can be well simulated. In this way, distributions of final state particles from fundamental interactions is predicted using event generator codes, the passage of particles through matter is simulated with particle transport codes and the response of a detector is reproduced by converting particle interactions in the detector to measurement signals.

2.1 Widely used Monte Carlo codes

There are a lot of well-developed Monte Carlo method based packages capable for X-ray/gamma-ray imaging system simulation, such as MCNP [29], EGS [30], FLUKA

[31], GEANT4 [32, 33], etc.

2.1.1 MCNP

MCNP, as a general-purpose Monte Carlo N-Particle code developed by Los Alamos National Laboratory, can be used for neutron, photon, electron, or coupled neutron/photon/electron transport. The code treats an arbitrary three-dimensional configuration of materials in geometric cells and uses pointwise cross-section data [34]. MCNP has many standard tallies to make it easy for the user to obtain the desired result as a function of cell or surface, energy, etc. For example, F8 card combined with cell number and energy bins can be used to calculate energy spectra of photons and electrons that deposit in concerned geometries, which are generally used for detector simulation. MCNP is a highly general user oriented application and more accurate compared with other simulation codes, and even those who have no experience of programming can run MCNP simulations by simply filling input files. However, MCNP suffers from poor interface and it is difficult and sometimes impossible for users to format the output data and extract intermediate information about the particle passage.

MCNP is the most widely used in neutron simulations, especially for reactor design and analysis.

2.1.2 EGS

The EGS (Electron-Gamma Shower) code system, written in FORTRAN and developed by Stanford Linear Accelerator Center (SLAC, US) and High Energy Accelerator Research Organization (KEK, Japan), is a general purpose package for the Monte Carlo simulation of the coupled transport of electrons and photons in an arbitrary geometry for particles with energies above a few keV up to several hundred GeV. The user defines and controls an EGS5 shower simulation by initializing, tallying, and altering variables found in COMMON blocks shared by user code MAIN and a set of EGS5 subroutines. The user can access and manipulate variables at points in the simulation specified by the user.

The EGS code has been used in a wide variety of applications, particularly in medical physics and radiation measurements studies.

2.1.3 FLUKA

FLUKA, developed in FORTRAN, is a fully integrated Monte Carlo simulation package for the interaction and transport of particles and nuclei in matter. Implementation and improvement of sound and modern physical models are always the highest priority in the design and development of FLUKA. As a result, about 60 different particles can be simulated with high accuracy by FLUKA about the interaction and propagation in matter. Like MCNP code, no programming is required from the user for most applications, and a number of user interface routines are available for users with special requirements.

FLUKA has been most extensively applied in designs of proton and electron accelerator shielding and target. It can also be applied in calorimetry, activation, dosimetry, detector design, accelerator driven systems, cosmic rays, neutrino physics, radiotherapy, etc.

2.1.4 GEANT4

GEANT4, implemented in the C++ programming language, is the first large scale object-oriented software toolkit for simulating the passage of particles through matter. A complete range of functionalities are included for managing geometry, tracking, detector response, runs, events, particle definitions, visualization and user interfaces. Its modular architecture allows users to load and use only the components needed. Meanwhile, it also allows users to customize and extend the toolkit in all the domains. Compared with softwares such as MCNP and EGS, an important advantage of Geant4 is that the source codes are completely open and no specific software license is needed for its use, as a result, almost all information that users are interested in can be extracted with proper programming implementation.

Geant4 has been used by a wide scientific community worldwide in nuclear and accelerator physics, studies in medical and space science, particularly in high energy physics. Furthermore, benefiting from the object-oriented technology, GATE [35], a simulation toolkit for positron emission tomography (PET) and single photon emission computer tomography (SPECT) is developed based upon Geant4.

2.1.5 Other codes

Other Monte Carlo codes, such as Penelope [36], MORSE [37], SRIM [38], PHITS [39], et al. are also widely used in a variety of applications.

Benefitting from the object-oriented methodology and convenience of extracting all interesting information, GEANT4 is chosen to analyze and design the X-ray imaging system. Because concrete structures are usually more regular in geometry compared with steel structures and thus it is easier to analyze and evaluate the system, the material of samples in the simulation is set to be concrete. In order to satisfy the requirements listed in section 1.6, the key point of the simulation is to decrease the contribution from the scattering components while keeping high detection efficiency of primary photons from the X-ray generator. The 3.95 MeV portable X-ray generator was chosen in the simulation. The simulation was proceeded with the following steps:

- 1) Calculate energy spectrum of the X-ray source;
- 2) Investigate interaction between X-ray photons and sample;
- 3) Calculate the response of one detector module to the X ray;
- 4) Evaluate tungsten shielding and collimator module;
- 5) Summarize the results and form a suggestion for the whole imaging system.

2.2 Energy spectrum of the X-ray source

The X-ray target is composed with one 0.5-mm-thick tungsten circular disk and one 1.6-mm-thick copper circular disk behind, and the diameter of the two disks is 5.0 mm. The 3.95 MeV electron beam with a diameter of 3 mm bombards the tungsten target and the bremsstrahlung X-ray photons are generated. The high-Z tungsten layer acts electron-gamma converter while the copper layer acts as a filter for electrons from the source and low-energy bremsstrahlung photons. The output X ray is confined within a cone angle of 15° . The geometry of the X-ray source simulation is shown in Figure 2.1 and the spectrum is obtained as shown in Figure 2.2.

The peak energy of the X ray is between 0.2 and 0.4 MeV, the average energy is 0.82 MeV and about 8.5% of all generated photons have energy higher than 2 MeV.

To reduce calculation time and improve statistics of simulation, the obtained energy spectrum is written into the X-ray source in the following simulations. Because we are interested in inspecting concrete structures as thick as 1 m, which is more than 100 times of the target size and 20 times of the detector length (5 cm), the X-ray source is treated as a monodirectional source and photons homogenously emit from a $R5.0$ cm (fully covers the detector module with a cross section of $5\text{ cm} \times 5\text{ cm}$) circular disk.

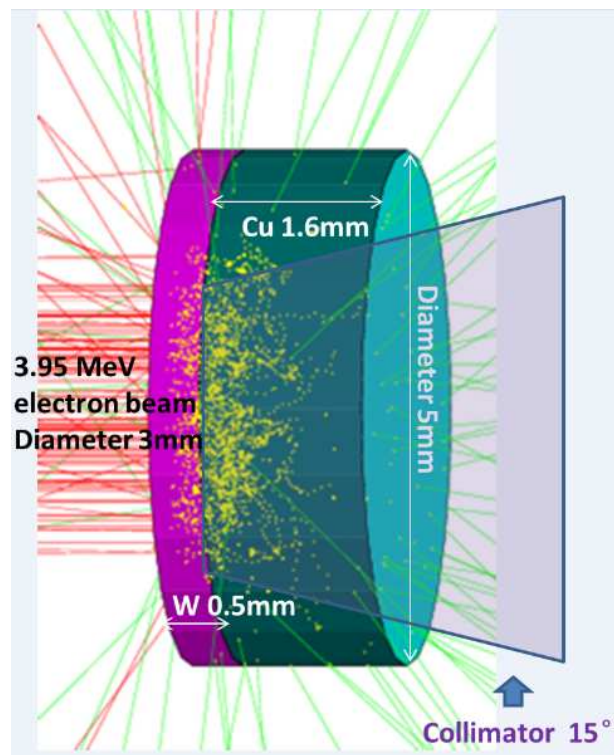


FIGURE 2.1: Geometry of the X-ray target

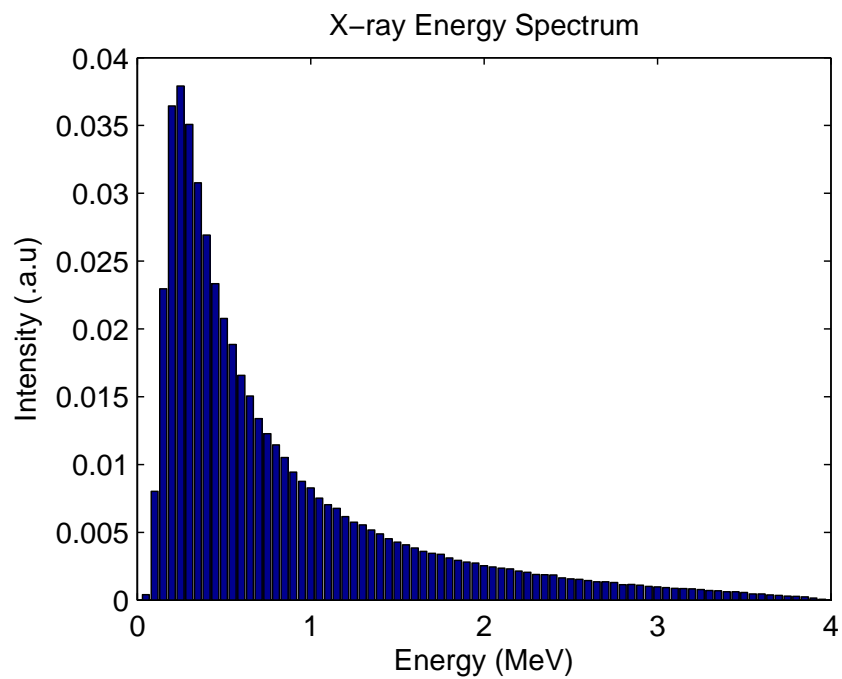


FIGURE 2.2: Energy spectrum of the 3.95 MeV X-ray source

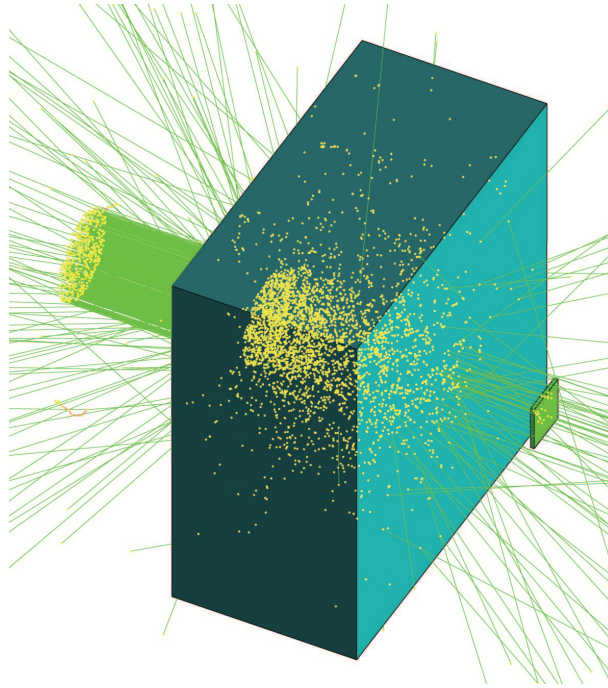


FIGURE 2.3: Geometry of the X-ray attenuation simulation

TABLE 2.1: X-ray attenuation and scattering after penetrating concrete of different thicknesses

Thickness (cm)	20	40	60	80	100
Intensity	1.82E-02	1.98E-03	1.75E-04	4.59E-05	4.78E-06
Intensity-Primary	1.27E-02	1.27E-03	2.85E-04	2.74E-05	8.06E-06
Scatter/Primary ratio	0.43	0.56	0.63	0.67	0.69
Average energy (MeV)	1.65	2.21	2.53	2.73	2.87

2.3 X-ray attenuation and scattering in concrete

The geometry of simulations is demonstrated in Figure 2.3. A plane with a cross section of $5\text{ cm} \times 5\text{ cm}$ is placed at 10 cm behind the back surface of concrete block (cross section of $40\text{ cm} \times 40\text{ cm}$ and thickness of 20 cm, 40 cm, 60 cm, 80 cm, and 100 cm) and all photons incident on this plane are recorded. Primary photons (without interaction with the concrete) and scattered photons are recorded separately.

The obtained spectra are shown in Figure 2.4, Figure 2.5, Figure 2.6, Figure 2.7 and Figure 2.8, respectively. The attenuation of primary photons, the scattering-to-primary ratios and average energy of all photons are summarized in Table 2.1.

It can be seen that X ray spectrum is greatly hardened after penetrating thicker

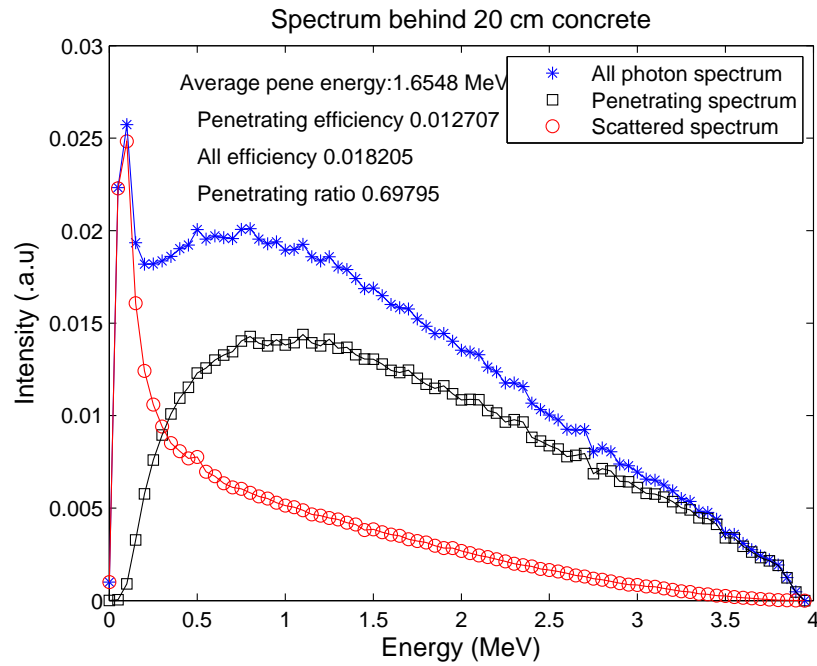


FIGURE 2.4: Spectrum at 10 cm behind 20-cm-thick concrete

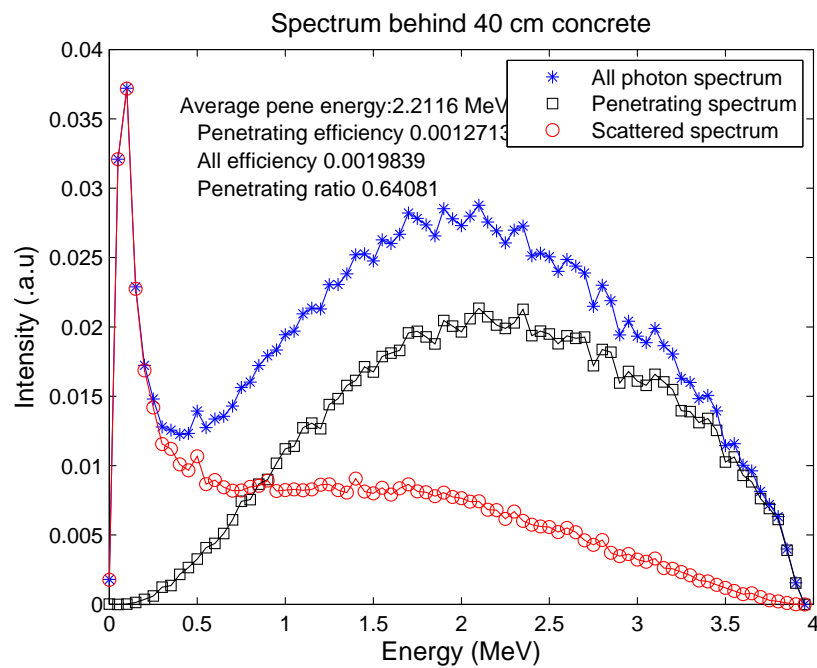


FIGURE 2.5: Spectrum at 10 cm behind 40-cm-thick concrete

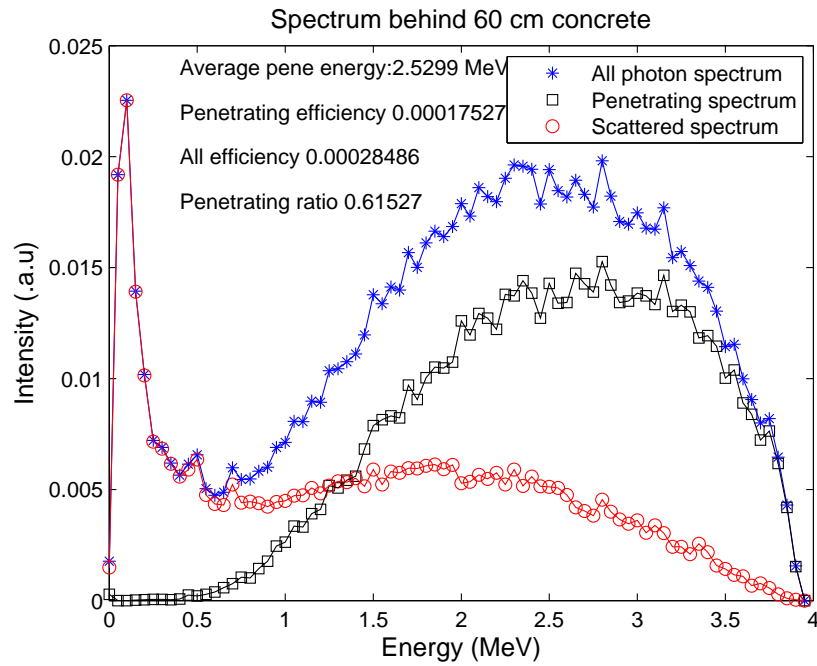


FIGURE 2.6: Spectrum at 10 cm behind 60-cm-thick concrete

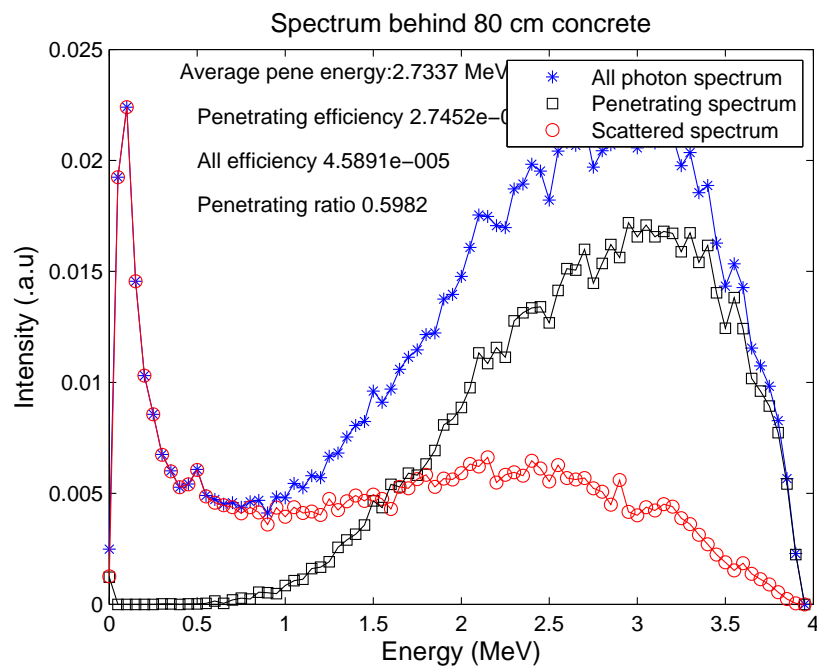


FIGURE 2.7: Spectrum at 10 cm behind 80-cm-thick concrete

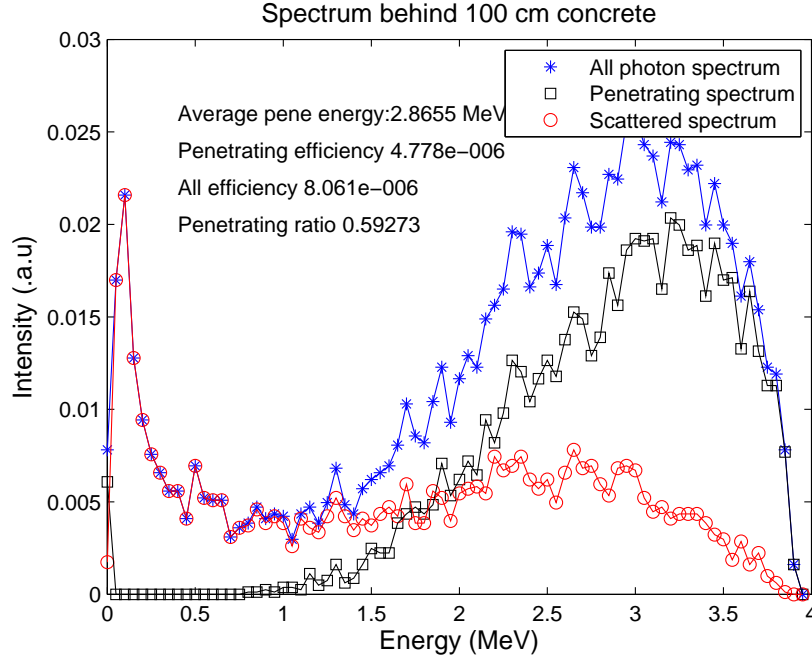


FIGURE 2.8: Spectrum at 10 cm behind 100-cm-thick concrete

concrete. A 20-cm-thick concrete attenuates X ray by about one order but the attenuation is smaller when the concrete is thicker because of the hardening effect. In addition, the scatter-to-primary ratio increases with the concrete thickness. The beam hardening effect and scattering degrade spatial resolution of X-ray imaging system. We cannot decrease the beam hardening because it is the nature of interaction between photon and other substances, but we have to suppress the scattering to decrease the degradation of spatial resolution.

2.4 Scattering decrease with object-to-detector distance

Different from the primary photons, track of the scattered photons diverges in direction, so it is anticipated that the scattering contribution could be lower with larger object-to-detector distance. Because concrete with a thickness of 20 cm leads to about one order's attenuation, the simulation time would be more than one order higher in order to obtain similar statistics. A thickness of 40 cm permits a good assessment of the interactions between photons and concrete and also requires reasonable simulation time, as a result, a concrete with a thickness of 40 cm and a cross section of 40 cm \times 40 cm is taken into consideration in the following simulations.

The spectra on a 5 cm \times 5 cm plane at 10/20/30/40/50 cm behind the back surface of the concrete are calculated and shown Figure 2.9, Figure 2.10, Figure 2.11, Figure

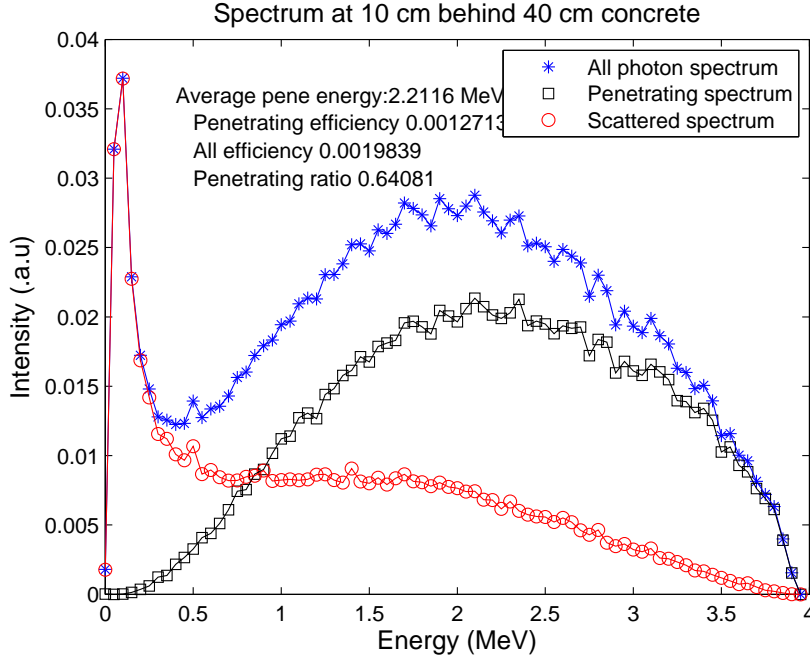


FIGURE 2.9: Spectrum at 10 cm behind 40-cm-thick concrete

TABLE 2.2: Scatter-to-primary ratios at different object-to-detector distances

Distance (cm)	10	20	30	40	50
Scatter/primary	0.56	0.28	0.17	0.11	0.08

2.12, and Figure 2.13, respectively. The dependence of scatter-to-primary ratio on the object-to-detector distance is summarized in Table 2.2.

The scattering contribution is greatly lowered when the detector is placed further to the object, and scatter-to-primary ratio is only 0.11 when the detector is placed at 40 cm to the object. According to the figures, low-energy scattering photons are much more lowered than high-energy scattering photons. This is because low-energy scattering photons originate from severe Compton scattering while high-energy photons originate from slight Compton scattering. Considering that detectors are more sensitive to low-energy photons than to high-energy photons, the spatial resolution degradation as a result of scattering in the object can be greatly alleviated.

Even if we consider the fan-out emitting of the X-ray source, this improvement still exists. Because the scattered photons originate closer to the detector compared with the primary photons, the scattered photons decrease faster than primary photons. This effect is basically because of the difference between the effective solid angle for the scattered and primary components. However, the detector cannot be placed too far away

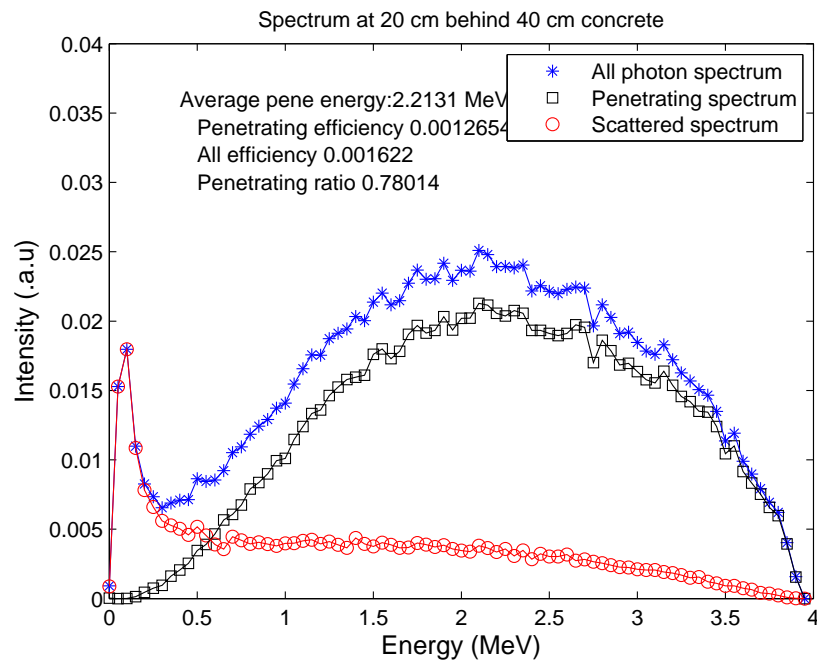


FIGURE 2.10: Spectrum at 20 cm behind 40-cm-thick concrete

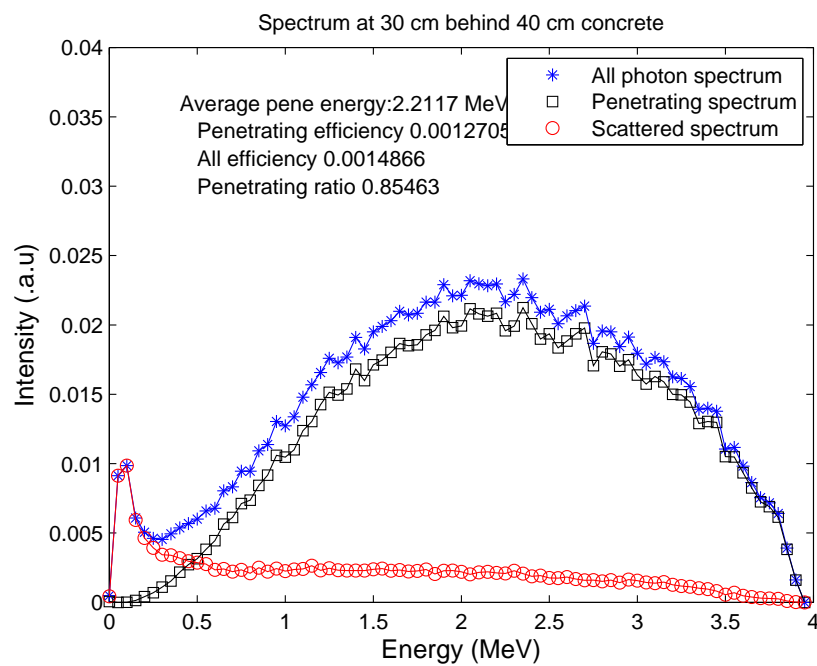


FIGURE 2.11: Spectrum at 30 cm behind 40-cm-thick concrete

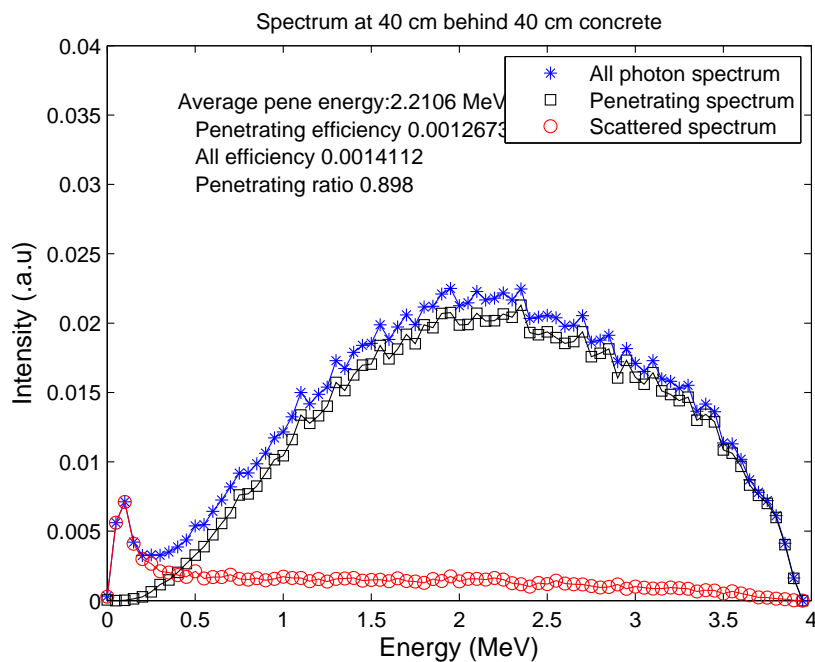


FIGURE 2.12: Spectrum at 40 cm behind 40-cm-thick concrete

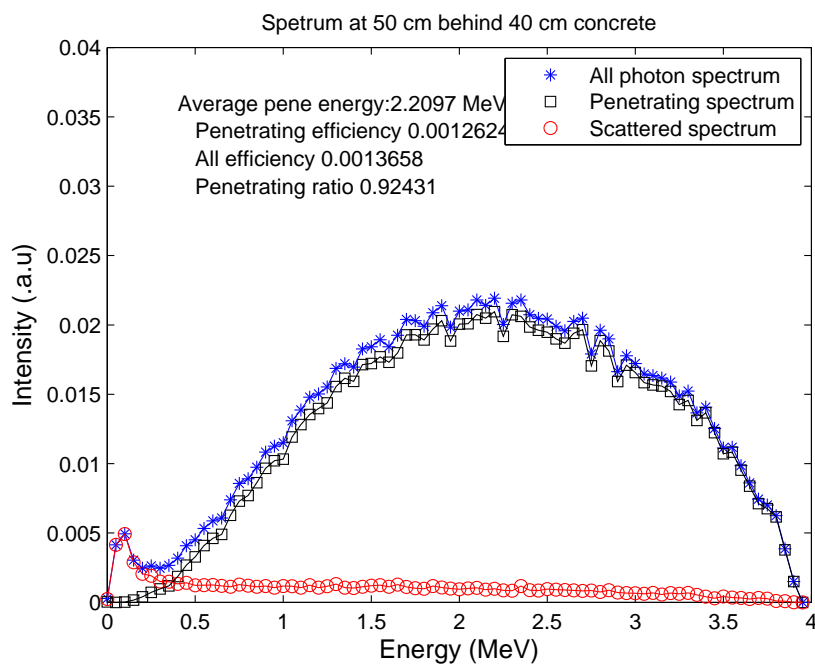


FIGURE 2.13: Spectrum at 50 cm behind 40 cm concrete

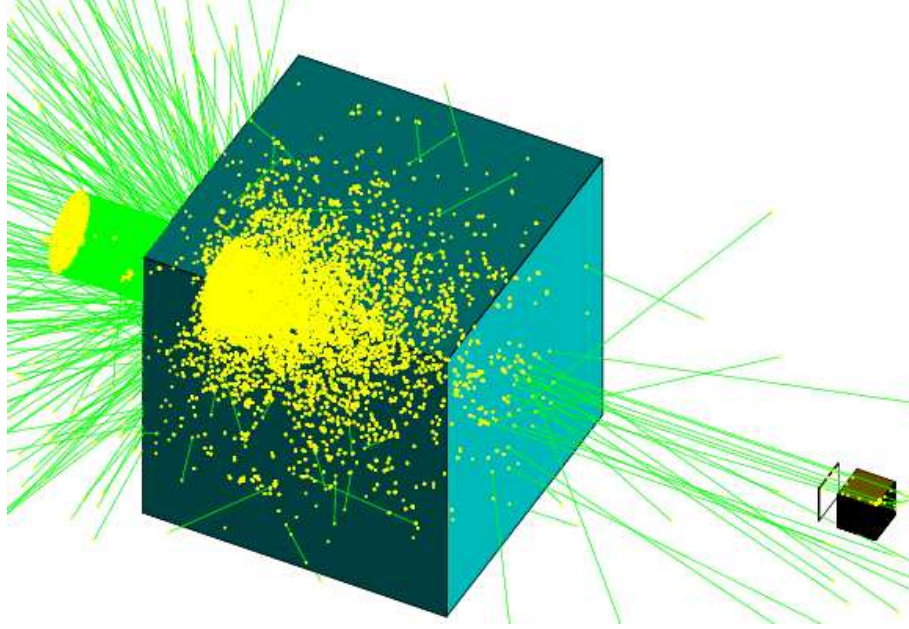


FIGURE 2.14: Geometry of concrete and detector module. The detector module is composed of 20 stacked 50-channel silicon strip detectors.

from the object because it also decreases the detection efficiency. The trade-off between the sensitivity and scattering suppression should be evaluated based on the practical situation of imaging.

2.5 Detector module response

A detector module consisting of 20 stacked layers of 50-channel silicon strip detectors is considered, and each channel has a cross section of $0.5 \text{ mm} \times 1 \text{ mm}$ and a length of 5 cm. Geometry of the simulation is demonstrated in Figure 2.14. A plane with a cross section of $5 \text{ cm} \times 5 \text{ cm}$ is placed at 40 cm behind the concrete block to record photons incident on the detector stack. The detector module is placed at 5 cm behind the plane, and 1000 channels are described separately in order to discriminate scattering in the detector module. A cross section of the detector module is shown in Figure 2.15.

Spectra of the primary and scattered photons incident on the plane are shown in Figure 2.16, and the scatter-to-primary ratio is 0.126.

Spectra of the primary and scattered photons incident on the 1000 silicon channels are shown in Figure 2.17, and the scatter-to-primary ratio is 6.28. The spectrum of deposited energy in all 1000 silicon channels is shown Figure 2.18. Besides, distribution of the event number when one photon is detected by the module is shown in Figure 2.19, and the average event number is 3.22.

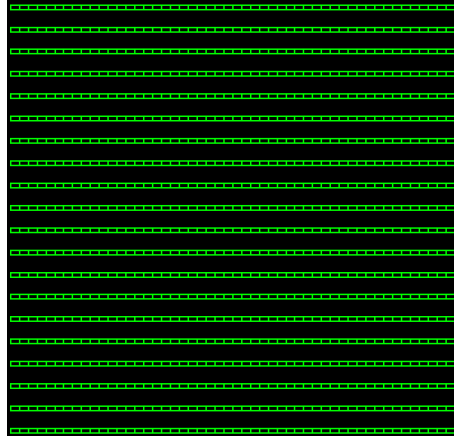


FIGURE 2.15: Cross section of the detector stack. Each silicon strip detector is divided into 50 individual channels.

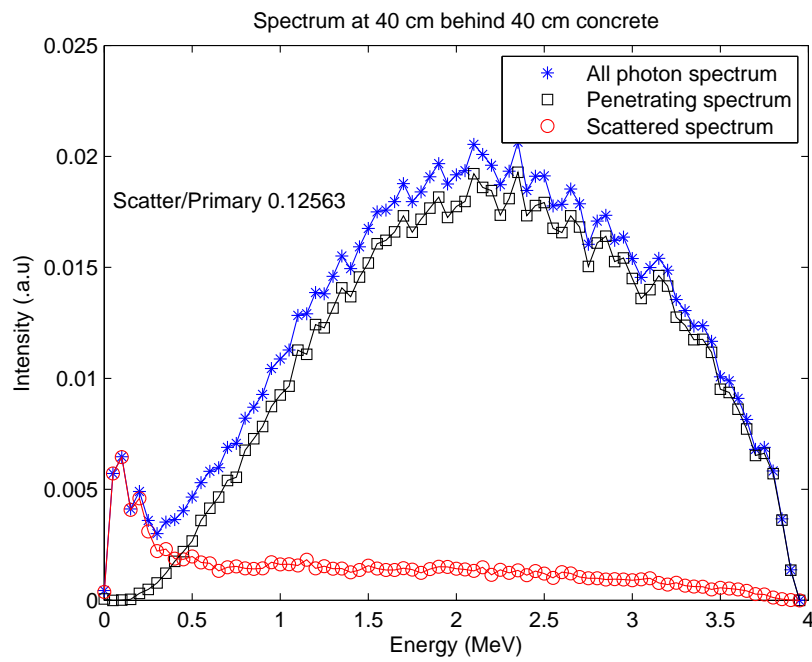


FIGURE 2.16: Photons incident on a plane in front of the detector module. Primary photons and scattered photons are recorded separately.

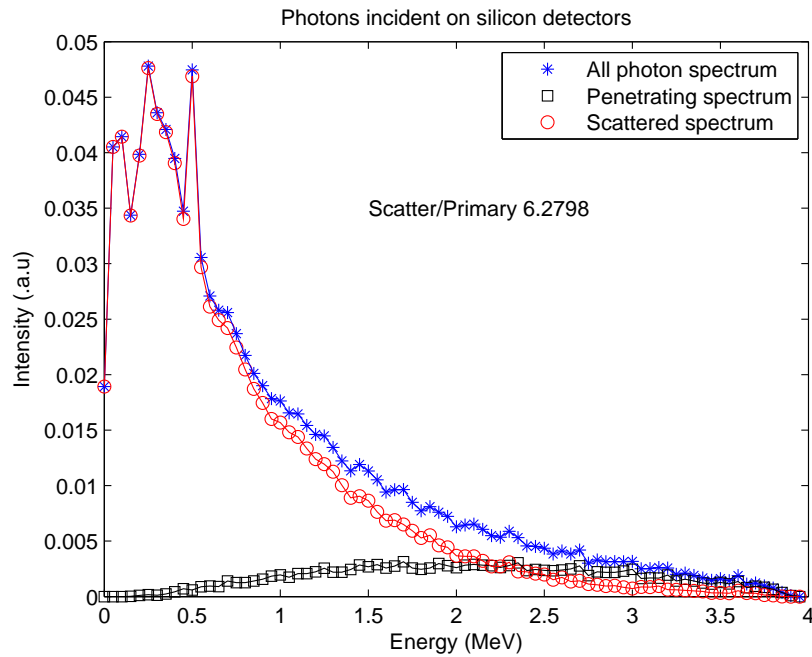


FIGURE 2.17: Photons incident on the 1000 silicon channels. Primary photons and scattered photons are recorded separately.

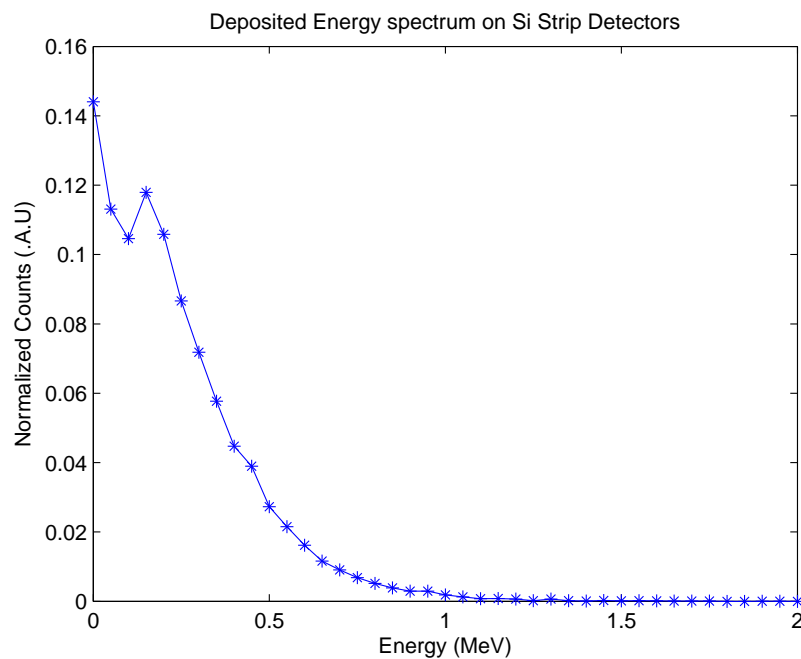


FIGURE 2.18: Spectrum of deposited energy on 1000 channels.

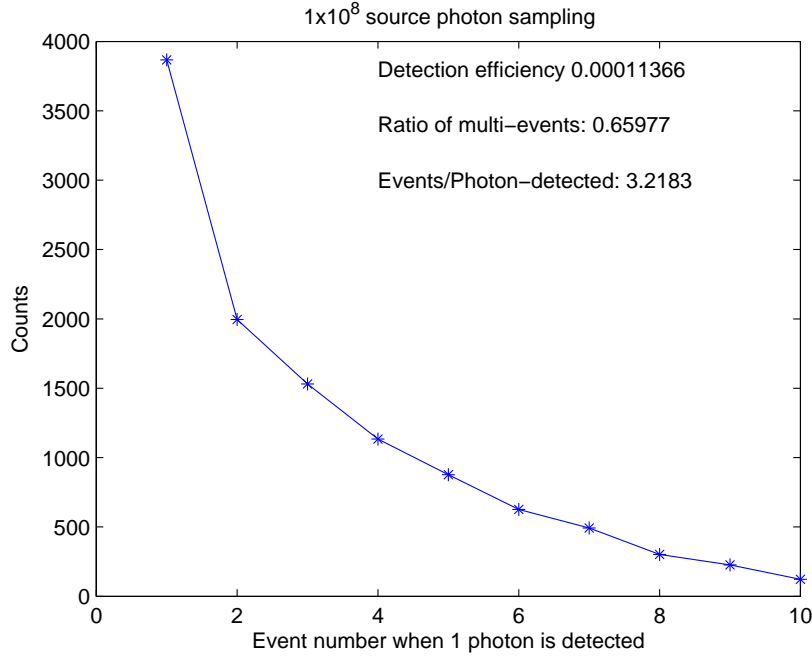


FIGURE 2.19: Event number when one photon is detected.

According to these results, photons are greatly scattered and a lot of scattered photons are detected by the detector stack. The stack geometry improves sensitivity of the imaging system greatly but suffers from a degradation of spatial resolution. Segmentation of the stacked strip detectors and anticoincidence rejection can be used to optimize the spatial resolution with small sensitivity loss, however, this also enforces a higher requirement about the readout electronics and data acquisition (DAQ) system.

2.6 Evaluation of PCB, tungsten shielding and tungsten collimator

Because the scattering in the detector module is severe, it is necessary to evaluate the effects of structural components such as PCB. Tungsten shielding and tungsten collimator have the potential of reducing scattering but also need to be evaluated.

In order to quantitatively evaluate imaging capability of the system for small interior structures, two iron bars with R1.0 cm and R0.5 cm are described inside the 40 cm thick concrete and their images are simulated. Geometry of the iron bars inside the concrete and the projected view of iron bars on the detector stack are shown in Figure 2.20.

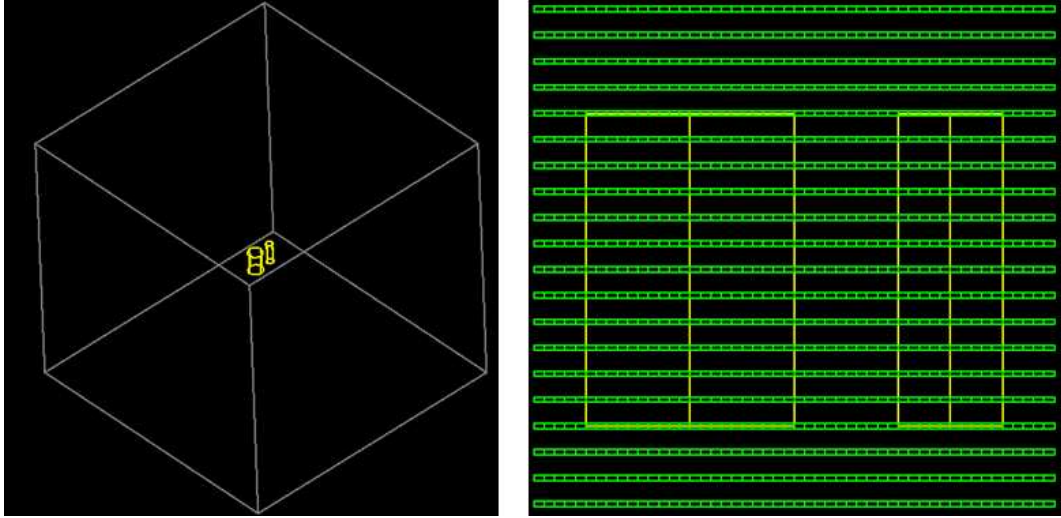


FIGURE 2.20: Concrete and the interior iron bars and the projected view of iron bars on the detector stack

2.6.1 Influence of PCBs

PCBs with an area of $5 \text{ cm} \times 5 \text{ cm}$ and a thickness of 1.5 mm placed under each detector layer are considered. A total of 8×10^9 source events are simulated.

Spectra of the photons incident on the silicon channels are shown in Figure 2.21 and the spectrum of deposited energy is shown in Figure 2.22. The scatter-to-primary ratio (10.71) is higher than the case without PCBs, and there are more low-energy ($< 200 \text{ keV}$) deposition events, indicating scattering is enhanced after PCBs are considered.

The event number and deposited energy on each channel are recorded separately. The counts over all 1000 channels are shown in Figure 2.23, and we can see the R0.5 cm iron bar and a clearer R1.0 cm iron bar. However, the images are blurred because of the scattering inside the detector stack. In the red rectangular area of Figure, I normalize the total counts over the channels with the same channel number by the total counts over the 30th channels and obtain the horizontal profile of the phantom concrete (shown in Figure 2.24). The horizontal profile when a 200-keV threshold is set to all channels is also shown, and the contrast is a little improved because more scattered events compared with the primary events are removed.

2.6.2 Tungsten shielding inside the detector stack

The tungsten shielding is composed of 20 tungsten sheets that are inserted into the detector stack. Each tungsten sheet has an area of $5 \text{ cm} \times 5 \text{ cm}$ and a thickness of 0.5

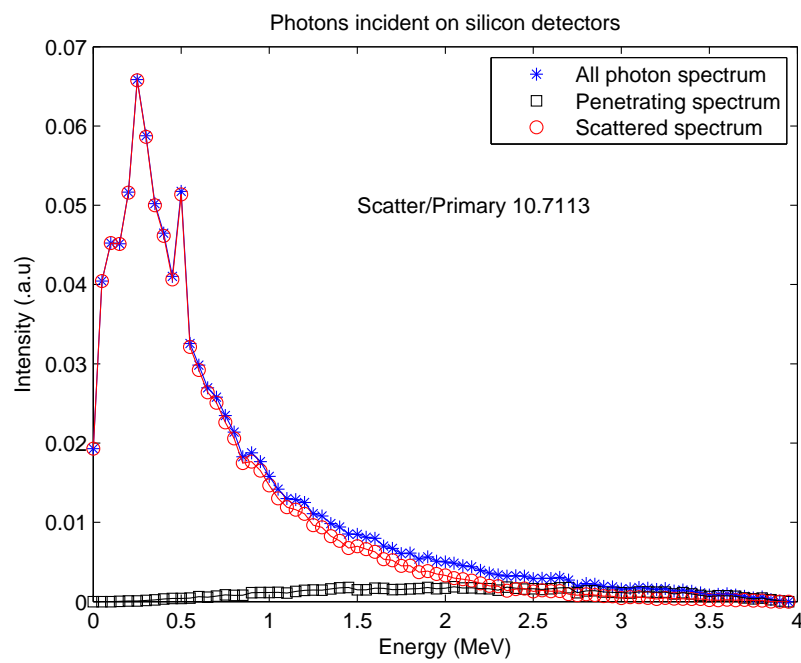


FIGURE 2.21: Spectra of photons incident on the 1000 silicon channels. PCBs are placed below each detector.

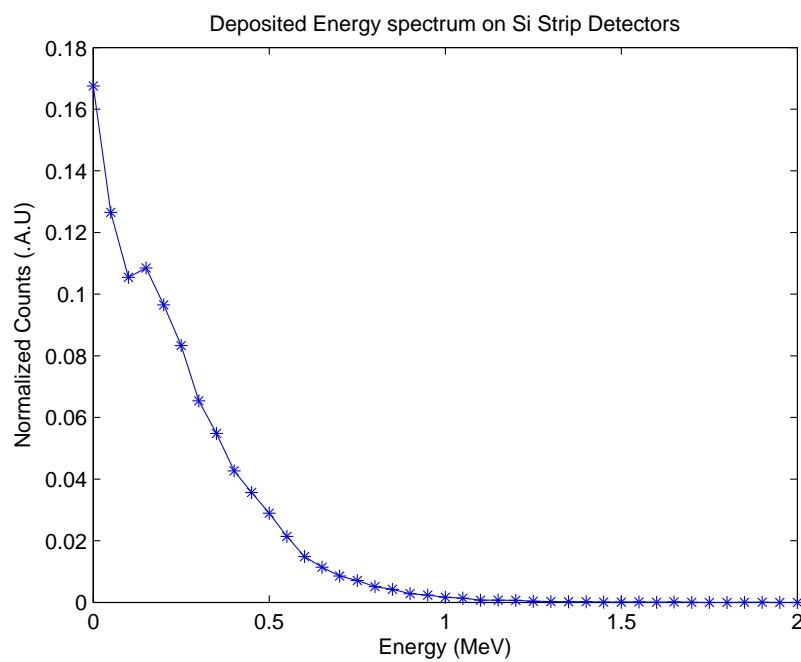


FIGURE 2.22: Spectrum of deposited energy on 1000 channels. PCBs are placed below each detector.

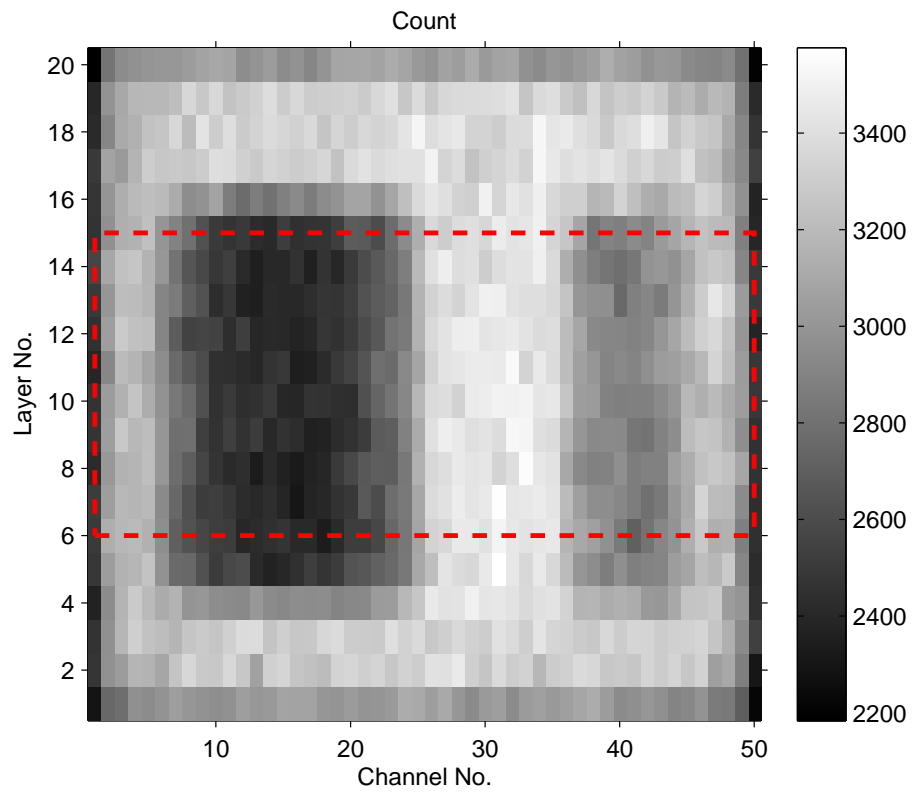


FIGURE 2.23: Image of the phantom concrete. PCBs are placed below each detector.

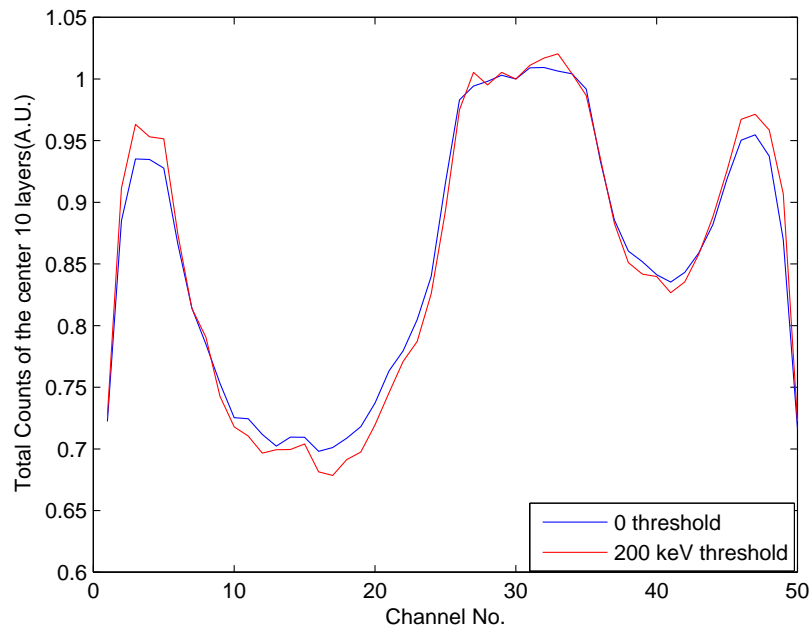


FIGURE 2.24: Horizontal profiles of the red rectangular area without/with threshold. PCBs are placed below each detector.

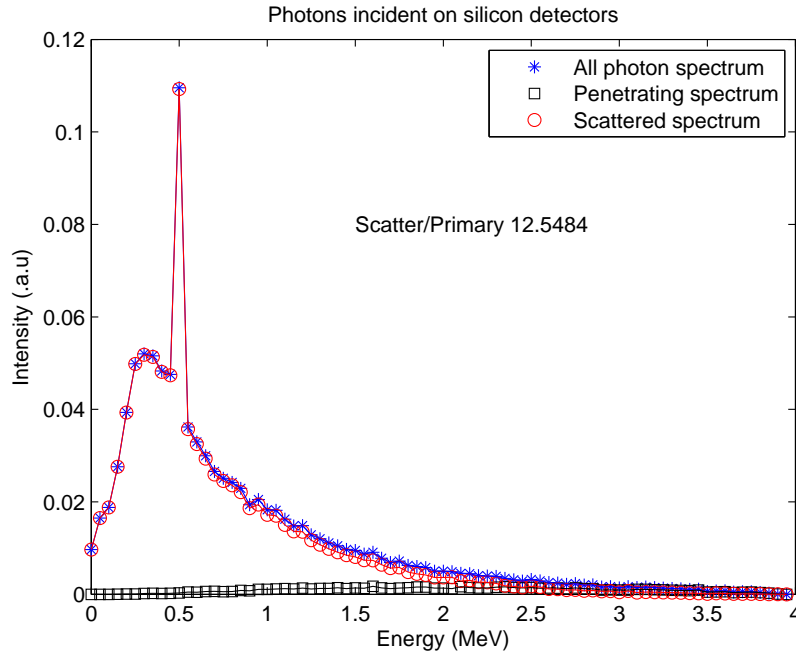


FIGURE 2.25: Spectra of photons incident on the 1000 silicon channels. Tungsten sheets are placed inside the detector stack.

mm. PCBs described in section 2.6.1 are also considered. A total of 8×10^9 source events are simulated.

Spectra of the photons incident on the silicon channels are shown in Figure 2.25 and the spectrum of deposited energy in all channels is shown in Figure 2.26. The scatter-to-primary ratio is even higher (12.55) and the 511 keV annihilation peak can be clearly seen, on the other hand, ratio of the low-energy deposition events are slightly reduced.

Image of the phantom concrete is shown in Figure 2.27, and the horizontal profiles without threshold and with a 200-keV threshold are shown in Figure 2.28. Because the tungsten sheets stops low-energy scattering but lead to higher scattering, the contrast improvement as a result of the 200-keV threshold shown in the previous section almost diminishes.

2.6.3 Tungsten collimator in front of the detector stack

Collimator composed of tungsten sheets vertical to the detector surface is denied because they cover half of detectors' sensitive area and the efficiency of the imaging system is decreased as a result. Therefore, I only evaluate tungsten collimator that is composed of horizontal sheets in front of the detector module. Twenty horizontal tungsten sheets are placed 35 cm in front of the detector stack. Each tungsten sheet has

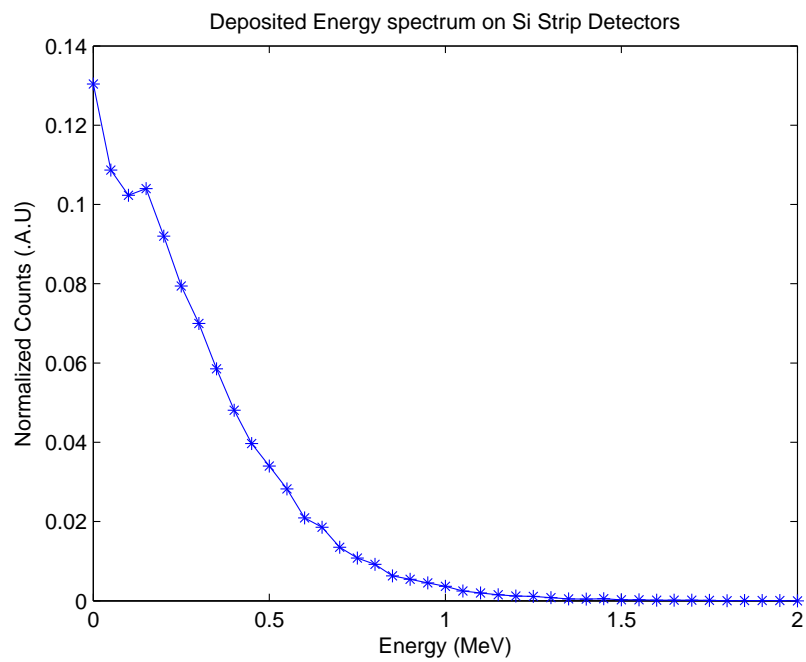


FIGURE 2.26: Spectrum of deposited energy on 1000 channels. Tungsten sheets are placed inside the detector stack.

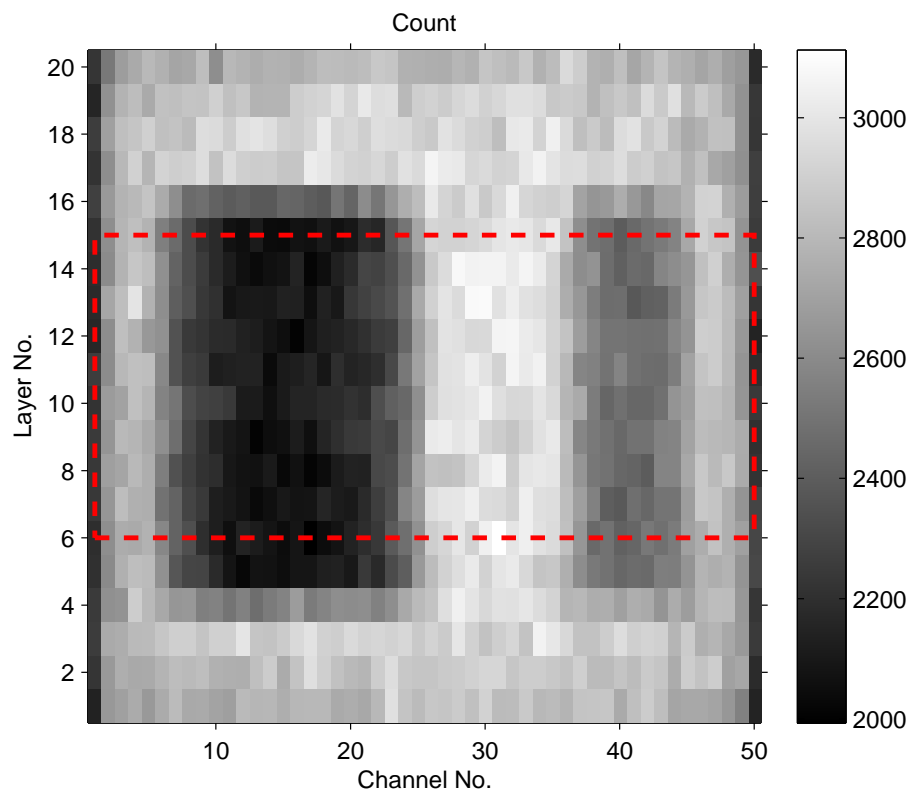


FIGURE 2.27: Image of the phantom concrete. Tungsten sheets are placed inside the detector stack.

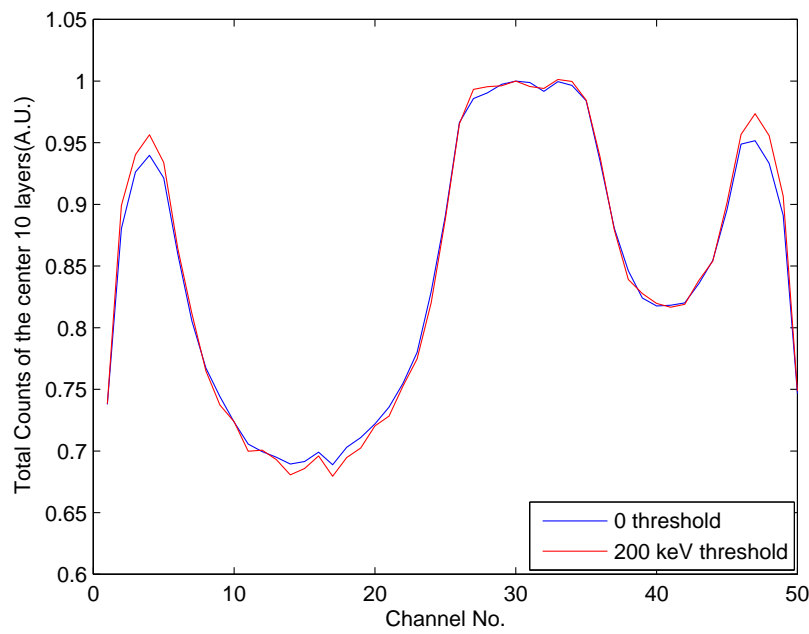


FIGURE 2.28: Horizontal profiles of the red rectangular area without/with threshold. Tungsten sheets are placed inside the detector stack.

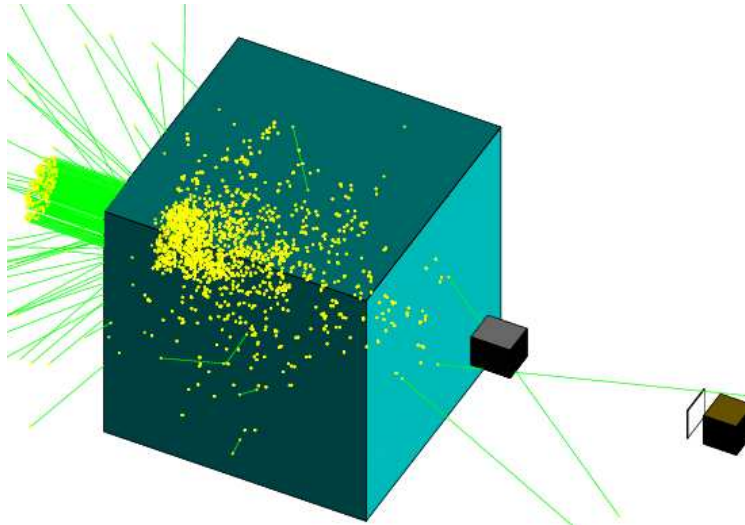


FIGURE 2.29: Geometry of concrete, tungsten collimator and the detector stack.

a size of 5 cm (width) \times 6 cm (length) \times 2 mm (thickness) and is placed in the 2 mm space between every two detectors in the vertical direction. PCBs described in section 2.6.1 are also considered. The geometry of the simulation is shown in Figure 2.29. A total of 8×10^9 source events is simulated.

Spectra of the photons incident on the silicon channels are shown in Figure 2.30 and the spectrum of deposited energy is shown Figure 2.31. The scatter-to-primary

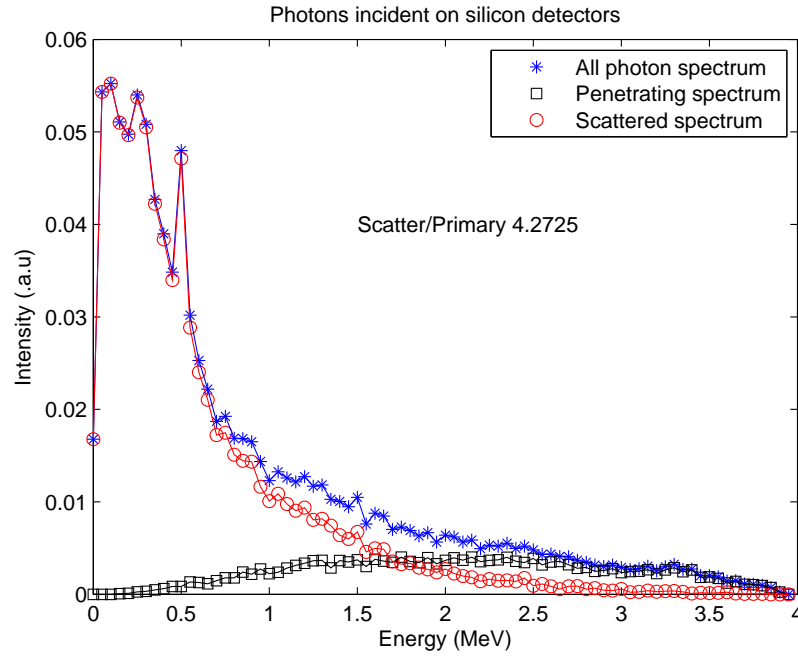


FIGURE 2.30: Spectra of photons incident on the 1000 silicon channels. Tungsten collimator is placed in front of the detector stack.

ratio is even lower (4.27) than the case without PCBs (12.55). On the other hand, the low-energy deposition events because of scattering in the stacked detectors and PCBs restore (see Figure 2.31).

Image of the phantom concrete is shown in Figure 2.32, and the horizontal profiles without threshold and with a 200-keV threshold are shown in Figure 2.33. The contrast is much better especially when a 200 keV-threshold is set to all detectors.

Considering structural components of the detector module, the scattering is greatly enhanced (by about 70% with 1.5 mm thick PCBs) and it will lead to a degradation of spatial resolution. The scattering can be decreased by reducing structural components. However, this is limited in order not to degrade strength of the detector module. Because the X ray has high penetration capability, tungsten sheets inside the detector module even enhances scattering and degrades contrast of image. On the contrary, collimator composed of horizontal tungsten sheets effectively reduces the scattering inside the detectors because primary photons that penetrate the object and direct at PCBs are stopped by tungsten sheets in front of the detectors. In addition, an energy threshold can also be used to decrease the contribution of scattering inside the detector module since the scattered photons tend to deposit lower energy inside detectors.

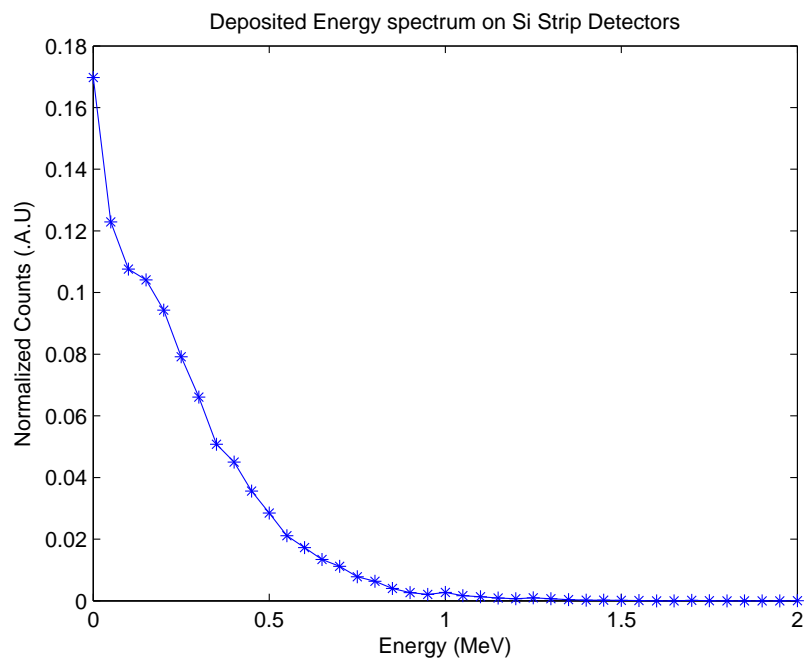


FIGURE 2.31: Spectrum of deposited energy on 1000 channels. Tungsten collimator is placed in front of the detector stack.

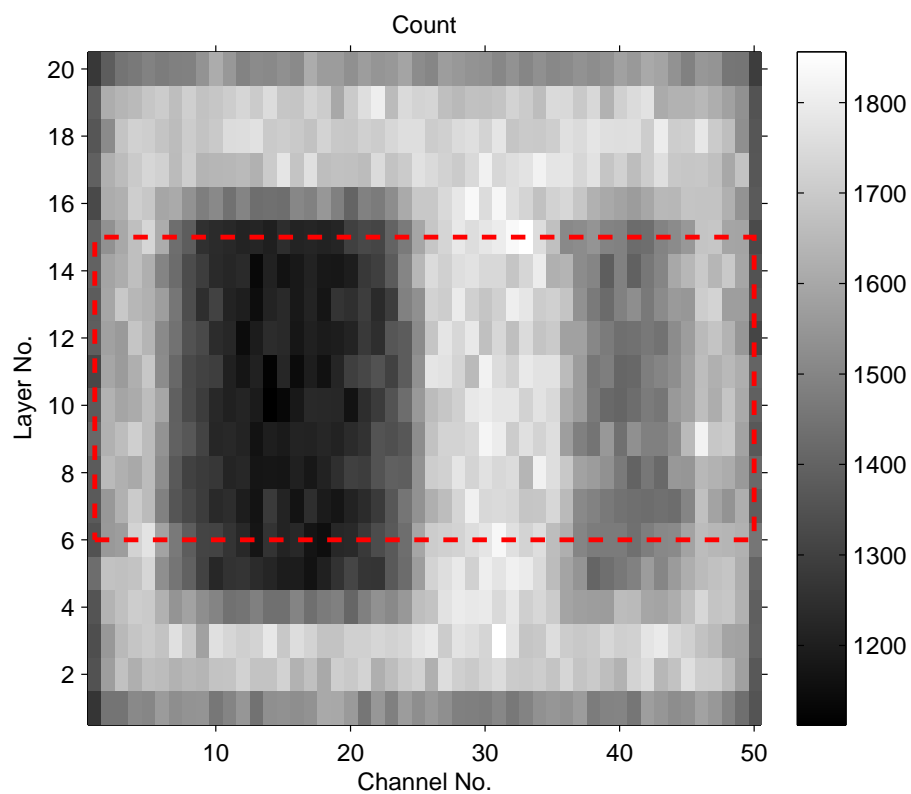


FIGURE 2.32: Image of the phantom concrete. Tungsten collimator is placed in front of the detector stack.

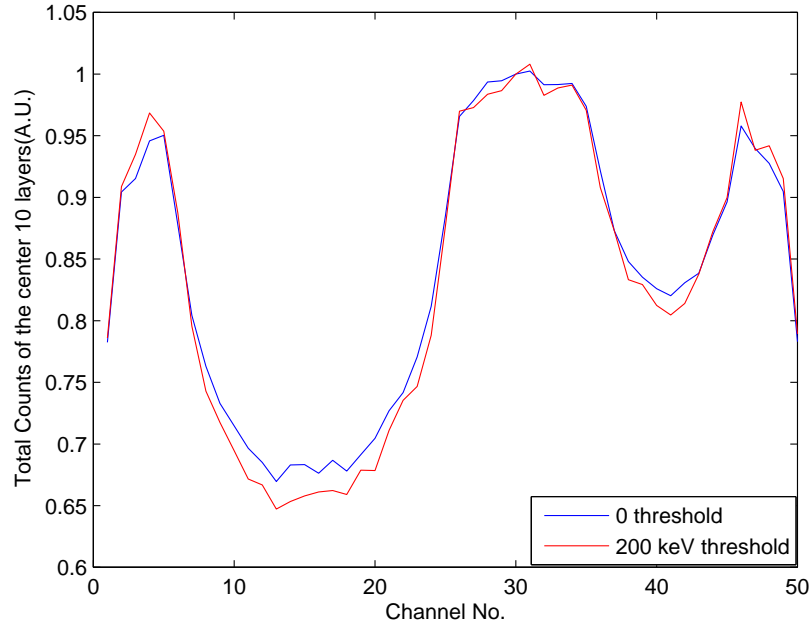


FIGURE 2.33: Horizontal profiles of the red rectangular area without/with threshold. Tungsten collimator is placed in front of the detector stack.

2.7 Summary

According to the simulation results, we get the following observations about the high-energy X-ray imaging system:

- 1) Photon spectrum is greatly hardened after penetrating a thick sample. The average energy of the photons from the 3.95 MeV X-ray source increases from 0.82 MeV to 2.87 MeV after penetrating a 100 cm thick concrete. Detectors with high efficiency for high-energy photons are extremely demanded for nondestructive testing of thick samples with high-energy X-ray sources.
- 2) Scattering contribution is greatly enhanced after penetrating a thick sample. The scatter-to-primary ratio is 69% after penetrating a 100-cm-thick concrete. Detectors should be placed further in order to decrease the scattering contribution from the test object. For a 40-cm-thick concrete, scatter-to-primary ratio decreases from 56% to 11% when the distance increases from 10 cm to 40 cm.
- 2) Scattering contribution of photons incident on silicon detectors inside the 5 cm long detector module is greatly severe. The scatter-to-primary ratio is about 6.3.
- 3) Structural materials enhance scattering inside the detector module. The scatter-to-primary ratio even increases to be about 10.7 when an 1.5-mm-thick PCB under each strip detector is considered. Structural materials should be thinner to reduce scattering.
- 4) Tungsten sheets parallel and match detectors can improve image contrast, it should be

placed close to object and apart from the detectors. Tungsten sheets inside the detector module even enhances scattering other than reducing scattering, and the scatter-to-primary ratio increases to be about 12.5 when a 0.5-mm-thick tungsten sheet is placed under each strip detector. On the contrary, the scatter-to-primary ratio decreases to be about 4.3 when a collimator module composed of 2-cm-thick tungsten sheets is placed in front of the detector module.

5) Energy threshold can be used to improve image contrast, and this can only be feasible in photon-counting imaging systems.

Chapter 3

a-Si/c-Si heterojunction strip detector

Semiconductor detectors have been widely used as the basic detection media since 1960s, and modern detectors are referred to as semiconductor diode detectors or simply solid-state detectors. Advantages of semiconductor detectors are superior energy resolution, compact size, relatively fast time characteristics, et al. Silicon predominates in the available semiconductor materials benefitting from its mature fabrication technology and low cost, room temperature operation, high values of carriers' mobility and lifetime, et al. Silicon strip detectors (SSDs) were firstly introduced as high precision tracking devices for high energy physics experiments in the early 1980s [40]. Since then, SSDs have been used in astrophysics satellites and telescopes, Compton cameras as scatter and X-ray/gamma-ray radiography.

3.1 Interaction of photons

A large number of possible interaction mechanisms are known for photons in matter, however, only three major processes play important roles: photoelectric absorption, Compton scattering, and pair production. They lead to changes in the photon history, in that the photon either disappears entirely or is scattered.

3.1.1 Photoelectric effect

In the photoelectric process (shown in Figure 3.1), the primary photon with an energy of $h\nu$ is completely absorbed and an energetic photo-electron is released from

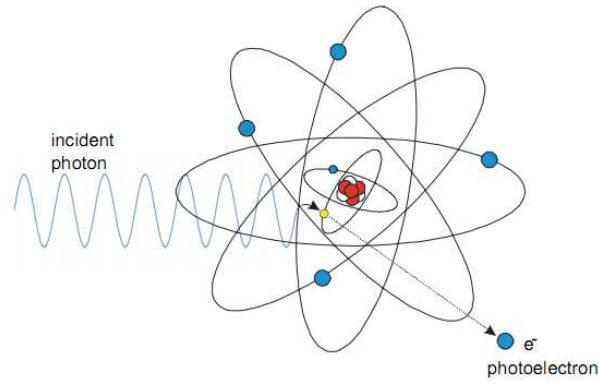


FIGURE 3.1: Demonstration of the photoelectric effect.

one of its bound shells. The photoelectric process is the predominant interaction for photons of relatively low energy and high atomic number (Z) materials. The probability of photoelectric absorption per atom over all ranges of $h\nu$ and Z , symbolized τ , can be expressed as:

$$\tau = \text{constant} \times \frac{Z^n}{h\nu^{3.5}} \quad (3.1)$$

where the exponent n varies between 4 and 5 over the photon energy region of interest.

3.1.2 Compton scattering

The Compton scattering (shown in Figure 3.2) takes place between the incident photon and a free or orbital electron. The incident photon is scattered by an angle with respect to its original direction and transfers a part of its energy to the recoil electron. The Compton scattering probability (σ) per atom depends on the number of electrons available and therefore increases linearly with Z but decreases as the photon energy increases. The Compton scattering is most often the predominant interaction mechanism for photon energies of typical radioisotope source. All angles of scattering are possible, and the angular distribution of scattered photon is predicted by the Klein-Nishina formula for the differential scattering cross section

$$\frac{d\sigma}{d\Omega} = Zr_0^2 \left(\frac{1}{1 + \alpha(1 - \cos\theta)} \right)^2 \left(\frac{1 + \cos^2\theta}{2} \right) \left(1 + \frac{\alpha^2(1 - \cos\theta)^2}{(1 + \cos^2\theta)[1 + \alpha(1 - \cos\theta)]} \right) \quad (3.2)$$

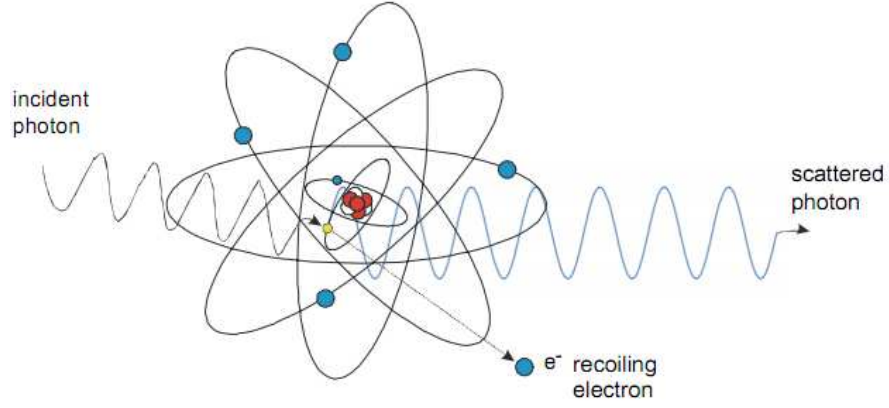


FIGURE 3.2: Demonstration of the Compton scattering.

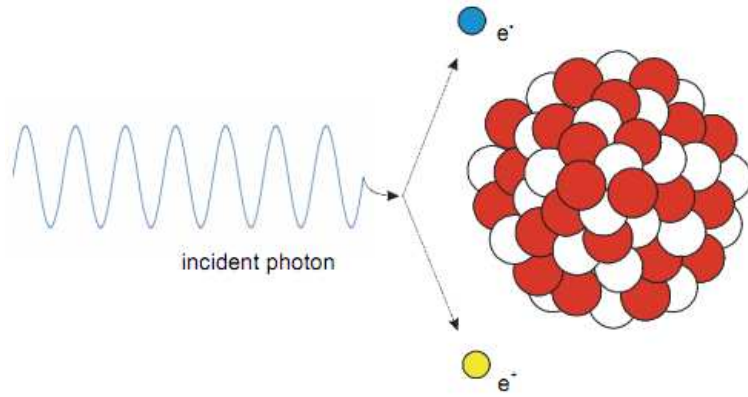


FIGURE 3.3: Demonstration of the pair production.

where $\alpha = h\nu/m_0c^2$ and r_0 is the classical electron radius and m_0c^2 is the rest-mass energy of the electron (0.511 MeV).

3.1.3 Pair production

If the photon energy exceeds twice the rest-mass energy of an electron (1.02 MeV), pair production process (shown in Figure 3.3) is energetically possible at the vicinity of an atom. The probability of pair production (κ) increases with increasing photon energy and atomic number approximately as Z^2 . The pair production is predominantly confined to high-energy photons with high-Z materials.

The relative importance of the three major interactions between photon and matter is shown in Figure 3.4.

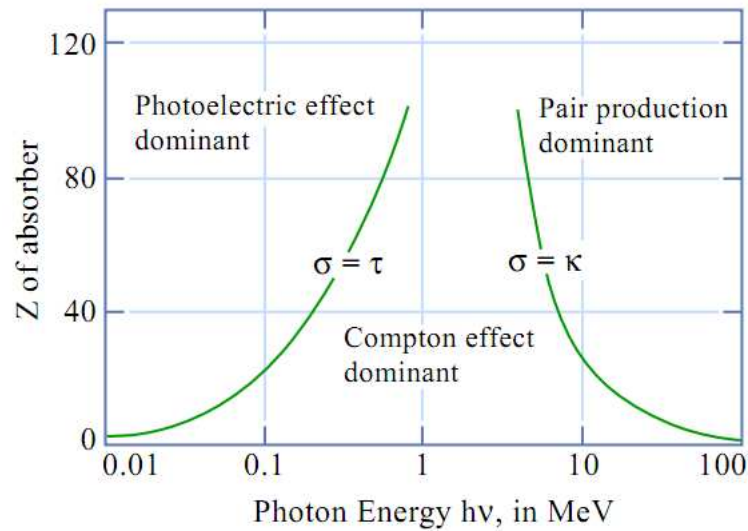


FIGURE 3.4: The relative importance of the three major interactions.

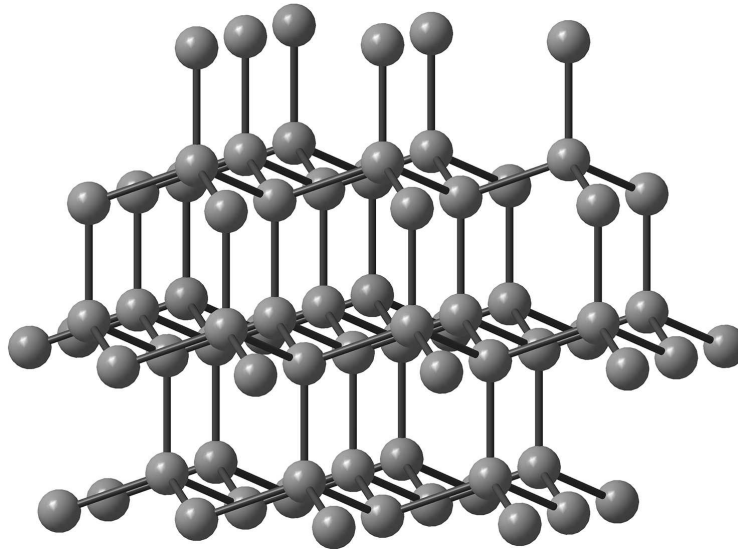


FIGURE 3.5: Diamond-lattice type structure of silicon.

3.2 Detector basics

3.2.1 Intrinsic properties of silicon

Silicon is the 14th element in the periodic table and belongs to group IV. It has a diamond-lattice type structure (Figure 3.5). Important properties of silicon and other commonly used semiconductors (diamond and germanium) are listed in Table 3.1 [19, 41–43].

TABLE 3.1: Intrinsic properties of commonly used semiconductors.

Semiconductor	Si	Ge	Diamond	GaAs	CdTe
Atomic number	14	32	6	31/33	48/52
Density [g/cm^3]	2.33	5.32	3.52	5.31	6.2
Band gap [eV]	1.12	0.66	5.47	1.42	1.56
Average energy/eh pair	3.61	2.96	13	4.26	4.43
Dielectric constant	11.9	16.0	5.7	13.1	10.2
Electron mobility [$cm^2/V\cdot s$]	1500	3900	1800	8500	1050
Electron mobility lifetime [cm^2/V]	>1	>1	-	10^{-5}	$10^{-4} - 2 \times 10^{-3}$
Hole mobility [$cm^2/V\cdot s$]	450	1900	1200	400	100
Hole mobility lifetime [cm^2/V]	~ 1	>1	-	10^{-6}	$10^{-5} - 10^{-4}$

The valence band is the highest range of electron energies which is fully occupied with electrons at absolute zero temperature. The higher band in which electrons can move freely between atoms of the crystal is called the conduction band. Electrons in the conduction band contribute to the electrical conductivity of materials. The forbidden area between the two bands is called band gap, and the size of it determines whether the material is classified as a semiconductor or an insulator. Silicon has a band gap of 1.12 eV as shown in Table 3.1.

Intrinsic semiconductors contain no impurities. The occupation probability for an electronic state is given by the Fermi-Dirac function:

$$F(E) = \frac{1}{1 + \exp(\frac{E-E_F}{kT})} \quad (3.3)$$

Where E_F , the Fermi energy, is the energy at which the occupation probability of a possible state is 50%, k is the Boltzmann constant and T is the absolute temperature. This expression can be approximately separate for electrons ($F_n(E)$) and holes ($F_p(E)$) for intrinsic semiconductors as:

$$F_n(E) \approx e^{\frac{E-E_F}{kT}} \quad (3.4)$$

$$F_p(E) = 1 - F(E) \approx e^{\frac{E_F-E}{kT}} \quad (3.5)$$

The state density in the conduction and valence bands is given by:

$$N(E_{kin}) = 4\pi(\frac{2m_{eff}}{h^2})^{3/2} E_{kin}^{1/2} \quad (3.6)$$

Where m_{eff} is the effective mass of electrons (m_n) or holes (m_p) respectively, h is Planck's constant, and E_{kin} is the kinetic energy measured from the band gap.

The free electron density n is obtained by integrating the product of state density and the occupation probability over the conduction band:

$$n = 2 \left(\frac{2\pi m_n kT}{h^2} \right)^{3/2} e^{-\frac{E_C - E_F}{kT}} = N_C e^{-\frac{E_C - E_F}{kT}} \quad (3.7)$$

Similarly for holes, we get:

$$p = 2 \left(\frac{2\pi m_p kT}{h^2} \right)^{3/2} e^{-\frac{E_F - E_V}{kT}} = N_V e^{-\frac{E_F - E_V}{kT}} \quad (3.8)$$

The product of electron and hole density is independent of the Fermi level and depends on the band gap. For an intrinsic semiconductor at thermal equilibrium, the numbers of electrons and holes are equal: $n=p=n_i$ ($\approx 1.45 \times 10^{10} \text{ cm}^{-3}$ for silicon at 300 K). It is found that:

$$n_i = \sqrt{N_C N_V} e^{\frac{E_C - E_V}{2kT}} = \sqrt{N_C N_V} e^{\frac{E_G}{2kT}} \quad (3.9)$$

and

$$E_i = \frac{E_C + E_V}{2} + \frac{3kT}{4} \ln\left(\frac{m_p}{m_n}\right) \quad (3.10)$$

Equation 3.7 and equation 3.8 can be rewritten as:

$$\begin{aligned} n &= n_i e^{\frac{E_F - E_i}{kT}} \\ p &= n_i e^{\frac{E_i - E_F}{kT}} \end{aligned} \quad (3.11)$$

3.2.2 Extrinsic properties of silicon

Suffered from the technical difficulty of obtaining sufficient high purity semiconductor materials, intrinsic semiconductors are seldom used. On the contrary, extrinsic semiconductors with intentional additive of small fractions of impurities are widely used in semiconductor devices. The procedure of specific impurities is called doping and the added impurity is called dopant.

Group V elements, such as phosphorus (P) and arsenic (As) which have five valence electrons, can donate an additional electron in the crystal lattice and are called donors. On the other hand, elements in the group III, such as boron which only has three valence electrons, can accept an additional electron at their place in the crystal lattice and are called acceptors.

Figure 3.6(a) represents silicon doped with arsenic. Only four valence electrons are used to form covalent bonds with neighboring silicon atoms, while the fifth valence

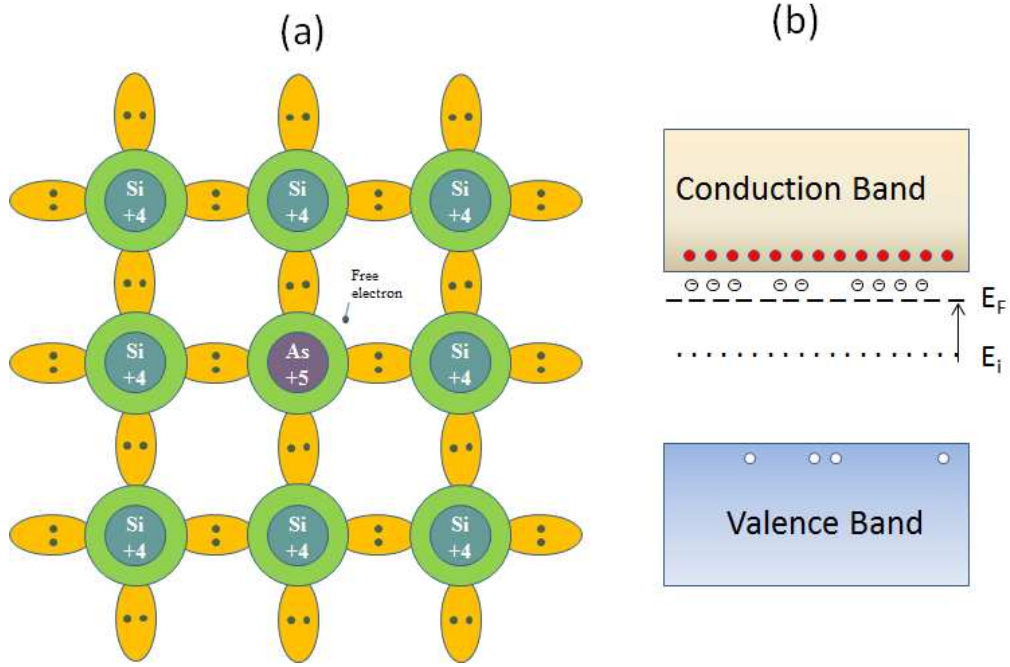


FIGURE 3.6: n-type doping. (a) The crystal lattice of Si doped with As. (b) Band structure of n-type material.

electron is weakly bonded and is free for conduction. The $E_C - E_D$ is 0.045 eV for P and is 0.054 eV for As in silicon. Electrons in these states are almost completely ionized at room temperature and transported to the conduction band (Figure 3.6(b)). Silicon doped with negative charge carriers is called n-type silicon. The donor levels are almost completely ionized can be explained by the movement of the Fermi level E_F from the intrinsic level E_i towards the conduction band. The acceptor levels are almost completely filled can be explained by the movement of E_F from E_i towards the valence band. Considering high concentration doping which is generally real in practice, the electron density equates to the number of donor and hole density equates to the number of acceptor.

For n-type silicon, the new Fermi level is derived from Equation 3.7:

$$E_C - E_F = kT \ln \frac{N_C}{N_D} \quad (3.12)$$

If a silicon atom is replaced by boron, one electron is missing in the covalent bonds and a hole is created and free for conduction (Figure 3.7(a)). These holes introduce energy states (E_A) slightly above the valence band (E_V , and $E_A - E_V = 0.045$ eV). These states are almost completely filled at room temperature and holes are transported in the valence band (Figure 3.7(b)). Silicon doped with positive charge carriers is called

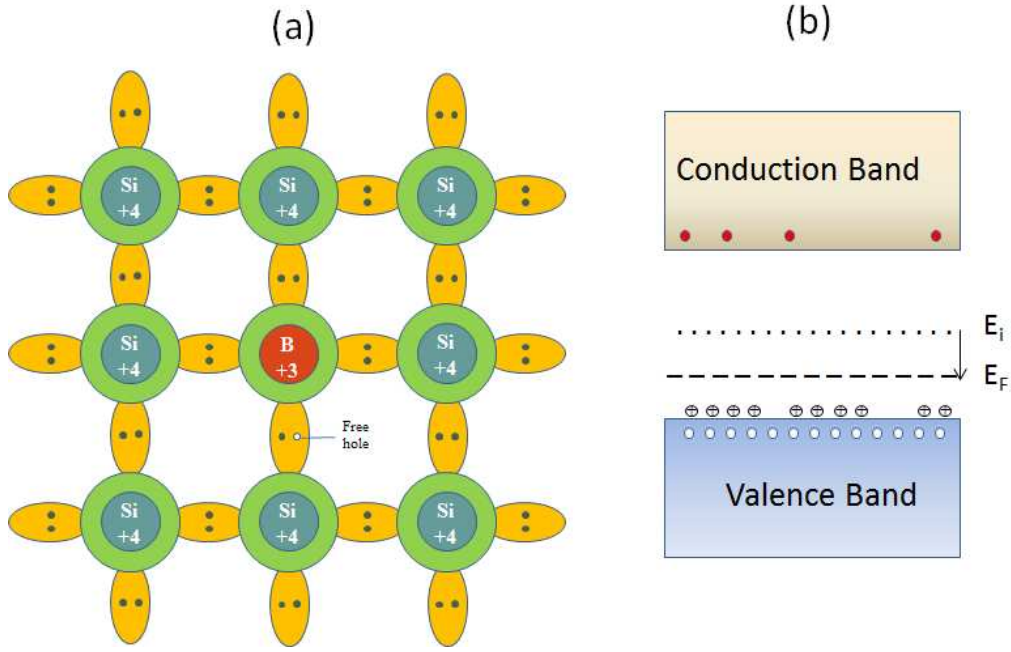


FIGURE 3.7: p-type doping. (a) The crystal lattice of Si doped with B. (b) Band structure of p-type material.

p-type silicon. For p-type silicon, the new Fermi level is derived from Equation 3.8:

$$E_F - E_V = kT \ln \frac{N_V}{N_A} \quad (3.13)$$

The electron density and hole density can still be described by Equation 3.11 with rewritten Fermi levels. The increase of majority carriers is accompanied with a decrease of minority carriers.

3.2.3 p-n junction

The p-n junction, as the most important electronic structure, can be formed by joining a p-type semiconductor and an n-type semiconductor. Such a structure shows diode characteristics, which is low resistive if positively biased and high resistive if reversely biased. The p-n junctions can be categorized into homojunctions and heterojunctions. A homojunction is formed between layers of similar semiconductor materials, which have equal band gaps but are differently doped. A heterojunction is a semiconductor interface that occurs between two dissimilar semiconductors, which have unequal band gaps as opposed to a homojunction. The p-n junction will be introduced based on the silicon homojunction.

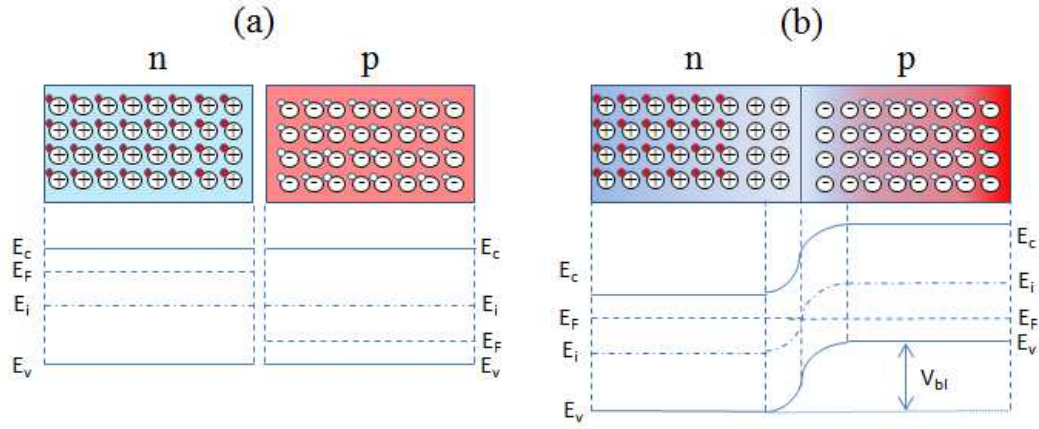


FIGURE 3.8: A p-n junction in thermal equilibrium (a) with two parts separated (b) with two parts brought together.

The p-type part and n-type part are electrically neutral with electrons and holes homogeneously distributed (Figure 3.8(a)) when they are initially separated. Once the two parts are contacted, free electrons with higher density in the n-type part will diffuse into the p-type region and holes with higher density in the p-type region will diffuse into the n-type region, and a space charge region near the junction is created and an electric field is formed to counteract the diffusion (Figure 3.8(b)). This region is depleted of free charge carriers because the electric field sweeps away any mobile charge carriers in the region. The transformation can also be considered in the band model. A built-in voltage (V_{bi}) is formed because the Fermi levels have to be equal in thermal equilibrium.

If an external voltage (V) is applied to the p-n junction, the charge carriers will start to drift according to the electric field. The width of the space charge region (d) shrinks with forward bias and expands with reverse bias:

$$d = \sqrt{\frac{2\epsilon\epsilon_0(N_A + N_D)}{q_e N_A N_D} (V_{bi} - V)} \quad (3.14)$$

where ϵ is the dielectric constant and ϵ_0 is permittivity of the semiconductor. For silicon, ϵ is 11.9.

In the case of semiconductor radiation detector, the p-n junction is usually formed on low doped silicon of which one edge side is highly oppositely doped (with a density of N_d) and the junction is reversely biased (with $|V| \gg V_{bi}$). The width of the space charge region (d) can be expressed as:

$$d = \sqrt{\frac{2\epsilon\epsilon_0}{q_e N_d} |V|} \quad (3.15)$$

The depleted space charge region is treated as the sensitive region for ionization irradiations. Electron-hole pairs are created if radiations incident in the depleted region, and they will be separated by the electric field and drift to the electrodes on the edges. The drift of charge carriers leads to a current pulse and will be processed with front-end and back-end electronics.

3.3 Fabrication processes of silicon strip detector

The passivated planar technology is the most mature process for fabricating silicon junction detectors with excellent operational characteristics. However, it suffers from complexity. Hydrogenated amorphous silicon is resistive to radiation and suitable for large area fabrication. However, it is difficult to produce a-Si layer thick enough for minimum-ionizing particle detection. Instead, some research about the fabrication of a-Si/c-Si heterojunction detector was reported. Compared with the normal planar process, the hydrogenated amorphous silicon/crystalline silicon (a-si:H/c-si) heterojunction greatly simplifies the fabrication of semiconductor detectors. However, a heterojunction detector with both low leakage current and position-sensitive capability was not realized. Yabe M et al. [44] fabricated a large-area a-Si/c-Si heterojunction detector by DC plasma deposition process at 200 °C, and the detector showed a leakage current of 150 nA at full depletion bias and an energy resolution of 8.3 keV full width at half maximum (FWHM) for 59.5 keV at room temperature. Chiba Y et al. [45] fabricated a heterojunction detector by the plasma-chemical vapor deposition (CVD) method, and they realized position-sensitive by evaporating segmented electrodes on the a-Si film, however, their detector suffered from high leakage current ranged from 10^{-6} to 10^{-5} A at 20 °C and they did not find out the solution to decrease this high leakage current. We try to fabricate strip detector with the a-si/c-si heterojunction technology.

3.3.1 General process steps in passivated planar technology

The passivated planar technology follows mature production technologies used to produce integrated circuits in the semiconductor industry [46, 47]. The most important differences are more severe requirements for low contamination with impurities and low defects during production. Contamination of the sensor bulk will increase leakage current and the defects over a large area strip detector affect charge collection, leading to degradation of the detector performance. In order not to deteriorate the detector performance, special care has to be taken in the passivated technology and the fabrication procedures become more complex.

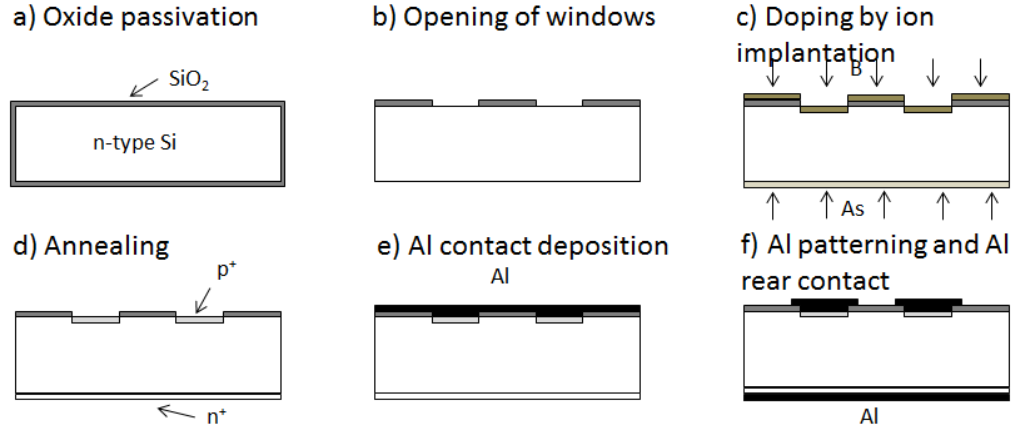


FIGURE 3.9: Steps of the passivated planar process.

The planar fabrication process generally begins with high-purity silicon wafer of either p-type or n-type. Take n-type silicon wafer as an example, the steps in the process are briefly shown in Figure 3.9:

- a) Firstly passivate the surface through oxidation at elevated temperature after the wafer is polished and cleaned.
- b) Deposit photoresist, expose photoresist through mask with strip pattern, etch exposed SiO_2 areas so as to open windows for p^+ doping and remove the remaining photoresist. These processes can be summarized as the photolithography technique.
- c) Introduce p-dopant to form strip electrodes through the implanting of acceptor ions (typically boron) and introduce n-dopant on the rear surface through donor implantation (typically with arsenic) using accelerators.
- d) Drive-in and thermal anneal of implant to remove radiation damage in the implanted layers at elevated temperature.
- e) Deposit aluminum-silicon alloy for contacts on the front surface.
- f) Form strip and bonding pads in the front surface by photolithography and deposit aluminum contact to form ohmic contact on backside.

3.3.2 a-si/c-si heterojunction process

The wafers employed for fabrication are p-type silicon, each with an area of $52.5 \text{ mm} \times 52.5 \text{ mm}$ and a thickness of $500 \mu\text{m}$. The resistivity of the wafers is $10 \text{ k}\Omega\cdot\text{cm}$ and the surface orientation is (111).

The fabrication process is shown in Figure 3.10:

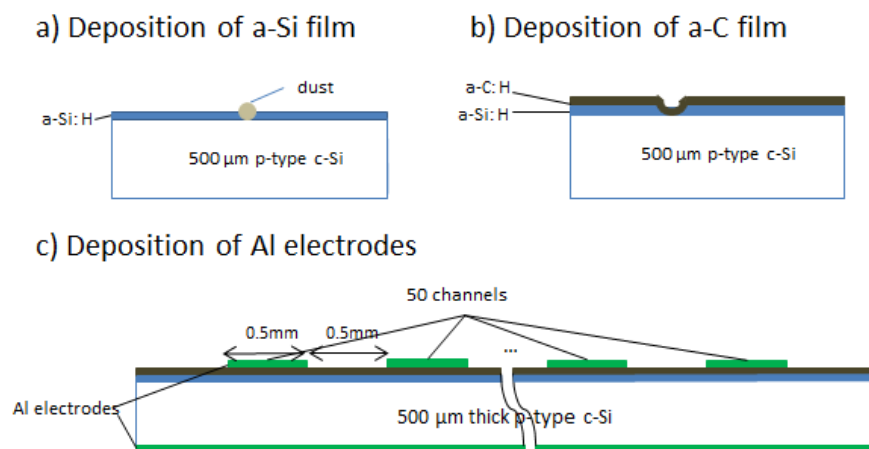


FIGURE 3.10: Steps of fabricating a-Si/c-Si heterojunction strip detector.

a) Firstly an 1 μm thick undoped a-Si: H film is deposited on the wafer at 100 $^{\circ}\text{C}$ by decomposing SiH_4 diluted to 10% in hydrogen using plasma enhanced chemical vapor deposition (PECVD) technique.

However, fatal pinhole defects will be caused in the a-Si film if there is dust attached to the silicon wafer during the depositing. These tiny pinholes will lead to a direct contact of the metal layer and the Si wafer, which is the main reason for the large leakage current if a metal contact is evaporated on the a-Si film.

b) To solve this problem, another Hydrogenated amorphous carbon (a-C: H) layer is deposited on the a-Si layer at 100 $^{\circ}\text{C}$ by decomposing CH_4 using electron cyclotron resonance chemical vapor deposition (ECR-CVD) techniques.

The resistive a-C: H layer has a thickness of 1~3 nm and resistivity of $1\sim 8\times 10^{12} \Omega\cdot\text{cm}$, which can effectively suppress the leakage current without a high additional voltage drop when the detector is reversely biased.

c) Then 50 electrodes are formed on the a-C: H layer by masked deposition of aluminum using the electron beam evaporation technique. An aluminum anode is also evaporated on the other side of the silicon wafer.

Each electrode on the a-C: H layer is 0.5 mm \times 49.5 mm, and the electrodes are 0.5 mm apart. The thickness of the aluminum cathodes and anode is 1 μm .

A fabricated a-Si/c-Si heterojunction strip detector is shown in Figure 3.11. The 50 front Al electrodes can be wire bonded to multichannel readout electronics (e.g. ASIC).

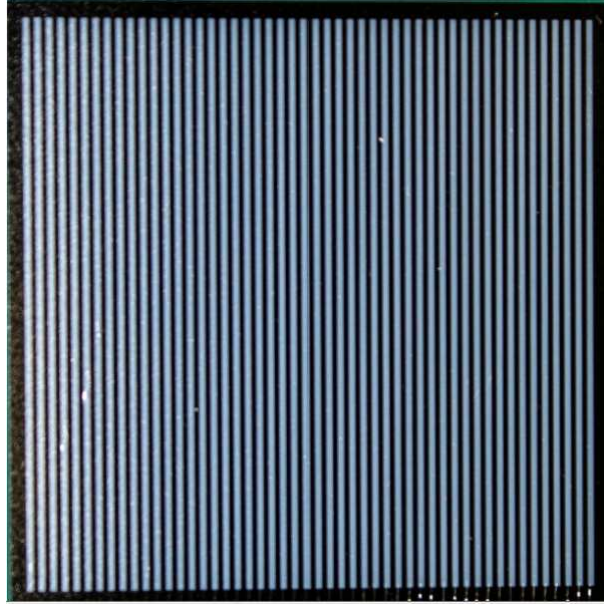


FIGURE 3.11: A fabricated a-Si/c-Si heterojunction strip detector.

3.4 Operational characteristics

Measurement of the leakage current and capacitance of each channel of the silicon strip detector helps to characterize the detector and aids in the optimization of detector fabrication. We measured the bias dependence of leakage current and junction capacitance with the Keithley 4200-SCS semiconductor characterization system, and the detector was placed in the Apollowave MBP-55 probe station for optical and electromagnetic shielding.

3.4.1 Leakage current characteristics

The leakage current through each single channel was measured as a function of reverse bias voltage at 20 °C. Figure 3.12 shows the test configuration. Three channels were biased at the same voltage, and all other channels were float while the anode was grounded. The bias was increased from 0.1 V to 150 V with a 1 s delay between two bias voltages in order to allow the current to reach equilibrium. Leakage currents of 3 adjacent channels in one measurement are shown in Figure 3.13.

The leakage currents of the two adjacent channels were higher (about 2 times) than the central channel, indicating the neighboring channels were partially depleted even when they were floating. As a result, only the leakage current of the central channel in each measurement was recorded as the real leakage current. The bias dependence of the leakage currents of 5 typical channels is shown in Figure 3.14(a), and the leakage

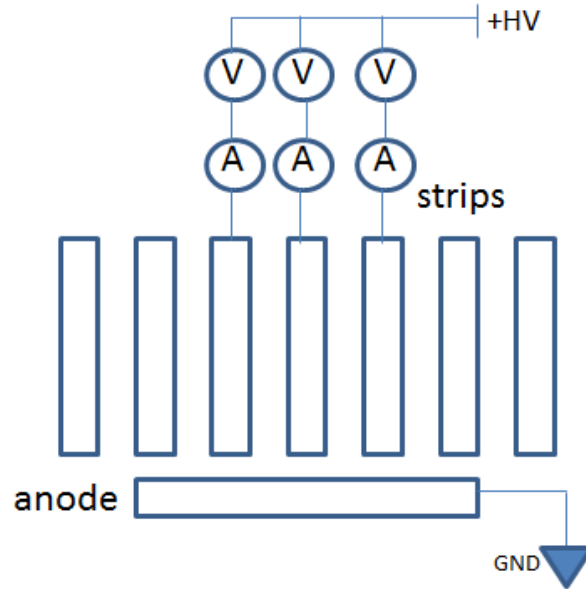


FIGURE 3.12: Configuration of the leakage current measurement. 3 channels are biased at the same high voltage simultaneously.

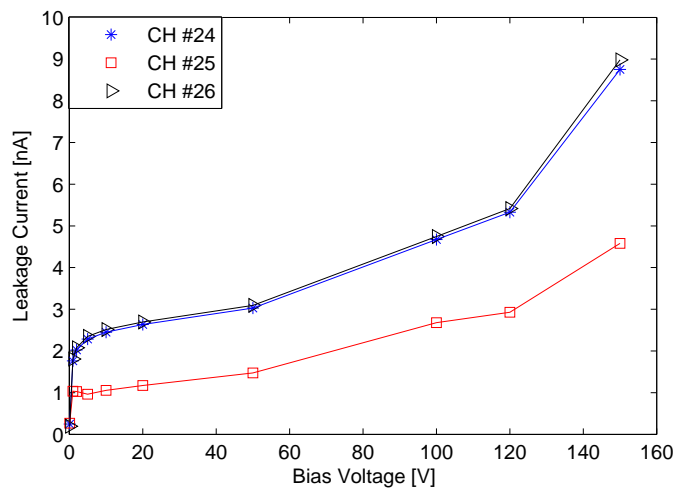


FIGURE 3.13: Leakage currents of 3 adjacent channels in one measurement.

currents of all 50 channels at typical biases are shown in Figure 3.14(b). The 50-channel detector had quite homogenous leakage performance when the bias was lower than 120 V except for the 2 edge channels that covered wider side areas (shown in Figure 3.14(b)). The average leakage current of the central 48 channels was 2.9 nA and the leakage current density was calculated to be 0.06 nA/mm^2 at 120 V bias. However, one channel showed higher leakage current when the bias is 150 V.

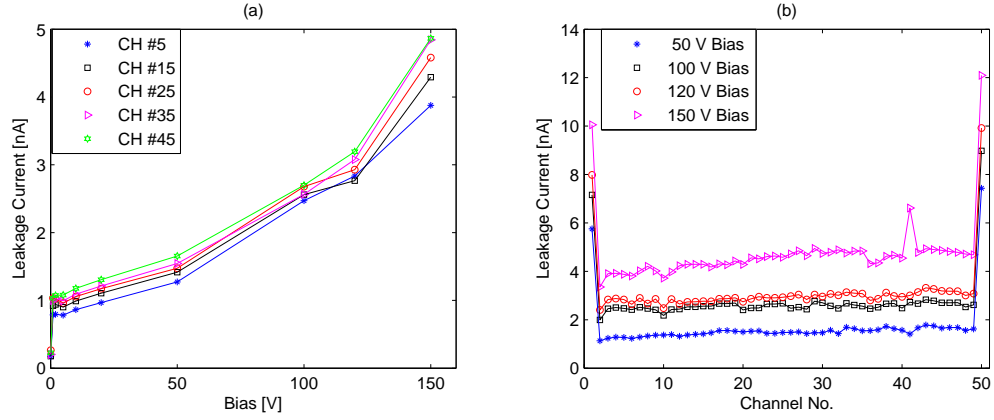


FIGURE 3.14: (a) Bias dependence of the leakage currents of 5 channels (b) Leakage currents of all 50 channels.

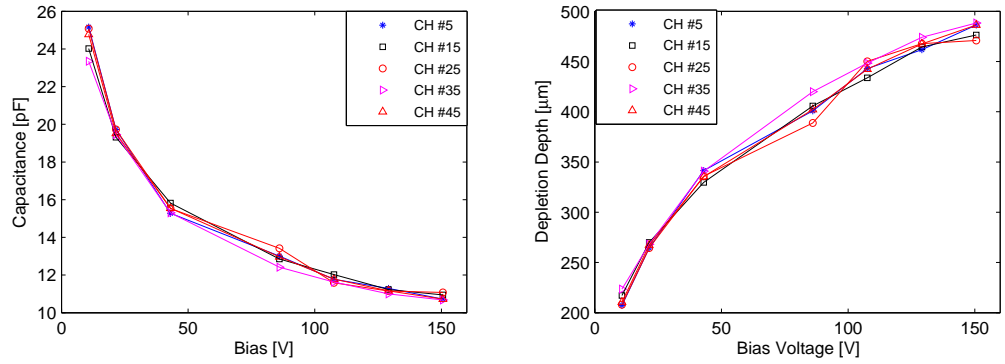


FIGURE 3.15: (a) Junction capacitances of 5 channels. (b) Depletion depth of 5 channels.

3.4.2 Capacitance characteristics

We measured the junction capacitances using similar configuration as shown in Figure 3.12. The junction capacitances of 5 channels at different bias voltages are shown in Figure(a). The depletion depth can be estimated accordingly (see Figure 3.15). A bias of 120 V guaranteed depletion of over 90% of the whole wafer and homogeneous leakage performance of all central 48 channels. 120 V was chosen the working bias of the detector.

3.5 Energy spectrum measurement

A CLEARPULSE 5005H charge-sensitive preamplifier and an ORTEC 571 shaper were used to evaluate the noise of the detector. The performance of the preamplifier is 1.25 keV (FWHM) + 20 eV/pF (FWHM) for silicon at a 2.0 μ s shaping time. The

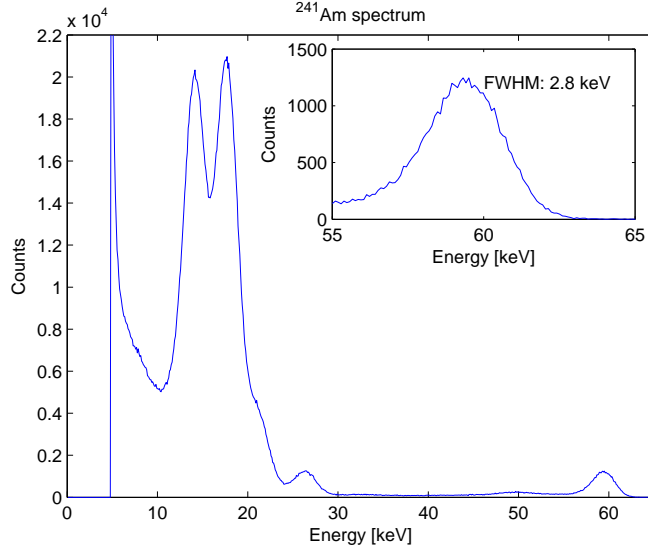


FIGURE 3.16: ^{241}Am spectrum measured by channel 2. The FWHM of the 59.5 keV photopeak is 2.8 keV.

shaping time was set to $1.0\ \mu\text{s}$, the bias was set to 120 V, and the temperature was kept at 18°C during the measurement.

3.5.1 ^{241}Am spectrum and ^{57}Co spectrum

Pulse height spectra of ^{241}Am and ^{57}Co measured by the second channel of the detector are shown in Figure 3.16 and Figure 3.17, respectively. The FWHM of the 59.5 keV photopeak is 2.8 keV and the FWHM of the 122 keV photopeak is 2.9 keV.

3.5.2 ^{133}Ba spectrum and ^{137}Cs spectrum

Pulse height spectra of ^{133}Ba and ^{137}Cs measured by the second channel are shown in Figure 3.18(a) and Figure 3.18(b), respectively. Because the atomic number of silicon is too low, the 356 keV photopeak of ^{133}Ba and the 662 keV photopeak of ^{137}Cs cannot be observed in the measured spectra. However, identification of full energy peaks is not required since X-ray sources usually emit photons with continuous energy spectra.

3.6 Position sensitivity evaluation

As a new detector developed for imaging systems, the position sensitivity of the strip detector is required to be confirmed firstly. One 48-channel ToT ASIC was connected

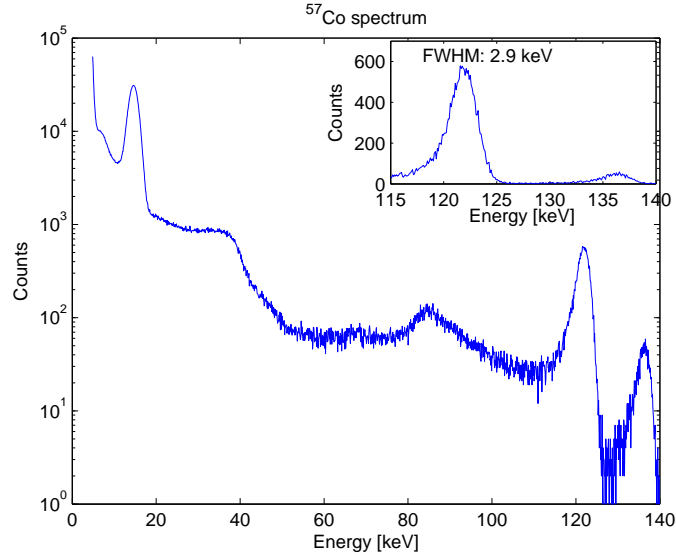


FIGURE 3.17: ^{57}Co spectrum measured by channel 2. The FWHM of the 122 keV photopeak is 2.9 keV.

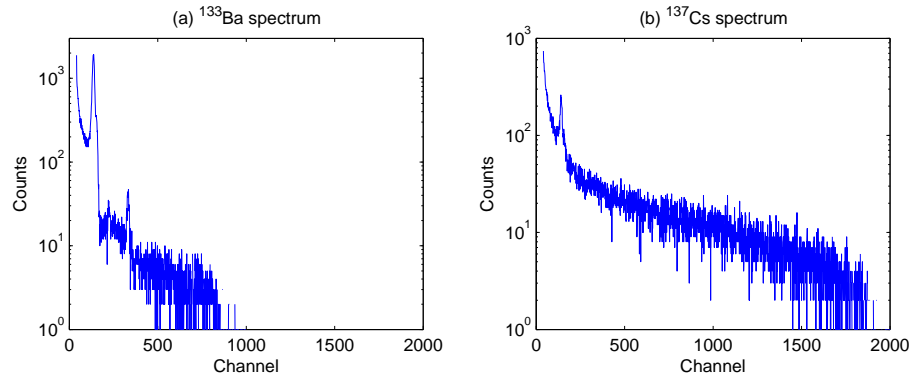


FIGURE 3.18: (a) The measured ^{133}Ba spectrum. (b) The measured ^{137}Cs spectrum.

with the central 48 channels of the detector to readout and process signals for sensitivity evaluation. Event number of photons that deposited energy higher than a fixed energy threshold in each channel was recorded. The ASIC will be introduced in Section 4.3.

We performed position sensitivity evaluation simply with a collimated ^{90}Sr β source. The setup for the evaluation is shown in Figure 3.19. The ^{90}Sr source was placed above a lead collimator and the collimator was placed above the detector surface. The lead collimator has a thickness of 6 mm and is enough to stop the electrons emitted by the ^{90}Sr source. The diameter of the collimator hole is about 1.0 mm.

Five measurements of count distribution were performed by varying the position of the collimator together with the ^{90}Sr source. The count distributions were Gaussian

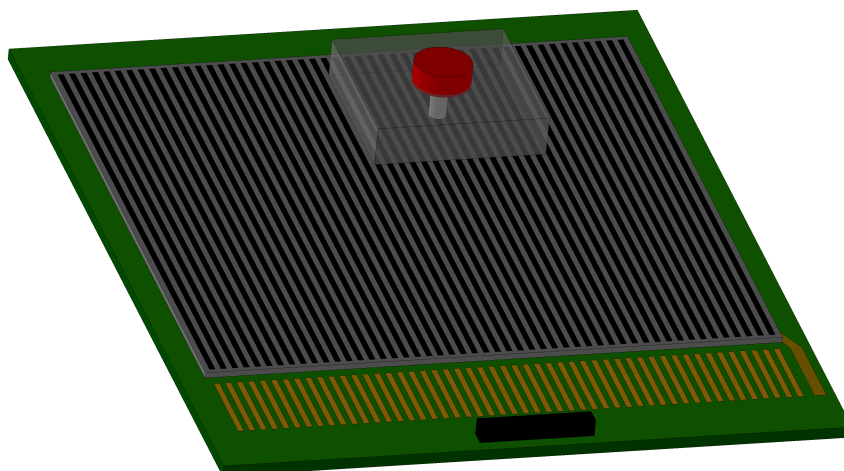
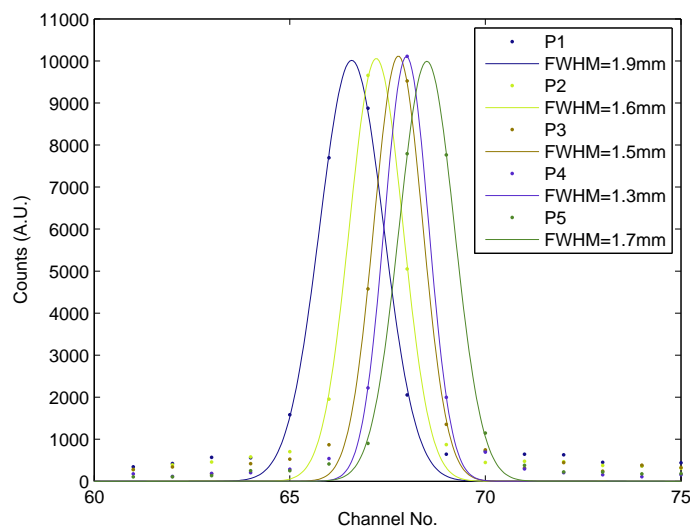


FIGURE 3.19: Setup of the position-sensitivity evaluation.

FIGURE 3.20: Count distributions of 5 measurements with a collimated ^{90}Sr β source

fitted and the FWHMs of fitting were obtained (Figure 3.20). FWHMs of the 5 measurements were between 1 mm and 2 mm which was a little larger than the pitch of the detector. We can expect the measured FWHM would be closer to 1 mm if we use a collimator with a larger collimation ratio.

3.7 Conclusion

Compared with the normal passivated process for fabricating silicon detectors, the *a-Si/c-Si* heterojunction process is much more simplified. The *a-Si/c-Si* heterojunction

process is suitable for mass production at low cost, especially suitable for imaging systems that are composed of a large number of detectors.

We fabricated 50-channel 1D strip detectors with the a-Si/c-Si heterojunction technique. The strip detector has homogenous and low leakage current characteristics at the full-depletion bias. The fabricated detector has energy resolutions of 2.8 keV FWHM at 59.5 keV and 2.9 keV FWHM at 122 keV. The fabricated 1 mm pitch detector has a spatial resolution of 1-2 mm (FWHM).

Face-on strip detectors can be stacked orthogonally as tracker for Compact Muon Solenoid (CMS,[48]) and Fermi Large Area Telescope [49]. The edge-on 1D strip detectors can be stacked to build 2D detectors for gamma-ray or X-ray imaging. Furthermore, cathode pattern can be easily fabricated on the heterojunction by common lithography process to meet the demands of different applications, e. g., 2D pads for low energy X-ray imaging or Compton imaging (as scatter).

Chapter 4

Time-over-Threshold (ToT) based front-end electronics

Conventional discrete circuits are not applicable to modern high-spatial-resolution photon-counting imaging systems that have thousands of channels or tens of thousands of pixels, due to their relatively large size, high costs, huge power consumption and heat dissipation. On the contrary, the integrated circuit (IC), which is also called monolithic integrated circuit, is a set of electronic circuits constructed in one small piece of silicon and is much smaller than the discrete circuit which is made from independent electronic components. With all electronic components printed as a unit by photolithography [50], package ICs use much less material than discrete circuits and the cost is lower as a result. Furthermore, because the components on ICs switch more quickly and consume less power as a result of smaller size and closer proximity of the components, ICs have higher performance. Advances in IC technology, particularly recent development of chip-level application specified integrated circuit (ASIC) electronics has made it possible to provide fast, multichannel readout electronics for X-ray imaging systems.

As described in Section 1.4.2, photon-counting systems only count and digitalize analog signals whose voltage gain exceeds a preset threshold and have higher SNR of image compared with conventional energy-integrating systems. Recent studies have also shown that ideal energy-sensitive photon-counting detectors applying optimal energy weighting schemes have the potential to further increase the contrast-to-noise ratio and to discriminate between different materials [51, 52]. Thus the signal processing should retain the energy information and not just detect the presence of an event. However, such a feature has to be satisfied without adding too much circuit complexity in the ASIC chip which has already a very high functional density.

An analog-to-digital converter (ADC) is the conventional device that converts an analog quantity to a digital number that represents the quantity's amplitude. Flash ADC is one of the most common ADCs, however, it requires a large number of comparators to realize accurate conversion. A flash converter requires 2^N-1 comparators for an N-bit conversion. ADCs of this type suffer from a large die size, a high input capacitance and high power dissipation. Other types of ADCs such as successive-approximation ADC and Wilkinson ADC need fewer comparators, however, they suffer from relatively lower conversion speed. On the contrary, Time-over-threshold (ToT, [53, 54]) technique can be realized within a very high-density ASIC while keeping energy information of the detected events. ToT circuit realizes analog-to-digital conversion with only one comparator. The pulse duration is equal to the time when the shaped signal exceeds the preset threshold and carries the charge information of the detected event.

4.1 Integrated circuit technology

4.1.1 A brief history of integrated circuit

The invention of vacuum tube launched and ruled the electronics industry in the first half of 20th century. However, vacuum tubes were bulky, expensive, power-hungry and unreliable, and limited commercial and military electronic systems. William Shockley and his colleagues at Bell Laboratories invented the transistor in 1947 [55, 56], ushering in the solid-state era of electronics. Jack Kilby of Texas Instruments invented the first working planar IC in 1958 [57]. The invention of the IC revealed the potential for extending the cost and operating benefits of transistors to all massive electronic circuits, and IC industry has undergone rapid advances. The number of transistors on one IC has doubled approximately every 18 to 24 months, following Moore's law [58, 59] stated in 1965. According to the density of transistors per IC, development of the IC technology is classified as the following generations [60]:

Small scale integration (SSI): it was crucial to early aerospace projects, and the number of transistors integrated on a single chip was less than 100 in early 1960s. Typical SSI circuits include gates, flip-flops, op-amps, et al.

Medium scale integration (MSI): the number of transistors was several hundred on a single chip in late 1960s. Counters, MUX, adders, 4-bit microprocessors are some examples of MSI circuits.

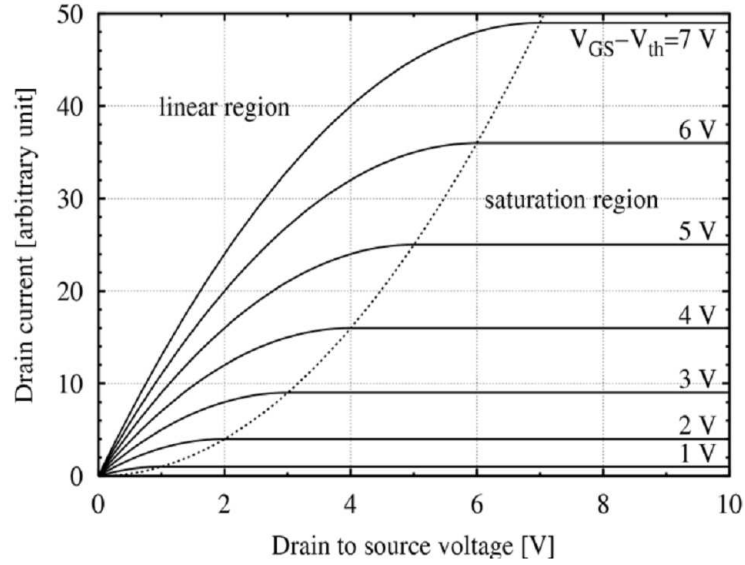


FIGURE 4.1: Dependence of drain current on drain to source voltage.

Large scale integration (LSI): The technology was developed by integrating the number of transistors of 1000-10000 on a single chip in 1970s. Examples are 8-bit microprocessors, ROM, RAM, and so on.

Very large scale integration (VLSI): the number of transistors was from 10 thousand to 1million on a single chip in early 1980s. Multifunction can be realized by one chip. Examples are 16-32 bit microprocessors, peripherals, complimentary high MOS.

Ultra large scale integration (ULSI): the number of transistors of more than 1million on a single chip in late 1980s. Intel 486 and the Pentium series of processors were built on ULSI principles.

Nowadays, hot topics of integration circuit include the wafer-scale integration (WSI), system-on-a-chip (SoC) and three-dimensional integrated circuit (3D-IC).

4.1.2 CMOS technology

MOS stands for Metal-Oxide-Semiconductor Field-Effect-Transistor (FET), and it is the basic element in the design of a large scale integrated circuit. MOS transistor is a voltage controlled device and consists of three regions, source, drain and gate. The source is the terminal, or node, which acts as the source of charge carriers; charge carriers leave the source and travel to the drain. Figure 4.1 shows the dependence of drain current on the drain to source voltage.

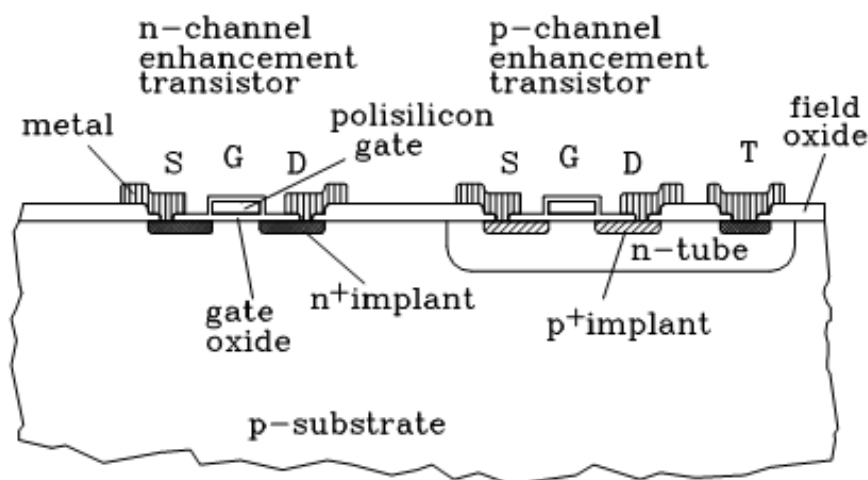


FIGURE 4.2: CMOS technology: n- and p-channel enhancement transistors.

Complementary metal oxide semiconductor (CMOS) electronics integrates both n-channel MOS (NMOS) and p-channel MOS (PMOS) on the same chip (see Figure 4.2). These complementary transistors are insulated from each other by putting one of them into a well with opposite doping to the original bulk material. Such a well is usually produced by diffusion or by implantation and following drive-in diffusion [41].

Two important advantages of CMOS devices are high noise immunity and low static power consumption. CMOS devices do not dissipate as much heat as other forms of logic, such as NMOS or transistor-transistor logic (TTL) logic. CMOS also allows a high density of logic functions on a chip and dominates the fabrication of ICs. The scale-down of the feature size in CMOS technology has fulfilled Moore's law over the years [61]. Whereas the gate lengths of early CMOS transistors were in the micrometer range and the feature sizes of current CMOS devices are in the nanometer range.

CMOS is the most used technology in VLSI or ULSI circuit chips. As of 2010, CPUs with the best performance per watt each year have been CMOS static logic since 1976.

4.1.3 ASIC

Unlike multi-function standard product ICs for general-purpose use, an ASIC is a type of IC customized for a particular use. According to the signals to be processed, ASICs can be generally categorized into digital ASIC, analog ASIC and mixed-signal ASIC.

Digital ASICs can be built using a standard cell library consisting of fixed-height, variable-width 'tiles' containing various digital logic functions. The ability to reuse these blocks over and over saves time and money when designing a custom logic IC. Analog ASICs were initially comprised of a pair of matched transistors and soon expanded to include rudimentary op amps, voltage regulators, comparator, timers and much more. Modern analog circuits require digital control or tuning, as a result, there are very few pure analog ICs and analog and digital functionality is merged on a single silicon chip that is referred as the mixed-signal ASIC. With the help of mixed-signal ICs, analog signals are converted to digital signals that can be easily processed by digital devices. Mixed-signal ICs are more difficult to design and manufacture than analog-only or digital-only ASICs.

There are various versions of ASIC design flow in industry. Each company or research group bases their flow on specific resources and tools. Generally the mixed-signal flow is a top-down process and can be divided into two main phases mapped closely to the front-end and back-end computer-aided design (CAD) tools. The front-end tools are used for behavioral modelling and simulation, logic synthesis, optimization mapping, test synthesis, schematic capture and simulation analysis. The back-end tools are used for layout, place, route and verification [56]. VLSI Design and Education Center (VDEC), which is located in the University of Tokyo, distributes VLSI design information, provides CAD software and licenses and supports chip designs, fabrications and measurements with lower costs [62].

4.2 Principle of ToT method

ToT method is a type of signal processing method which transfers analog signals into digital signals. The principle of ToT method is shown in Figure 4.3.

The charge signal from the detector is firstly integrated by a preamplifier, and then processed by a shaping amplifier (shaper). The shaping amplifier is usually designed with semi-Gaussian shaping. The preamp-shaper processing chain is a linear system similar with electronics in spectrometry applications. The peak amplitude of the shaper output is proportional to the input charge (deposited energy) from the detector. The shaper signal is then output to a comparator whose threshold is set above the noise or with some other preset value, a digital pulse is generated at the output terminal with duration equal to the time during which the shaper signal exceeds the threshold. The relationship between the output ToT and input charge is nearly logarithmic. By resolving the width of the output ToT signal, the digitized information of the deposited

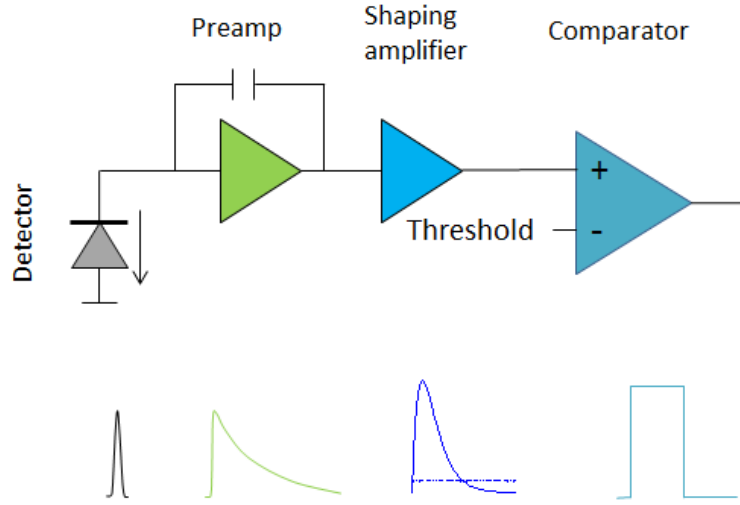


FIGURE 4.3: Block diagram and signal flow of ToT method.

energy can be obtained. Furthermore, the nearly logarithmic ToT response allows larger dynamic range with fewer bits.

In principle, the ToT method converts analog signals to digital signals with only one comparator. Such a simple structure is beneficial to decreasing circuit complexity in a chip which is key important for imaging systems with more than thousands of channels.

4.3 ToT ASIC

A 48-channel ASIC based on ToT method was designed and fabricated using a 0.25 μm 3.3 V Taiwan Semiconductor Manufacturing Company complementary metal oxide semiconductor (TSMC CMOS) process [63]. The chip has a die of 2 mm \times 5 mm. Each channel of the ASIC consists of a charge-sensitive preamplifier, a shaping amplifier and a comparator whose threshold is controlled by a 12 bit DAC. Figure 4.4 shows a picture of the board and die of the ToT ASIC. On the ASIC die, 48 input pads are located on the left side and the 48 output pads are located on the right side, while pads connected to chip bias and threshold DAC are located on the top and bottom sides.

4.3.1 Charge-sensitive preamplifier

For most detectors, the charge is so small that intermediate amplification is required. A preamplifier is located as close as possible to the detector and converts the small charge to a voltage signal that can be easily processed.

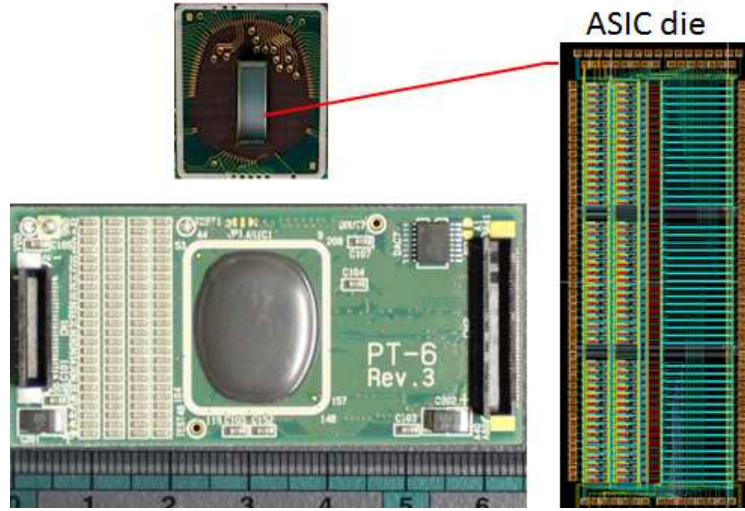


FIGURE 4.4: Board and die of the 48-channel ToT ASIC.

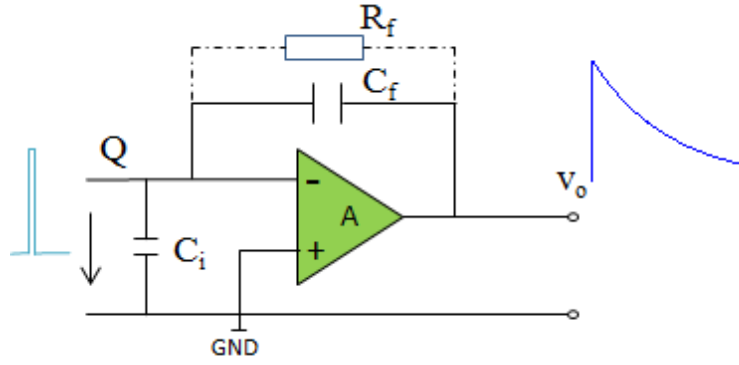


FIGURE 4.5: Simplified diagram of a charge-sensitive preamplifier.

Figure 4.5 shows a simplified diagram of a charge-sensitive preamplifier. The current pulse induced by the detection of an ionization radiation is integrated on the feedback capacitor and the amplitude of the output voltage signal V_o can be expressed as:

$$V_{out} = A \frac{Q}{C_i + (A + 1)C_f} \quad (4.1)$$

Where A is the gain of the amplifier, C_i is the input capacitance and C_f is the feedback capacitance. Assume $A \gg (C_i + C_f)/C_f$ which is always true in a preamp, $V_{out} = \frac{Q}{C_f}$, indicating that the output voltage is proportional to the integrated charge in the current pulse and is independent from the input capacitance. To limit pulse pileup, a large-value resistor R_f is connected parallel to the feedback capacitor to discharge it, and the output voltage decays exponentially with time with a time constant of $\tau = R_f C_f$.

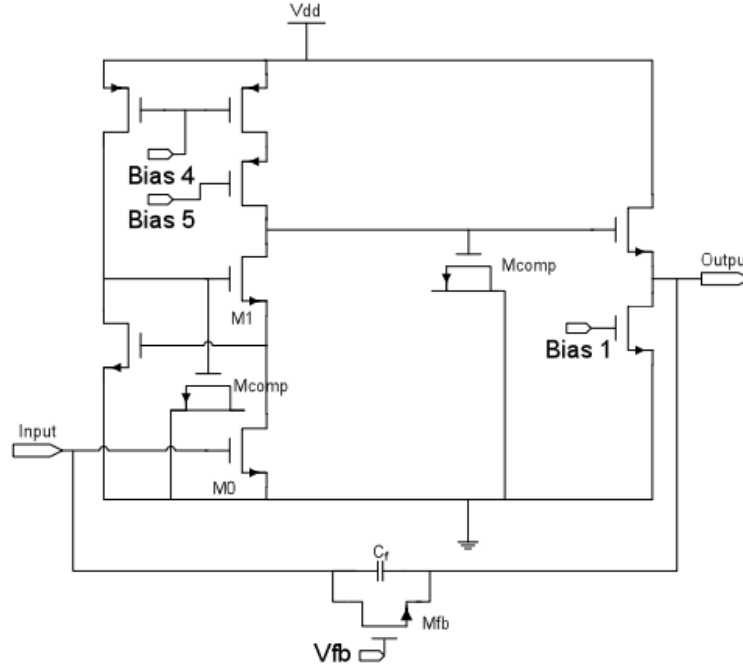


FIGURE 4.6: Schematic of the preamplifier implemented in the ASIC.

Preamplifiers implemented in the 48-channel ASIC is based on the gain-booster (regulated) cascode topology [64, 65], and a schematic of the preamplifier is shown in Figure 4.6. Benefitting from higher transconductance, NMOS transistors were chosen in the design although they have higher flicker noise compared with PMOS transistors. Because large value resistors are impossible to be placed into a die with limited area, a NMOS transistor biased at the triode region is used as the feedback resistor (M_{fb}) of the preamp and can be adjusted by controlling the gate voltage (V_{fb}). The feedback capacitor (C_f) is 200 fF and the gain of the preamp is set to be 5 V/pC.

4.3.2 Shaping amplifier

A shaping amplifier is usually located behind the preamplifier, performing key functions. Its primary function is to further magnify the amplitude of the preamplifier output for facilitating accurate pulse amplitude measurements. Furthermore, the shaper shapes the pulses to minimize the risk of overlap between successive signals and optimize signal-to-noise ratio (SNR).

The simplest shaping method is the CR-RC shaping with a CR high-pass filter followed by an RC low-pass filter as shown in Figure 4.7. The $C_D - R_D$ high-pass filter provides a derivation of the input pulse and improves the signal-to-noise ratio by attenuating the low frequencies that contain a lot of noise and very few signals. The

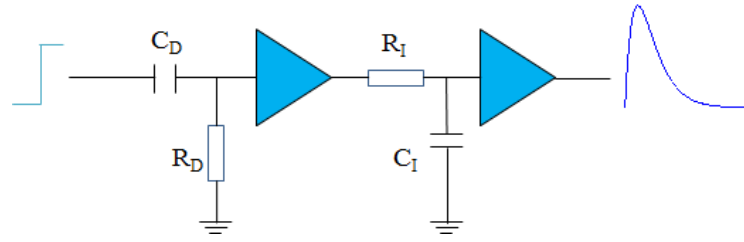


FIGURE 4.7: Schematic of CR-RC pulse shaping.

$C_I - R_I$ low-pass filter behaves like an integrator and improves the SNR by attenuating high frequencies that contain excessive noise. Typically, the differentiation time constant $\tau_D = C_D R_D$ is set equal to the integration time constant $\tau_I = C_I R_I$, and the output of the shaper has a semi-Gaussian waveform expressed as:

$$V(t) = \frac{Q}{C_f} \frac{t}{\tau_D} e^{-t/\tau_D} \quad (4.2)$$

There is a noticeable undershoot as the amplifier pulse is returning to the baseline in the simple CR-RC circuit as a result of the long exponential decay of the preamplifier output pulse. Most shaping amplifiers incorporate a pole-zero cancellation (PZC) circuit to eliminate this undershoot. In addition, several orders of CR differentiator and RC integrator or a more complicated active integrator network are used to further improve the SNR and reduce the output pulse width with little pulse height loss.

The Bridge-T structure is adopted in the shaper design of the ToT ASIC, and the complete schematic is shown in Figure 4.8. A PZC circuit is added in front of the shaper to remove the undershoot.

4.3.3 Comparator

Intrinsically a comparator is an open-loop operational amplifier. The comparator implemented in the ASIC is based on folded-cascade topology and the schematic is shown in Figure 4.9 [66].

4.3.4 DAC

There are in total 7 DAC chips (DAC128S085 12-bit DAC [67]) implemented on one ASIC board, and each DAC chip has 8 outputs. Pin configuration of the DAC chip is shown in 4.10. Six chips supply threshold of 48 channels and the other chip is used

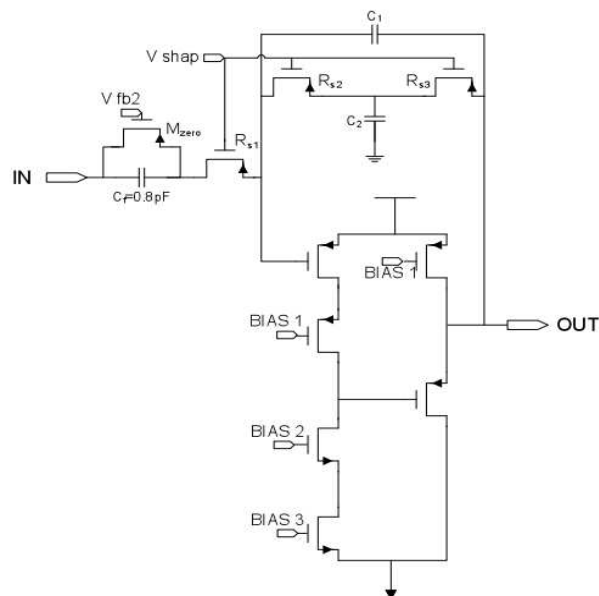


FIGURE 4.8: Schematic of the shaper with PZC circuit.

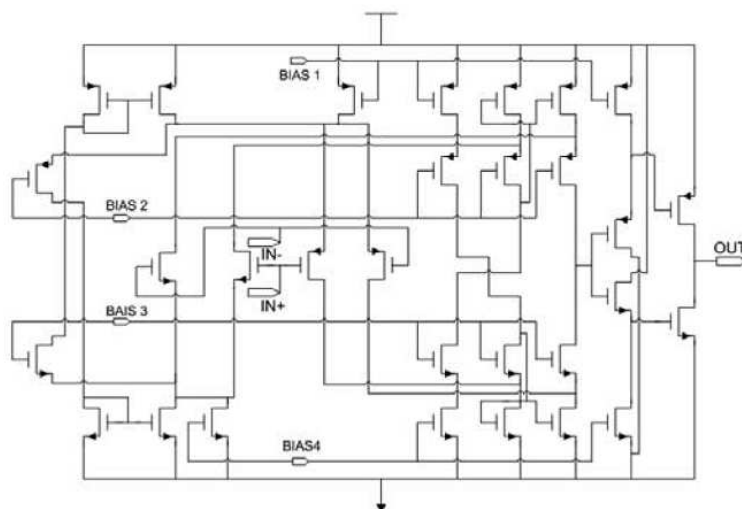


FIGURE 4.9: Schematic of implemented comparator.

to set quiescent operation points of preamps and comparators. The accuracy of digital-analog conversion reach as low as $\tilde{0.8}$ mV with a 3.3 V power supply. The DAC128S085 chip offers daisy chain operation where an unlimited number of DAC128S085s can be updated simultaneously using a single serial interface. To support multiple devices in a daisy chain configuration, SCLK and \overline{SYNC} are shared across all DAC128S085s and DOUT of the first DAC is connected to DIN of the second.

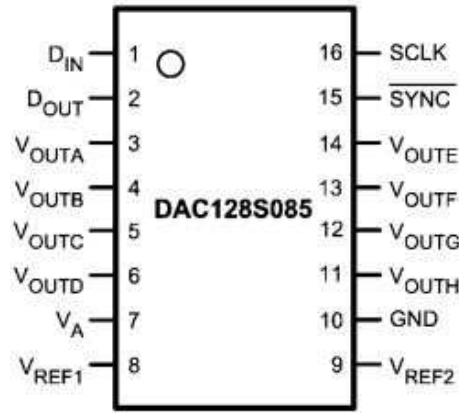


FIGURE 4.10: Pin configuration of the DAC128S085 12-bit DAC.

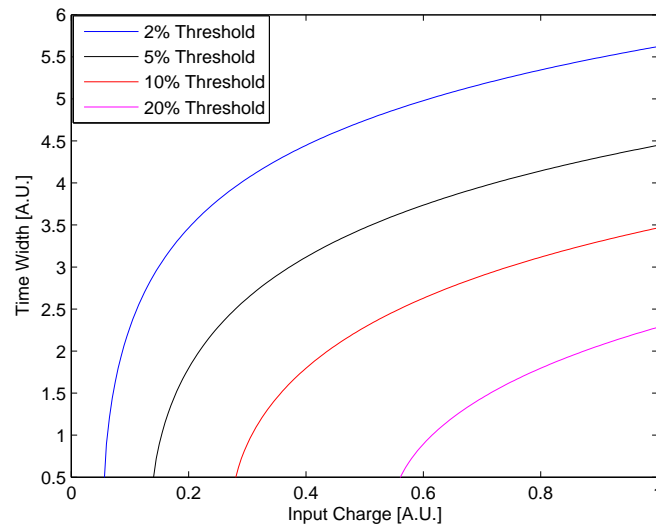


FIGURE 4.11: ToT responses to the input charge at different threshold levels.

4.3.5 Response of ToT to input charge

ToT method with a constant threshold suffers from severe nonlinearity and the nonlinearity depends on the shaping method. Take the CR-RC shaper as an example, the ToT responses to the input charges at different threshold levels are simulated and shown in Figure 4.11. Severe nonlinearity is observed especially when the input is small and the threshold level is low. The linearity is improved when the threshold level is higher; however, the dynamic range of the ToT is narrower when the threshold level is higher. These curves indicate that a good linearity and a wide dynamic range cannot be simultaneously realized with the ToT method. If energy information is needed, the linearity curve has to be measured and the nonlinearity can be calibrated with the linearity curve.

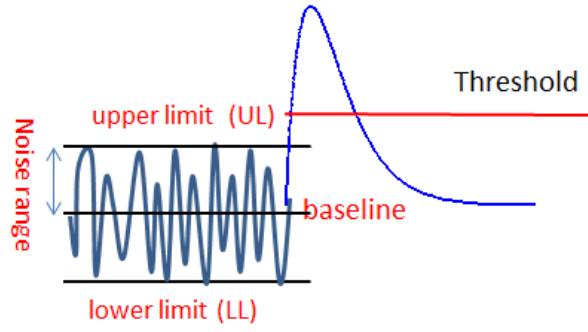


FIGURE 4.12: Demonstration of the baseline and noise of the signal output to the comparator in the ASIC.

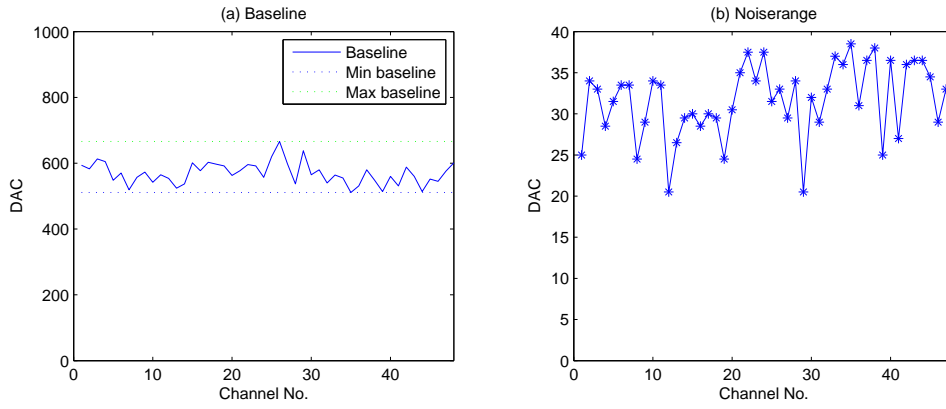


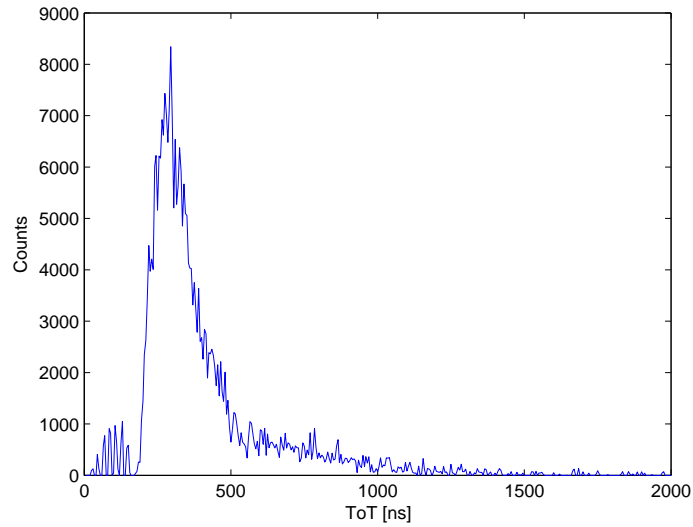
FIGURE 4.13: A scanned baseline and noiserange of one ASIC chip.

4.4 Evaluation of the ToT ASIC

4.4.1 Baseline and noise characteristics

Figure 4.12 demonstrates the signal outputs to the comparator in the ASIC. By adjusting threshold of each comparator and counting the corresponding noisy ToT signals, we obtained the upper limit (UL) and the lower limit (LL) of the baseline that was fluctuating with random noise. The baseline was $(UL+LL)/2$ and the noise range of the channel is $(UL-LL)/2$. The scanned baseline and noiserange of one ASIC chip is shown in Figure 4.13. The scanned ASIC had baselines with a fluctuation of about 150 DAC value, and the noiserange was between 20 and 40 DAC value.

Because the shaping signal of the silicon strip detector has a positive polarity, the threshold value is required to be higher than the noise range so as to avoid oscillating. We set an identical threshold of 50 DAC value (equivalent to be about 180 keV for silicon detector) to all channels in order to achieve approximately uniform response of

FIGURE 4.14: The measured ToT spectrum of ^{137}Cs source.

all channels, however, the response of each channel needs to be calibrated because of gain variation among channels.

4.4.2 ToT spectrum

One ToT ASIC was connected with one silicon strip detector and we measured spectrum of a ^{137}Cs gamma-ray source. Figure 4.14 shows the measured ToT spectrum.

4.5 Dynamic ToT

The ToT method has the potential of increasing integrity and decreasing power consumption. However, the ToT electronics suffers from poor linearity and its application in imaging system is limited particularly when accurate energy information is required. A dynamic ToT method [68, 69] is proposed to improve the linearity of the relationship between the input charge and time duration.

4.5.1 Principle of dynamic ToT

Different from the traditional ToT method which has a constant threshold, the dynamic ToT method has a threshold that is changing to catch up with the signal from the shaper. The principle of dynamic ToT method is demonstrated in Figure 4.15.

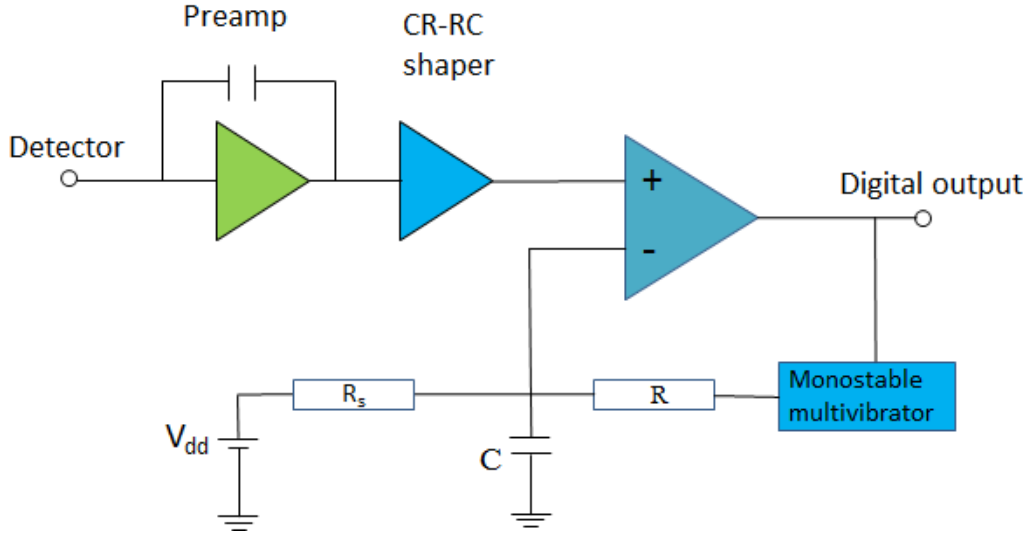


FIGURE 4.15: Schematic of the dynamic ToT circuit.

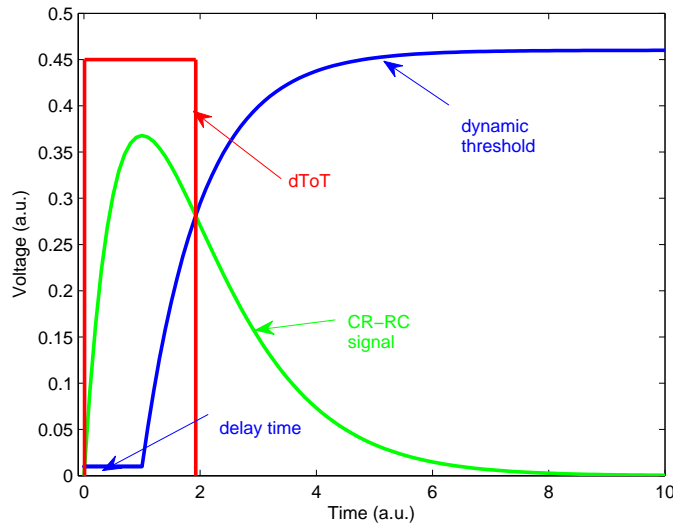


FIGURE 4.16: Waveforms of CR-RC signal, dynamic threshold signal and ToT signal of the dynamic ToT circuit.

The dynamic threshold is generated using a positive feedback from the discriminator output when the shaper signal is higher than a preset initial threshold level. The monostable multivibrator is used to delay the ramp-up of the dynamic threshold signal. The width of the ToT (dToT) equates to the time from the shaper signal cross over the preset initial threshold until the threshold catches up with the shaper signal. It is simulated that the linearity is best and the integral nonlinearity (INL) is 1.6% when the delay time, time constants of CR-RC shaper and threshold are the same [70]. Figure 4.16 shows the shaper signal, the threshold signal and the corresponding dToT signal.

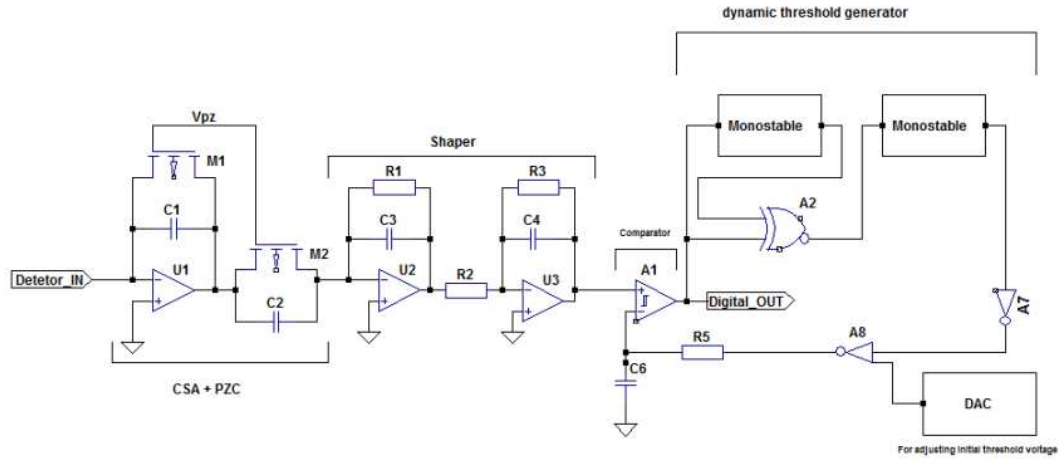


FIGURE 4.17: Schematic of one channel of the 64-channel dynamic ToT ASIC.

With a few more components added, the dynamic ToT method can achieve excellent linearity response between the width of the output digital signal and the input charge. The dynamic ToT electronics has huge potential in imaging applications particularly systems which require energy information. However, there is also one drawback that the current circuit can only fit for signals with one fixed polarity.

4.5.2 Dynamic ToT ASIC

A 64-channel dynamic ToT ASIC had been fabricated. Figure 4.17 shows a brief schematic of one channel of the ASIC [71].

Figure 4.18 shows the layout of the 64-channel dynamic ToT ASIC [71]. On the ASIC die, 64 input pads are located on the left side and the 64 output pads are located on the right side, while pads connected to chip are located on the top and bottom sides.

However, the currently fabricated dToT ASIC had an opposite polarity to the fabricated strip detector. As a result, we determined to choose the traditional ToT ASIC. We plan to design a new dToT ASIC that fits for the current silicon strip detector and we will implement imaging systems using dToT ASIC.

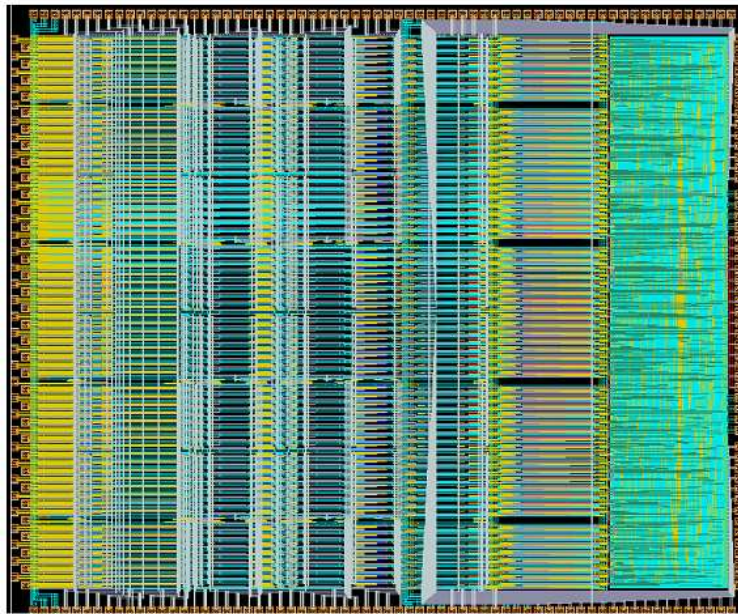


FIGURE 4.18: Layout of the 64-channel dynamic ToT ASIC.

Chapter 5

Development of imaging system

Because the fabricated 64-channel dynamic ToT ASIC is for positive input while the strip detector can only supply negative signals, we design the imaging system based on the 48-channel ToT ASIC. 48 channels of one 50-channel strip detector are connected with one 48-channel ToT ASIC, and the left 2 edge channels are biased with the same high voltage and function as the guard ring.

Two types of imaging systems are developed: the continuous-mode system and the pulse-mode system. The data acquisition (DAQ) system is based on the CX-Card IV series board developed by Prime System, Inc. [72]. There is an Altera Cyclone IV (EP4CE40F23C7N) FPGA on the board. Other important devices include a 48 MHz oscillator for supplying clock (CLK) signals and a 68013 USB interface for exchanging data with PC.

5.1 Continuous-mode system

For applications with gamma-ray sources or X-ray tubes working in continuous mode, usually only one channel outputs signals at one time. As a result, signals of several channels can be wired-OR multiplexed so as to reduce the number of transmission lines. We designed a module consisting of 3 detectors coupled with 3 ASICs (144 channels in total) as demonstrated in Figure 5.1.

The wired-OR multiplexing is realized in the FPGA located in the center and the principle of the multiplexing is demonstrated in Figure 5.2. Assuming only one signal is coming from the detector at (i, j) , only X_i and Y_j have output and the location of the detector which outputs the signal can be calculated as $12 \times (i - 1) + j$. The number

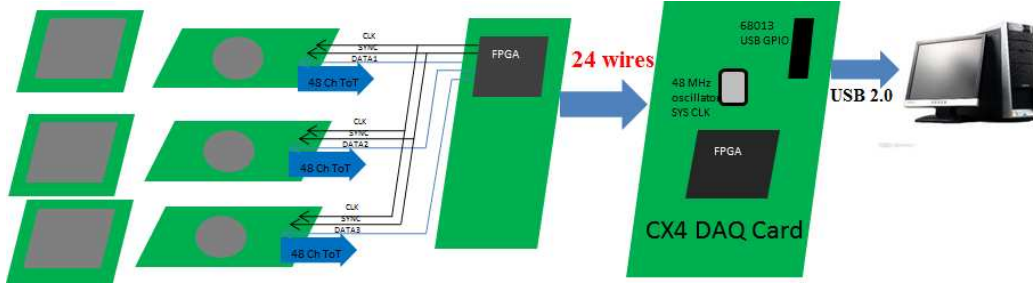


FIGURE 5.1: The continuous-mode system.

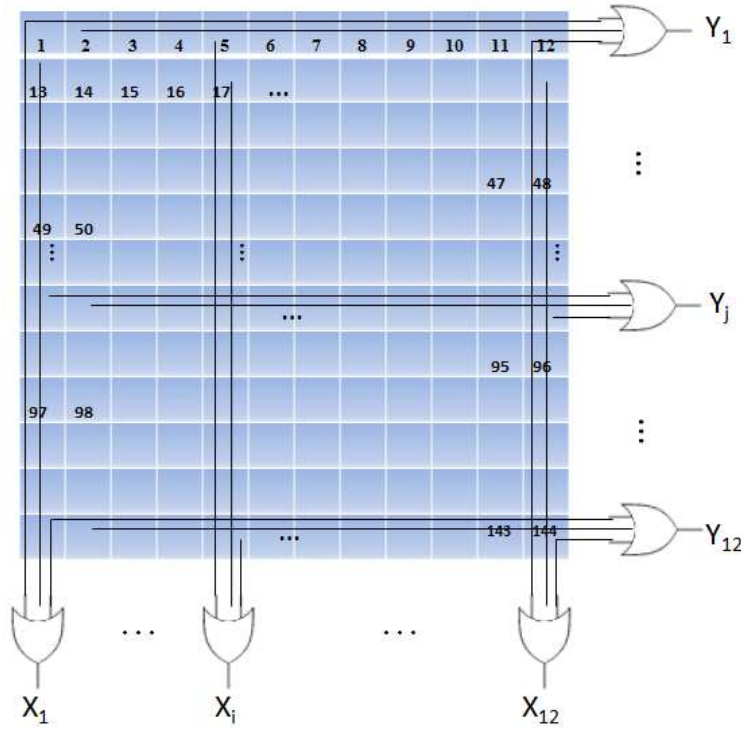


FIGURE 5.2: Wired-OR multiplex readout.

of transmission lines of one 3-detector module is reduced from 144 to 24. The wired-OR multiplexing also adds anticoincidence suppression to scattering influence, which is beneficial to low intensity continuous X-ray or gamma-ray applications. However, the system cannot work normally when a high-intensity X-ray source is used because a lot of channels output signals simultaneously.

We used a ^{137}Cs gamma-ray source to evaluate the continuous-mode system. The source has a cylinder shape with radius of 2.5 mm and thickness of 8 mm, and the intensity is 1 MBq. The clock frequency was set to be 200 MHz and the corresponding time precision was set to be 5 ns. The width of each ToT signal was counted referring to the 200 MHz clock. A plot of 144 ToT spectra with irradiation from the ^{137}Cs gamma-ray source was shown in Figure 5.3. Some channels did not have data because they were

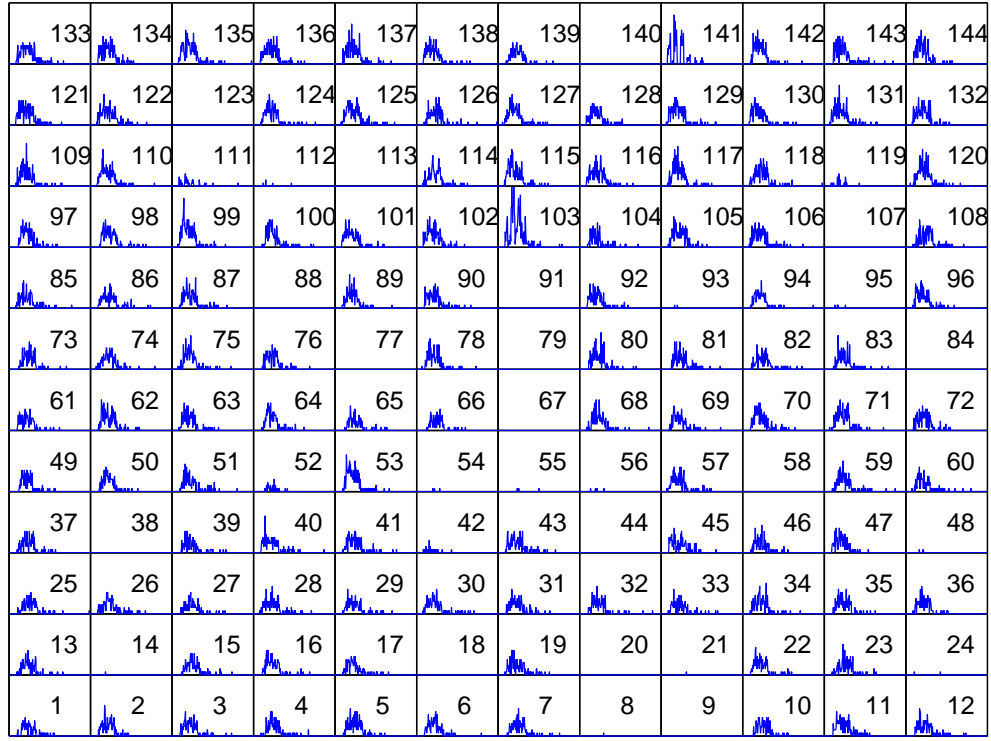


FIGURE 5.3: ToT spectra of 144 channels with irradiation from a ^{137}Cs γ -ray source. Some channels are masked intentionally in the DAQ software.

masked intentionally in the DAQ software. Energy information embodied in the ToT spectra can be used for off-line analysis.

5.1.1 One-layer module

We connected one strip detector with one 48-channel ToT ASIC and proceeded efficiency and spatial resolution evaluation, and we also scanned images of some objects with the one-layer module.

5.1.1.1 Edge-on efficiency

The ^{137}Cs gamma-ray source was placed at 12 cm to the front edge of the detector. The flood-field data of 48 channels were measured for 2500 s and shown in Figure 5.4. Mainly suffered from nonuniformity of gain and threshold of each channel of the ASIC, the approximately uniform flood-field data fluctuated greatly. The average count of each channel was 623. The average efficiency was calculated to be about 9%. It should also be noted that a threshold of about 180 keV was applied to each channel in combination with anticoincidence filter in this measurement.

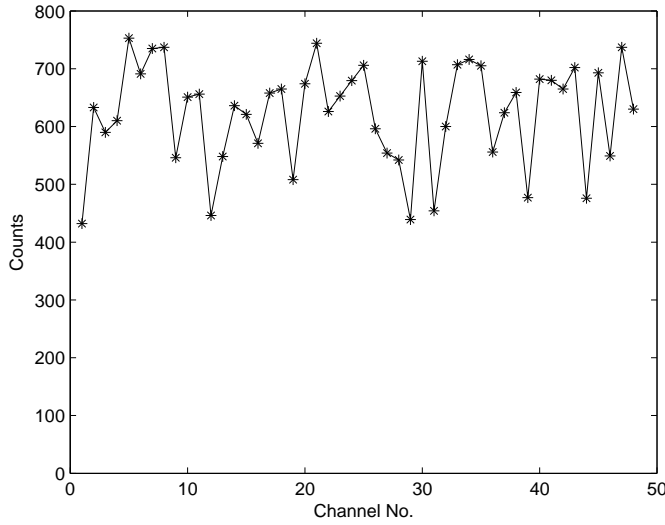


FIGURE 5.4: Count distributions with irradiation from a ^{137}Cs γ source.

5.1.1.2 Edge-on spatial resolution

Figure 5.5 shows the setup for the edge-on position sensitivity measurement. The lead brick was inserted and moved thrice, each time by 1 mm. The measured counts were normalized with the flood-field data and fitted with error function (Equation 5.1) as shown in Figure 5.6. Because the source-to-detector distance was about twice the source-to-object distance, the distance between adjacent edges was about 2 mm. Because the lead brick was too thick and the photons were not collimated, the σ of the error function fitting was about 2 mm, which was much larger than 1/2.355 mm.

$$f(x) = c + a \cdot \text{erf}\left(\frac{x - \mu}{\sigma\sqrt{2}}\right) \quad (5.1)$$

5.1.1.3 Scan imaging of samples

The gamma-ray source should be placed far away from the object for simulating homogenous irradiation from the X-ray generator and the detector should be moved vertically to its surface for simulating the imaging system consisting of stacked strip detectors. However, suffered from limited intensity of the gamma-ray source, the source was placed at about 10 cm in front of the detector and the irradiation incident on the detector was not uniform. The counts obtained at different positions need to be calibrated with the flood-field data measured at the same position if the detector is to

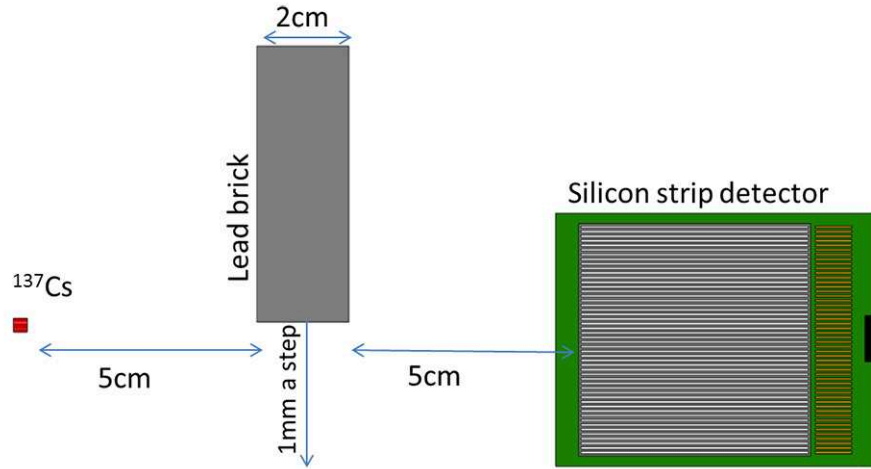


FIGURE 5.5: Setup of the edge-on spatial resolution evaluation.

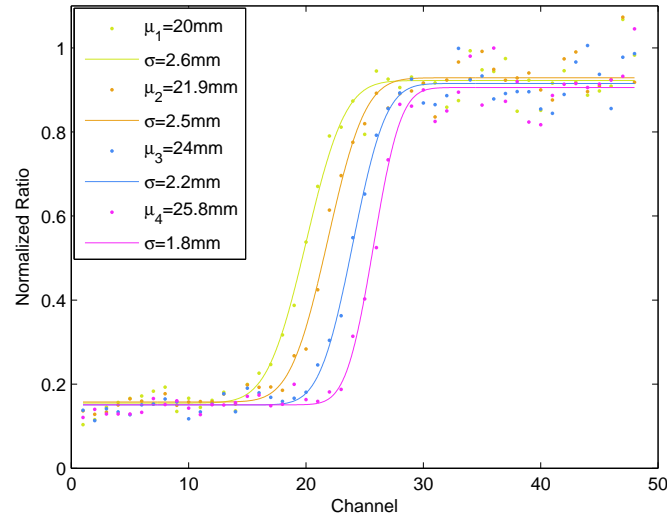


FIGURE 5.6: Normalized and fitted count distributions of four measurements using flood-field data.

be moved, which consumes twice time and also requests for a high-precision platform. Finally we decided to move the object for scan imaging.

We used the one-layer module to scan the image of an iron object. The thickness of the iron object is 3.5 cm. Setup for the scans is shown in the Figure 5.7. The ^{137}Cs source was placed at 17.0 cm in front of the detector, and we measured the flood-field image data. Then the iron object was inserted at 4.5 cm from the ^{137}Cs source and moved perpendicularly to the detector surface in 12 increments of 1 mm. Counts of each step were normalized by the flood-field image data and are shown in Figure 5.8. We can see the central right angle of the object from the image. Because the distance from the

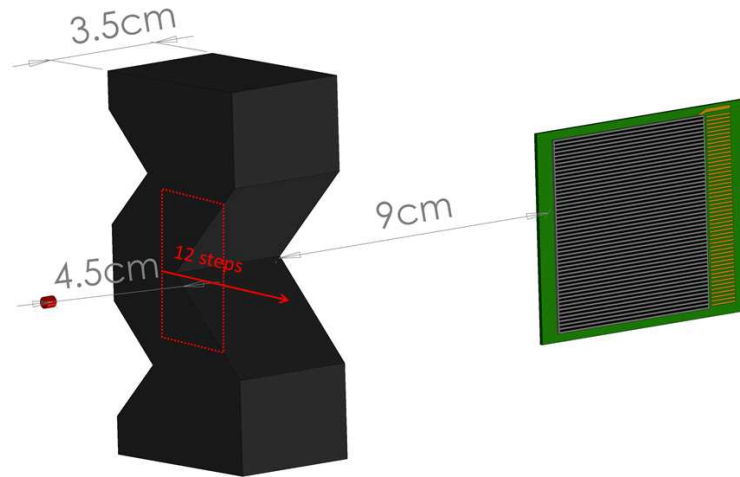


FIGURE 5.7: Setup of the scan imaging of an iron object.

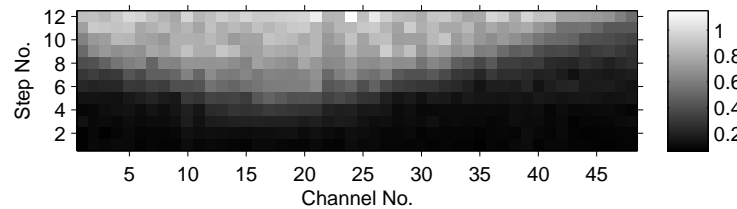


FIGURE 5.8: Scan image of the iron object.

detector to the source was more than twice the distance from the object to the source, the vertical size was amplified and the right angle was distorted.

To validate capability of identifying different materials in a test sample, another iron object was scanned. The object is shown in Figure 5.9(a). The object has a thickness of 1.0 cm and the center is filled with soil. The setup and procedures of the scan imaging was similar with the previous one. The ^{137}Cs source was placed at 15.0 cm in front of the detector, and the iron object was inserted at 9.0 cm from the ^{137}Cs source. The scanned image is shown in Figure 5.9(b). Because the object was placed closer to the detector, the distortion was slighter than the previous image. However, the image was not as clear as the previous image because the thickness was smaller and the density difference between soil and iron was smaller than that between air and iron.

5.1.2 Scan imaging with two-layer module

We stacked two silicon strip detectors to perform 2D scan imaging experiment. The distance between the two detectors was 9.6 mm. The object to be scanned was an R1.5

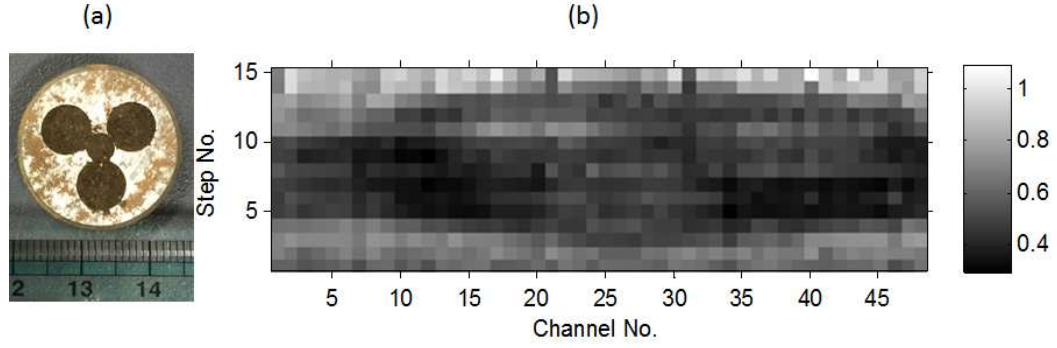


FIGURE 5.9: Scans of an iron object filled with soil. (a) The iron object filled with soil. (b) The scan image of the object.

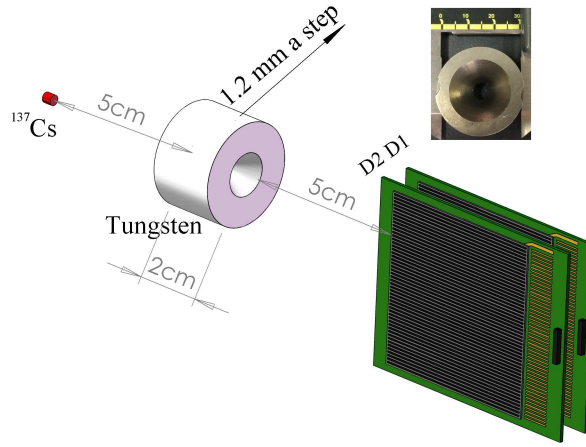


FIGURE 5.10: Setup for the scans of the tungsten object.

cm \times 2.0 cm tungsten cylinder with a conical hole in the center. Figure 5.10 shows the tungsten object and the setup for the scans.

The ^{137}Cs source was placed at 12.0 cm in front of the 2 detectors, and we measured the flood-field image data. Then the tungsten object was inserted at 5.0 cm from the ^{137}Cs source and moved perpendicularly to the detector surface in 9 increments of 1.2 mm. Counts of each step were normalized by the flood-field image data and are shown in Figure 5.11. The central hole and the outer edge of the tungsten cylinder are clearly visible. A splice of the two images are shown in Figure 5.12 and a wider region of the sample is imaged. However, the image obtained with the second detector cannot be spliced above the 8th data of the first detector, because photons were not incident parallel to the detectors. However, this splice can be expected when the photon source is placed far enough from the object.

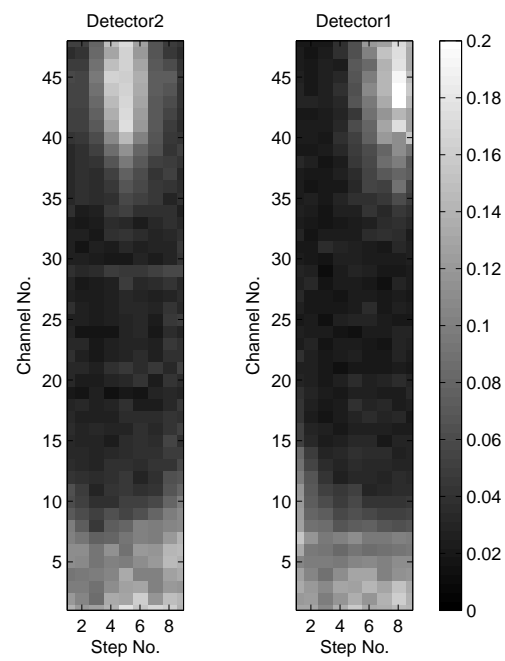


FIGURE 5.11: Nine-step scan images of the tungsten object using two detectors.

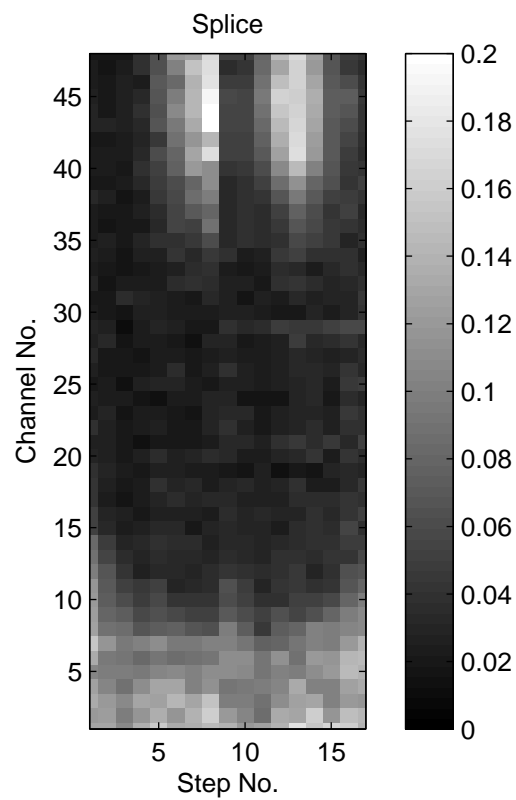


FIGURE 5.12: Splice of two scanned images.

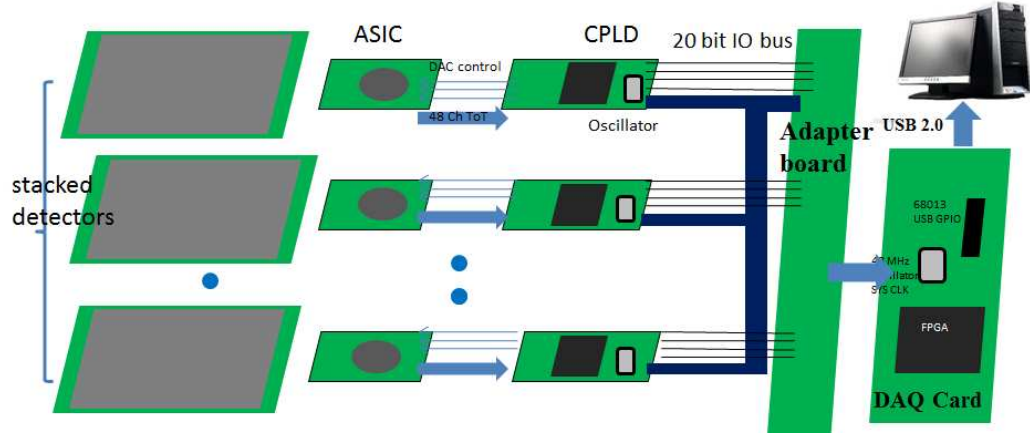


FIGURE 5.13: The pulse-mode system.

5.2 Pulse-mode system

High-intensity X-ray sources such as the X-band LINAC X-ray generator are usually working in pulse mode. A lot of photons are incident on the stacked detectors and tens of or hundreds of channels output signals simultaneously in the X-ray pulse. As a result, the location of the channels which output signals cannot be resolved in the continuous-mode system. Therefore, a pulse-mode system was designed as shown in Figure 5.13. Each Complex Programmable Logic Device (CPLD) is connected with one ASIC which is coupled with one strip detector. ToT signals of each channel are counted independently and the numbers of signals are stored in each CPLD during DAQ. The numbers of signals are transferred to the DAQ card when the acquisition is completed.

Limited by the number of IOs on the CX-CardIV DAQ card, one module can only support at most 8 layers. We constructed a module stacked with 6 layers as shown in Figure 5.14. The distance between adjacent layers was 6 mm.

5.2.1 Gamma-ray imaging with the ^{137}Cs source

We evaluated the pulse-mode module with the 1 MBq ^{137}Cs gamma-ray source.

5.2.1.1 Edge-on efficiency

The ^{137}Cs gamma-ray source was placed at 12 cm to the front edge of the detector. The flood-field counts of the 6 stacked detectors were measured for 3600 s and shown in Figure 5.15. Mainly suffered from nonuniformity of gain and threshold of each channel

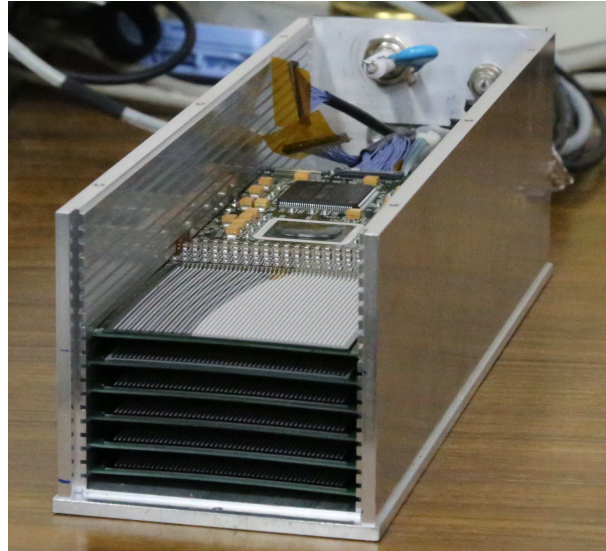
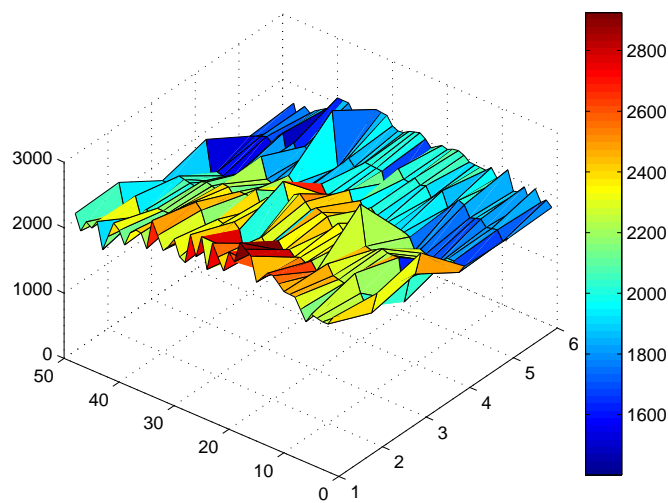


FIGURE 5.14: The constructed pulse-mode module with 6 stacked layers.

FIGURE 5.15: Flood-field counts with irradiation from a ^{137}Cs γ source.

of the ASIC, the approximately uniform flood-field data fluctuated greatly. The average count of each channel was 2100. The average count efficiency was calculated to be about 20%. The efficiency was much higher than the efficiency of the one-layer continuous module, because there was no anticoincidence filter and also the stacked geometry enhanced scattering inside the 6-layer module.

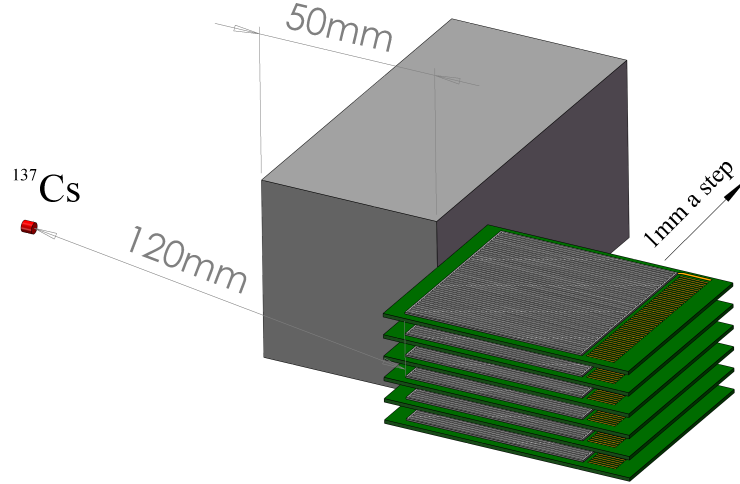


FIGURE 5.16: Setup for the edge-on spatial resolution evaluation of the 6-layer module with the 1 MBq ^{137}Cs source.

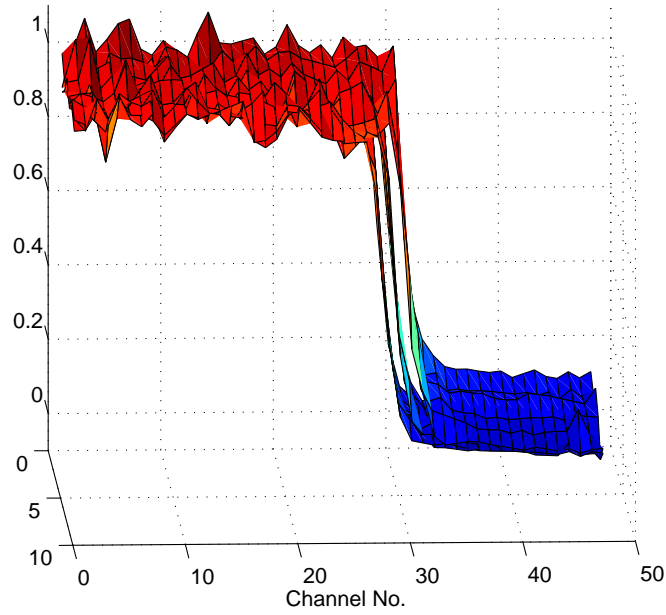


FIGURE 5.17: Normalized count distributions of 3 measurements.

5.2.1.2 Edge-on spatial resolution

Figure 5.16 shows the setup for the edge-on spatial resolution evaluation. A 50-mm-thick lead brick was inserted and the detector module was moved twice, each time by 1 mm. The measured counts were normalized with the flood-field data and shown in Figure 5.17.

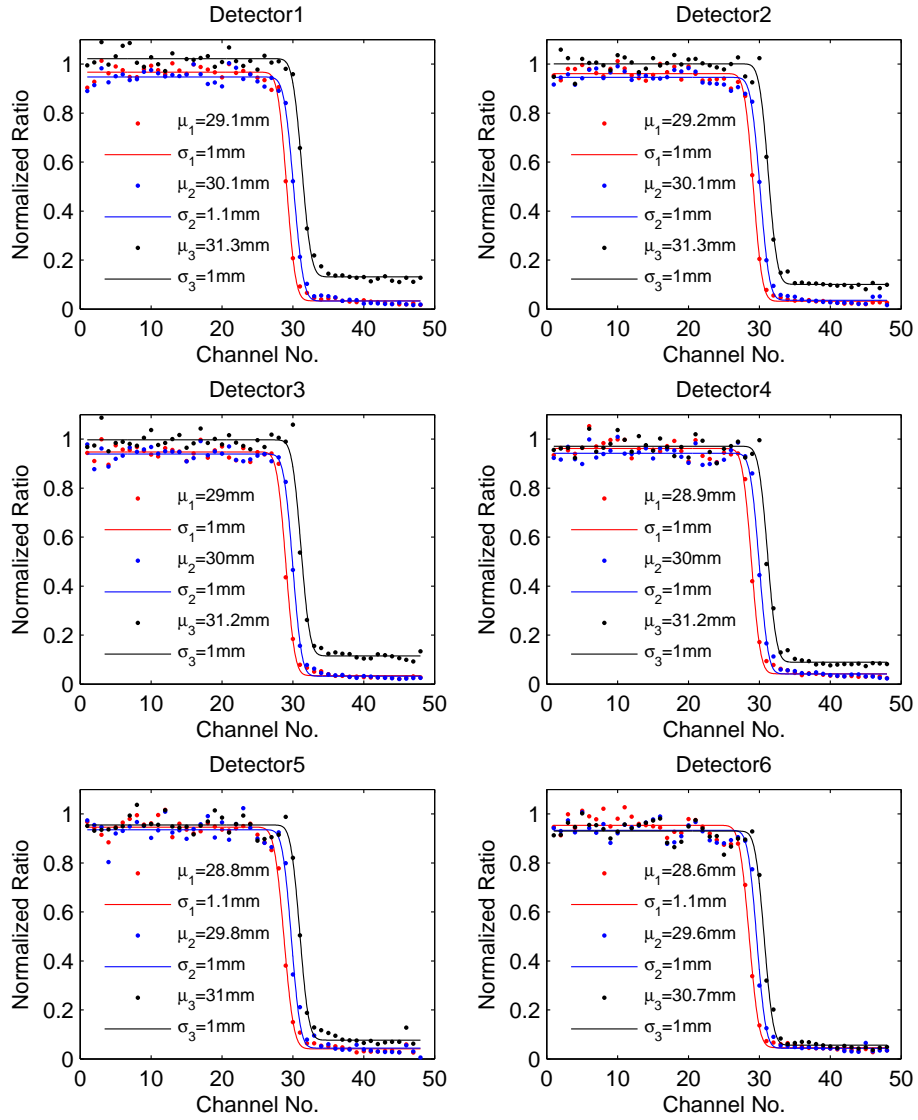


FIGURE 5.18: Normalized and fitted count distributions of 3 measurements of 6 detectors.

Figure 5.18 separately shows the normalized counts of 6 detectors and the fitting results with the error function (Equation 5.1). σ of fittings is generally about 1 mm, and distance between two adjacent falling edge is about 1 mm that is the same with the step size.

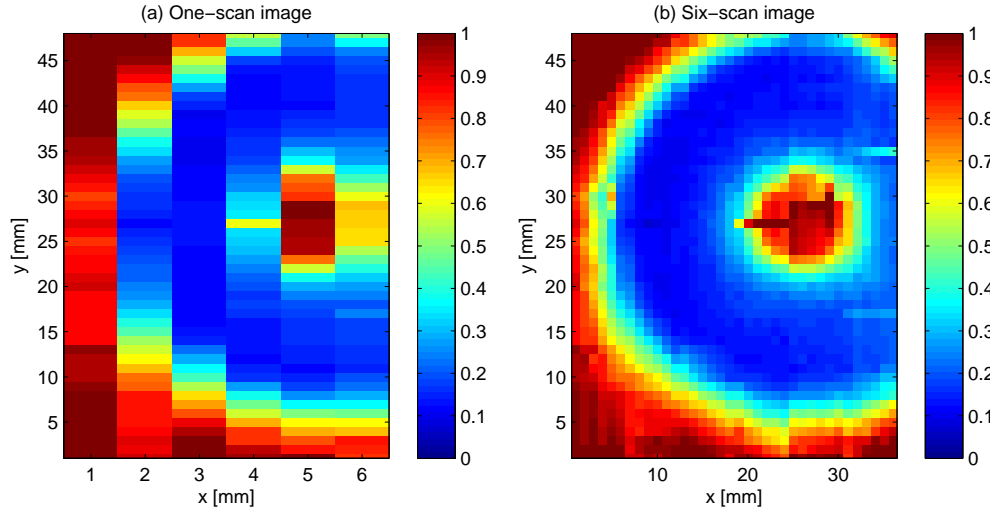


FIGURE 5.19: One-scan and six-scan images of the tungsten sample.

5.2.1.3 Scan imaging of samples

The 6-layer module was used to scan the image of the 2-cm-thick tungsten sample shown in Figure 5.10. The ^{137}Cs source was placed at 10.5 cm in front of the detector module and the flood-field counts were measured for 3600 s. The tungsten object was inserted at 0.5 cm in front of the detector module and irradiated for 3600 s. The measured counts were normalized with the flood-field counts and image was obtained as shown in Figure 5.19(a). The detector module was moved 5 times, each time by 1 mm and measured for 3600 s. All the normalized data of six scans were spliced and the six-scan image is shown in Figure 5.19(b). Compared with the one-scan image, the six-scan image represents more details of the sample. Furthermore, because we moved the detector module instead of moving the sample, the obtained scan image was not distorted. The scan image obtained with the fifth detector (from 25 mm to 30 mm) was a little distorted because the fifth layer was displaced.

We adjusted the fifth detector and used the detector module to scan the iron object shown in Figure 5.9. The One-scan and Six-scan images of the object are shown in Figure 5.20. The soil and iron can be clearly distinguished.

It is observed that the images of the objects were amplified because the photons were not incident on the object in parallel. We can expect real representations of samples when a LINAC X-ray source is used because the paralleled incidence of photons is guaranteed. Furthermore, because LINAC X-ray has much stronger intensity, a full image of the sample can be realized within much shorter time.

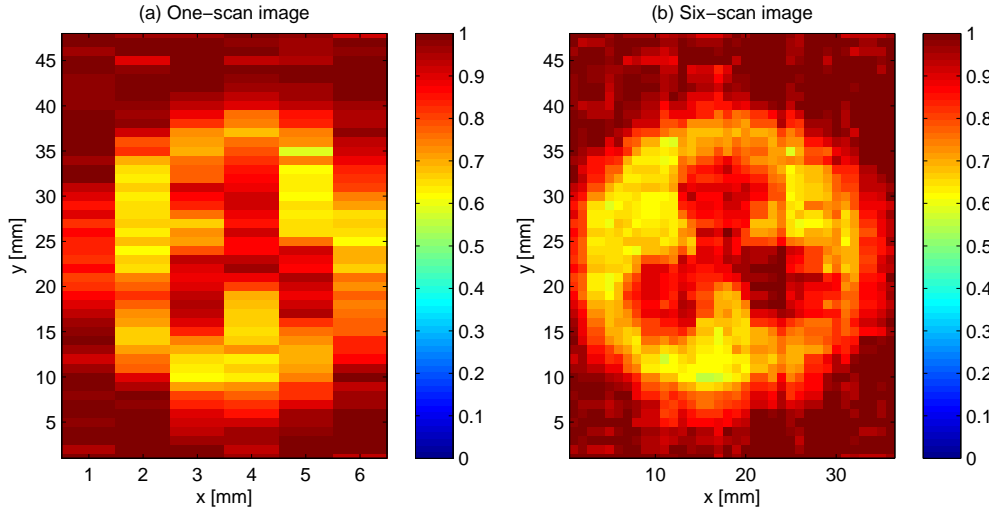


FIGURE 5.20: One-scan and six-scan images of the iron sample filled with soil.

5.2.2 X-ray imaging the 0.95 MeV LINAC X-ray generator

We evaluated the 6-layer imaging module with the X-band 0.95 MeV LINAC X-ray generator. The LINAC worked at 3.9 mGy/min and 200 pps during evaluations. The detector module was placed at 1.5 m to the LINAC. Because the LINAC was initially designed for traditional energy-integrating imaging applications, the high intensity guaranteed capability of imaging much thicker samples when our photon-counting system is used. However, the high intensity would lead to pileup of signals when there is no enough medium between the photon-counting imaging module and the LINAC. We placed a 2.5-cm-thick lead filter at 5 cm in front of the LINAC in the following measurements.

5.2.2.1 Edge-on spatial resolution

Similar with procedures introduced previously, we firstly measured the flood-field distribution of the detector module. The average count of each channel was 3.8×10^4 in 180 s. A 2-mm-thick lead brick was inserted to shield part of the module and the count was measured for another 180 s. The count was normalized with the flood-field data as shown in Figure 5.21(a). The distribution was fitted with the error function (Equation 5.1) as shown in Figure 5.21(b). σ of fitted distributions is generally about 1 mm.

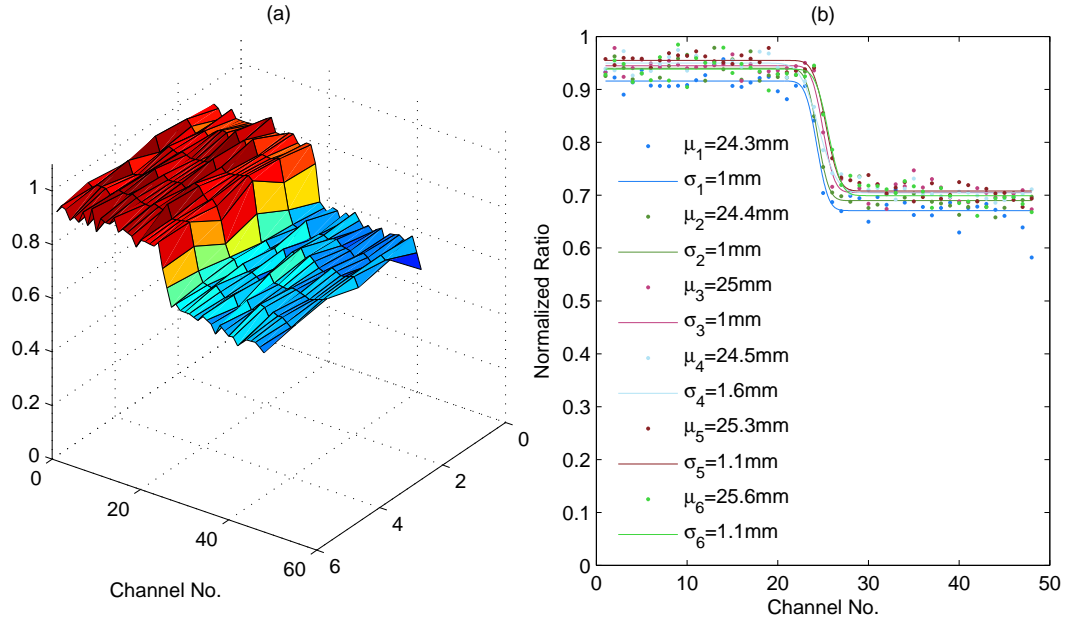


FIGURE 5.21: Count distributions when the a part of the detector module was shielded with a 2 mm thick lead. (a) Distributions of six layers (b) Fitting of six distributions.

5.2.2.2 Scan imaging of samples

We used the detector module to scan images of the tungsten object and the iron object. Similar with procedures described in Section 5.2.1.3, one full image was realized with 6 scans. Each scan of the tungsten object lasted for 300 s, and each scan of the iron object lasted for 180 s. The obtained images are shown in Figure 5.22. Compared with images shown in Section 5.2.1.3, the samples were more clearly represented because better statistics was realized by high-intensity X-ray source even within much shorter time. Furthermore, the images also reproduced the real size of samples because incidence of photons on the object can be approximately treated parallel.

5.2.2.3 Scan imaging of reinforcing bars inside concrete

The detector module was also used to image a 20-cm-thick concrete. There were 5 reinforcing bars inside the concrete.

The concrete was firstly imaged with a Perkin Elmer XRD1622 flat panel detector [73]. The flat panel detector has a fluorescent screen consisting of 400 μm -thick GOS scintillator and a TFT/diode array fabricated on a single substrate amorphous silicon. The detector has a 41-cm field of view with a pixel matrix of 2048×2048 at 200- μm pitch. The detector supports energy-integrating X-ray imaging with energy that ranges

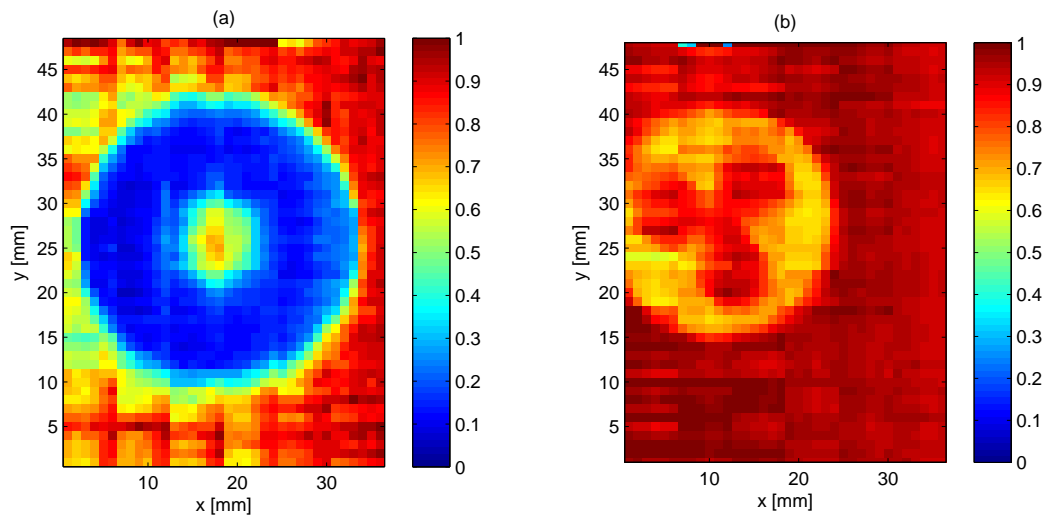


FIGURE 5.22: Six-scan images of the tungsten object and the iron object.(a) Image of the tungsten object.(b) Image of the iron object.

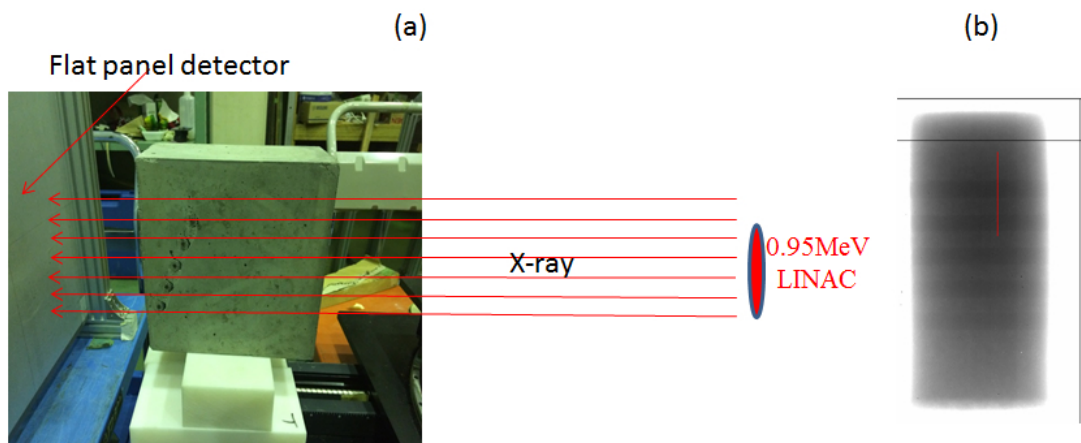


FIGURE 5.23: Scan imaging of a 20 cm thick concrete. The darker parts represent the iron reinforcing bars.

from 20 keV to 15 MeV. The setup for the imaging is shown in Figure 5.23(a). The lead brick was removed during the imaging. The obtained image in 10 s is shown Figure 5.23(b). Reinforcing bars inside the concrete were observed.

A 1.2-cm-thick lead brick was inserted at 5 cm in front of the LINAC to simulate a thicker sample, and the concrete was imaged with the flat panel detector again. The obtained image in 180 s is shown in Figure 5.24(a). The reinforcing bars inside were invisible because the concrete was beyond the dynamic range of the energy-integrating flat panel detector when the lead brick was inserted. We used our photon-counting imaging module to scan the concrete, and each scan lasted for 180 s. The image is shown in Figure 5.24(b). We can identify the reinforcing bars in the darker parts,

though the quality of the image was not so good suffered from insufficient statistics. This demonstrates advantage of our photon-counting imaging system compared with traditional imaging systems: thicker samples can be imaged by the same X-ray source working at the same intensity.

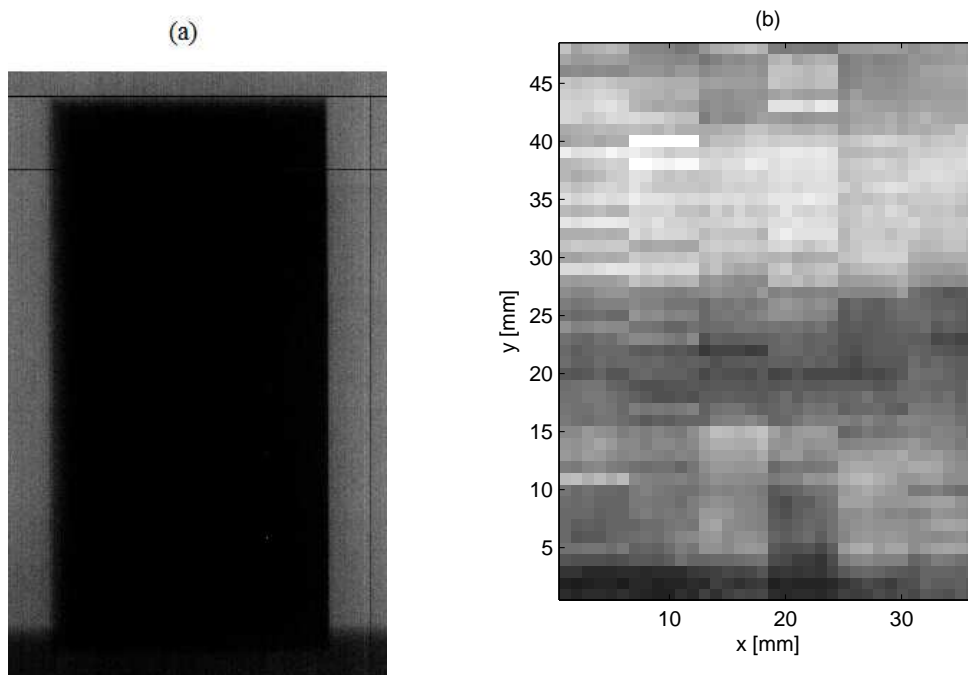


FIGURE 5.24: Six-scan images of the tungsten object and the iron object.(a) Image of the tungsten object.(b) Image of the iron object.

Chapter 6

Conclusion and discussion

6.1 Conclusion

We are now developing a photon-counting X-ray imaging system for nondestructive testing of steel pipes in nuclear facilities and concrete infrastructures. The system consists of stacked edge-on silicon strip detectors and has much higher efficiency for high-energy photons. The photon-counting technique can improve spatial resolution and fit the system for testing thicker samples.

The a-Si/c-Si heterojunction technique was successfully applied in fabricating silicon strip detector. Compared with conventional normal planar process for fabricating silicon diode detectors, this a-Si/c-Si heterojunction process with PECVD technique is greatly simplified and is suitable for mass production at low cost. The fabricated 50-channel strip detector showed uniform leakage current characteristics and the leakage current density was as low as 0.06 nA/mm^2 at full-depletion bias voltage. The detector had energy resolutions of 2.8 keV FWHM at 59.5 keV and 2.9 keV FWHM at 122 keV. The spatial resolution of the 1 mm-pitch strip detector was measured to be lower than 2 mm (FWHM) with face-on geometry.

ToT method was adopted to readout signals of the silicon strip detectors. Based on the 48-channel ToT ASIC, we built continuous-mode edge-on modules for gamma-ray or low intensity X-ray imaging and a pulse-mode edge-on module for LINAC X-ray imaging.

A pulse-mode module consisted of 6 stacked strip detectors were constructed. The module was evaluated with a ^{137}Cs gamma-ray source. The module had efficiency of about 20% for the 662 keV photons with a threshold of about 180 keV and without anticoincidence filter. Spatial resolution of the module was measured to be about 1 mm (rms). One-scan and six-scan images of a 2-cm-thick tungsten sample and an 1-cm-thick

iron sample were obtained. Each scan lasted for about 3600 s with the 1 MBq ^{137}Cs source for accumulating acceptable statistics. The module was also evaluated with the 0.95 MeV LINAC X-ray source. Spatial resolution of the module was measured to be about 1 mm (rms). Six-scan images of the same tungsten sample and iron sample were obtained. Each scan lasted for about 180 s. Compared with scan images measured with the ^{137}Cs source, the images measured with the LINAC X-ray source reproduced the samples better without distortion and amplification.

The six-layer module was also used to scan a 20-cm-thick concrete. Another 1.2-cm-thick lead was inserted to simulate a thicker concrete, reinforcing bars inside the concrete were observed. A flat panel detector working in energy-integrating mode was also used to imaging the concrete, however, the reinforcing bars were invisible when the setup was the same with the measurement proceeded with our silicon strip detectors, validating that the newly developed imaging system is capable of imaging thicker samples.

6.2 Discussion

Silicon detectors are generally considered to be only suitable for low-energy photons or charged particles. However, our results prove that silicon detectors are also suitable for high-energy imaging applications, especially very high detection efficiency can also be realized when silicon strip detectors are aligned in edge-on geometry.

The successful application of the simplified a-Si/c-Si heterojunction process in fabricating strip detectors has great potentials to be widely used. Excellent energy resolution makes the strip detector qualified for low-energy spectral photon counting imaging. Cathode patterns can be easily fabricated on a large-area silicon wafer with little cost and the 2D pixel detector is qualified for low energy X-ray/gamma-ray radiography or Compton imaging (as scatter).

The novel geometry of the stacked edge-on strip detectors have greatly advantages compared with traditional film/array detectors or slit-detector for scanning the image of samples. Edge-on geometry guarantees high detection efficiency for high-energy photons and the stack geometry is beneficial for achieving a full image with a single irradiation. The novel system is particularly suitable for high-energy X-ray imaging, and the process time can be shortened and dose to environment can be reduced which is very important for situ NDT evaluation of thick samples. The large length of the system enhances scattering inside the detectors and thus degrades the spatial resolution compared with array detector. This degradation is compensated with the photon counting technique that can filter noise and suppress scattering contribution. It should be noted that insertion of

heavy materials such as tungsten inside the detector module enhances scattering other than suppressing scattering when a high-energy X-ray source is used. A collimator module placed close to the sample is beneficial for suppressing scattering. In addition, the photon-counting technique makes the system qualified for imaging much thicker sample than imaging systems working in energy-integrating mode.

The measured edge-on spatial resolution of the continuous-module was about twice that of the pulse-mode module. The main reason was that the source-to-detector distance was twice the source-to-object distance and the real value was doubled during measurement. The doubling or distortion was also observed in the obtained images with the ^{137}Cs source compared with images measured with LINAC X-ray source.

Suffered from limited IO number of DAQ FPGA, we only constructed a module with 6 layers and the pitch of the module was 6 mm. As a result, few details can be obtained in the one-scan images and several scans were proceeded for a more detailed image of the sample. A full image can be realized by a module with more layers stacked with smaller pitch.

Suffered from nonuniformity of the detector and the ASIC, images were only obtained with data normalized by the flood-field data. This enforces an extra flood-field measurement compared with mature imaging systems such as the commercial Perkin Elmer flat panel detectors, so it would be better if we can calibrate the response of each channel of our system permanently. This can be realized by implementing dToT electronics of which the energy response is linear.

6.3 Future works

We are planning to use 4 (2×2) modules for X-ray imaging. Each module has more silicon strip detectors stacked with about 1-mm pitch as shown in Figure 6.1, and region of interest can be as large as 10 cm \times 10 cm by using 4 modules. In addition, tungsten collimator module as shown in Figure 6.2 will be applied in the following experiments.

We are planning to proceed on-site NDT of steel structures in NPPs and concrete in infrastructures with both the 0.95 MeV and 3.95 MeV LINAC X-ray sources. Dynamic ToT ASIC will be optimized and implemented in the imaging system.

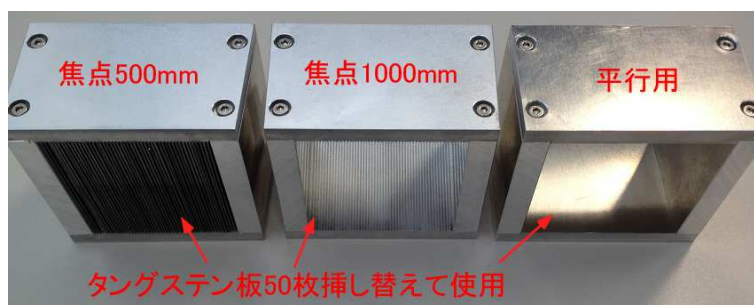
FIGURE 6.1: Imaging system composed of (2×2) modules.

FIGURE 6.2: Tungsten collimator modules.

Bibliography

- [1] URL http://www.enecho.meti.go.jp/en/category/others/basic_plan/pdf/4th_strategic_energy_plan.pdf.
- [2] URL <http://www.world-nuclear.org/info/Country-Profiles/Countries-G-N/Japan/>.
- [3] D. M. McCann and M. C. Forde. Review of NDT methods in the assessment of concrete and masonry structures. *NDT & E International*, 34(2):71–84, 2001.
- [4] L. H. Brasche. Feasibility Study for Detection and Quantification of Corrosion in Bridge Barrier Rails. Report, Iowa State University, 2013.
- [5] IAEA. Guidebook on non-destructive testing of concrete structures. 2002.
- [6] G. Jonkmans, V. N. P. Anghel, and et al. Jewett, C. Nuclear waste imaging and spent fuel verification by muon tomography. *Annals of Nuclear Energy*, 53:267–273, 2013.
- [7] L. W. Alvarez, J. A. Anderson, and et al. Bedwei, F. E. Search for hidden chambers in the pyramids. *Science*, 167:832–839, 1970.
- [8] K. N. Borozdin, G. E. Hogan, and et al. Morris, C. Surveillance: Radiographic imaging with cosmic-ray muons. *Nature*, 422(6929):277–277, 2003.
- [9] D. Venable, D. Dickman, and et al. Hardwick, J. PHERMEX: A PULSED HIGH-ENERGY RADIOGRAPHIC MACHINE EMITTING X-RAYS. Report, Los Alamos Scientific Lab., N. Mex., 1967.
- [10] L. Auditore, R. C. Barna, and et al. De Pasquale, D. Pulsed 5 MeV standing wave electron linac for radiation processing. *Physical Review Special Topics - Accelerators and Beams*, 7(3):030101, 2004.
- [11] L. Auditore, R. C. Barna, and et al. De Pasquale, D. Design of a 5 MeV electron linac based X-ray source source. *Nuclear Instruments and Methods in Physics Research Section B: Beam Interactions with Materials and Atoms*, 240(4):913–922, 2005.

- [12] H. Toyokawa, H. Kanada, and et al. Kaihori, T. Application of High-Energy Photon CT System With Laser-Compton Scattering to Non-Destructive Test. *IEEE Transactions on Nuclear Science*, 55(6):3571–3578, 2008.
- [13] R. H. Milburn. Electron Scattering by an Intense Polarized Photon Field. *Physical Review Letters*, 10(3):75–77, 1963.
- [14] M. Uesaka, M. Jin, and W. Wu. Commissioning of portable 950 keV/3.95 MeV X-band linac X-ray source for on-site transmission testing. *E-Journal of Advanced Maintenance*, 5(2):100, 2013.
- [15] M. Ueaska, K. Dobashi, and et al. Fujiwara, T. On-site nondestructive inspection by upgraded portable 950 keV/3.95 MeV X-band linac x-ray sources. *Journal of Physics B: Atomic, Molecular and Optical Physics*, 47(23):234008, 2014.
- [16] C. W. Van Eijk. Inorganic scintillators in medical imaging. *Physics in medicine and biology*, 47(8):R85–R106, 2002.
- [17] URL http://www.perkinelmer.com/corporate/images/009298B_02%20PRD_tcm137-169967.pdf.
- [18] L. Auditore, R. C. Barna, and et al. Emanuele, U. X-ray tomography system for industrial applications. *Nuclear Instruments and Methods in Physics Research Section B: Beam Interactions with Materials and Atoms*, 266(10):2138–2141, 2008.
- [19] Y. Eisen, A. Shor, and I. Mardor. CdTe and CdZnTe gamma ray detectors for medical and industrial imaging systems. *Nuclear Instruments and Methods in Physics Research Section A: Accelerators, Spectrometers, Detectors and Associated Equipment*, 428(1):158–170, 1999.
- [20] N. Estre, D. Eck, and et al. Pettier, J. L. High-energy X-ray imaging applied to non destructive characterization of large nuclear waste drums, pages 1–6, 2013.
- [21] H. Miyai, H. Kitaguchi, and et al. Kawasaki, S. Characteristics of a silicon detector for industrial X-ray computed tomography. *Nuclear Instruments and Methods in Physics Research Section A: Accelerators, Spectrometers, Detectors and Associated Equipment*, 353(1-3):97–100, 1994.
- [22] H. Miyai, S. Kawasaki, and et al. Kitaguchi, H. Response of silicon detector for high energy X-ray computed tomography. *IEEE Transactions on Nuclear Science*, 41(4):999–1003, 1994.
- [23] H. Miyai, K. Satou, and et al. Kitaguchi, H. A high energy X-ray computed tomography using silicon semiconductor detectors, volume 2, pages 816–820 vol.2, 1996.

- [24] K. Katsuyama, A. Ishimi, and et al. Maeda, K. Development of a High Resolution X-Ray CT Technique for Irradiated Fuel Pellets. *IEEE Transactions on Nuclear Science*, 59(4):1397–1400, 2012.
- [25] URL <http://www.nist.gov/pml/data/xraycoef/index.cfm>.
- [26] B. Mikulec. Development of segmented semiconductor arrays for quantum imaging. *Nuclear Instruments and Methods in Physics Research Section A: Accelerators, Spectrometers, Detectors and Associated Equipment*, 510(1-2):1–23, 2003.
- [27] N. Metropolis and S. Ulam. The monte carlo method. *Journal of the American statistical association*, 44(247):335–341, 1949.
- [28] G. Cowan. *Statistical data analysis*. Oxford University Press, 1998.
- [29] J. F. Briesmeister. MCNP—A general Monte Carlo code for neutron and photon transport. *LA-7396-M*, 1986.
- [30] H. Hirayama, Y. Namito, and et al. Nelson, W. R. The EGS5 code system. Report, United States. Department of Energy, 2005.
- [31] A. Ferrari, P. R. Sala, and et al. Fasso, A. FLUKA: A multi-particle transport code (Program version 2005). Report, 2005.
- [32] S. Agostinelli, J. Allison, and et al. Amako, K. Geant4-a simulation toolkit. *Nuclear Instruments and Methods in Physics Research Section A: Accelerators, Spectrometers, Detectors and Associated Equipment*, 506(3):250–303, 2003.
- [33] V. N. Ivanchenko. Geant4 toolkit for simulation of HEP experiments. *Nuclear Instruments and Methods in Physics Research Section A: Accelerators, Spectrometers, Detectors and Associated Equipment*, 502(2-3):666–668, 2003.
- [34] X.-M. C. Team. MCNP—A General Purpose Monte Carlo N-Particle Transport Code, Version 5. Report, LA-UR-03-1987, Los Alamos National Laboratory, April 2003., 2003.
- [35] S. Jan, G. Santin, and et al. Strul, D. GATE: a simulation toolkit for PET and SPECT. *Physics in Medicine and Biology*, 49(19):4543, 2004.
- [36] J. Baro, J. Sempau, and et al. Fernandez-Varea, J. M. PENELOPE: An algorithm for Monte Carlo simulation of the penetration and energy loss of electrons and positrons in matter. *Nuclear Instruments and Methods in Physics Research Section B: Beam Interactions with Materials and Atoms*, 100(1):31–46, 1995.
- [37] M. B. Emmett. MORSE Monte Carlo radiation transport code system. Report, Oak Ridge National Lab., TN (USA), 1983.

- [38] J. F. Ziegler, M. D. Ziegler, and J. P. Biersack. SRIM –The stopping and range of ions in matter (2010). *Nuclear Instruments and Methods in Physics Research Section B: Beam Interactions with Materials and Atoms*, 268(11-12):1818–1823, 2010.
- [39] K. Niita, T. Sato, and et al. Iwase, H. PHITS—a particle and heavy ion transport code system. *Radiation Measurements*, 41(9-10):1080–1090, 2006.
- [40] M. Brigida, C. Favuzzi, and et al. Fusco, P. A new Monte Carlo code for full simulation of silicon strip detectors. *Nuclear Instruments and Methods in Physics Research Section A: Accelerators, Spectrometers, Detectors and Associated Equipment*, 533(3):322–343, 2004.
- [41] G. Lutz. *Semiconductor radiation detectors*, volume 10. Springer, Munich, Germany, 1999.
- [42] J. P. Ponpon. Semiconductor detectors for 2D X-ray imaging. *Nuclear Instruments and Methods in Physics Research Section A: Accelerators, Spectrometers, Detectors and Associated Equipment*, 551(1):15–26, 2005.
- [43] S. Del Sordo, L. Abbene, and et al. Caroli, E. Progress in the Development of CdTe and CdZnTe Semiconductor Radiation Detectors for Astrophysical and Medical Applications. *Sensors*, 9(5):3491–3526, 2009.
- [44] M. Yabe and N. Sato. Silicon nuclear radiation detectors of a-Si:H/c-Si heterojunction structure with sensitive large area or array area. *Sensors and Actuators A: Physical*, 22(1-3):487–493, 1990.
- [45] Y. Chiba, I. Endo, and et al. Kubota, M. A position-sensitive radiation detector using a heterojunction of amorphous and crystalline silicon. *Nuclear Instruments and Methods in Physics Research Section A: Accelerators, Spectrometers, Detectors and Associated Equipment*, 299(1-3):152–156, 1990.
- [46] G. F. Knoll. *Radiation detection and measurement*. John Wiley & Sons, 2010.
- [47] H. Spieler. *Semiconductor Detector Systems*. Oxford University Press, 2005.
- [48] S. Chatrchyan, G. Hmayakyan, and et al. Khachatryan, V. The CMS experiment at the CERN LHC. *Journal of Instrumentation*, 3, 2008.
- [49] J. Bregeon and F.-L. Collaboration. Design and performance of the silicon strip tracker of the Fermi Large Area Telescope. *Journal of Instrumentation*, 6, 2011.
- [50] R. C. Jaeger. *Introduction to Microelectronic Fabrication*, volume 5 of *Modular Series on Solid State Devices*. Prentic-Hall, Inc, Upper Saddle River, New Jersey, 2 edition, 2002.

- [51] B. Hans and D. Mats. Photon-counting spectral computed tomography using silicon strip detectors: a feasibility study. *Physics in Medicine and Biology*, 55(7):1999, 2010.
- [52] P. Mats, H. Ben, and et al. Staffan, K. Energy-resolved CT imaging with a photon-counting silicon-strip detector. *Physics in Medicine and Biology*, 59(22):6709, 2014.
- [53] R. Becker, A. Grillo, and et al. Jacobsen, R. Signal processing in the front-end electronics of BaBar vertex detector. *Nuclear Instruments and Methods in Physics Research Section A: Accelerators, Spectrometers, Detectors and Associated Equipment*, 377(2-3):459–464, 1996.
- [54] I. Kipnis, T. Collins, and et al. DeWitt, J. A time-over-threshold machine: the read-out integrated circuit for the BABAR Silicon Vertex Tracker. *IEEE Transactions on Nuclear Science*, 44(3):289–297, 1997.
- [55] J. Bardeen and W. H. Brattain. The transistor, a semi-conductor triode. *Physical Review*, 74(2):230, 1948.
- [56] W. Shockley. The Theory of P-N Junctions in Semiconductors and P-N Junction Transistors. *Bell System Technical Journal*, 28(3):435–489, 1949.
- [57] J. S. Kilby. Invention of the integrated circuit. *Electron Devices, IEEE Transactions on*, 23(7):648–654, 1976.
- [58] G. E. Moore. Cramming more components onto integrated circuits (Reprinted from *Electronics*, pg 114-117, April 19, 1965). *Proceedings of the Ieee*, 86(1):82–85, 1998.
- [59] R. R. Schaller. Moore’s law: past, present and future. *Spectrum, IEEE*, 34(6): 52–59, 1997.
- [60] URL http://en.wikipedia.org/wiki/Integrated_circuit.
- [61] R. J. Baker. *CMOS: circuit design, layout, and simulation*, volume 18 of *IEEE Series on Microelectronic Systems*. John Wiley & Sons, Hoboken, New Jersey, 3 edition, 2011.
- [62] K. Asada and K. Hoh. VLSI Design and Education Center (VDEC) current status and future plan, pages 365–369, 1997.
- [63] K. Shimazoe, T. Orita, and et al. Nakamura, Y. Time over threshold based multi-channel LuAG-APD PET detector. *Nuclear Instruments and Methods in Physics Research Section A: Accelerators, Spectrometers, Detectors and Associated Equipment*, 731(0):109–113, 2013.

- [64] M. J. Paulus, J. M. Rochelle, and et al. Andreaco, M. S. A low-noise, wide-band CMOS charge-sensitive preamplifier for use with APD/LSO PET detectors. *IEEE Transactions on Nuclear Science*, 43(3):1666–1671, 1996.
- [65] D. M. Binkley, B. S. Puckett, and et al. Casey, M. E. A power-efficient, low-noise, wideband, integrated CMOS preamplifier for LSO/APD PET systems. *IEEE Transactions on Nuclear Science*, 47(3):810–817, 2000.
- [66] J. Y. Yeom, I. Defendi, and et al. Takahashi, H. A 12-channel CMOS preamplifier-shaper-discriminator ASIC for APD and gas counters. *IEEE Transactions on Nuclear Science*, 53(4):2204–2208, 2006.
- [67] URL <http://www.ti.com/lit/ds/symlink/dac128s085.pdf>.
- [68] T. Orita, H. Takahashi, and et al. Shimazoe, K. A new pulse width signal processing with delay-line and non-linear circuit (for ToT). *Nuclear Instruments and Methods in Physics Research Section A: Accelerators, Spectrometers, Detectors and Associated Equipment*, 648, Supplement 1(0):S24–S27, 2011.
- [69] K. Shimazoe, H. Takahashi, and et al. Boxuan, S. Dynamic Time Over Threshold Method. *IEEE Transactions on Nuclear Science*, 59(6):3213–3217, 2012.
- [70] T. Orita, K. Shimazoe, and H. Takahashi. The dynamic time-over-threshold method for multi-channel APD based gamma-ray detectors. *Nuclear Instruments and Methods in Physics Research Section A: Accelerators, Spectrometers, Detectors and Associated Equipment*, 775:154–161, 2015.
- [71] T. Orita. *Study on a time-width signal processing method of radiation signals*. Thesis, 2013.
- [72] URL <http://www.prime-sys.co.jp/products/cxcard4.htm>.
- [73] URL <http://www.perkinelmer.com/PDFs/Downloads/XRD%201622%20Product%20Note.pdf>.